

A STUDY OF TWO OPPOSING PLANAR AIR JETS

A STUDY OF TWO OPPOSING PLANAR AIR JETS

By

Moustafa Hassaballa, B.Sc.

A Thesis

Submitted to the School of Graduate Studies

in Partial Fulfillment of the Requirements

for the Degree

Master of Applied Sciences

McMaster University

© Copyright by Moustafa Hassaballa, August 2013

Abstract

This thesis tackles the behavior of two planar shaped opposing air jets. The word opposing means that the two air jets are positioned against each other to have a common centerline so that they impinge on each other. Opposing planar jets have several applications in industry which include: galvanization, chemical mixing processes, and combustion. Opposing planar jets are found to produce high level low frequency acoustic tones. In this study, the acoustic response of the opposing planar jets is investigated for different operating conditions. Acoustic tone analysis is performed for a wide range of jet exit velocities and separation distances between the two jets. Results show that the jets produce strong acoustic tones over the whole investigated range of test conditions. The acoustic response depends on the operating conditions of the jets and the acoustic tone is found to be generated by a self-sustained flow oscillation of the two jets.

In order to further understand the reported oscillation phenomenon, particle image velocity (PIV) is utilized. Images of the oscillating flow field are acquired and image analysis is performed to obtain various flow dynamic properties. A computational fluid dynamics simulation is performed to help in highlighting the oscillation behavior of the jets. Results reveal that the jets exhibit anti-symmetric “flapping” oscillation behavior. The jets are found to initially deflect away from their common centerline due to high stagnation pressure in the impingement region, while they deflect back to their common centerline due to cross stream oscillating velocity in the entrainment regions around the jets.

Acknowledgements

I would like to extend my deepest appreciation for Prof. Dr. Samir Ziada for his continuous help, solid support and valuable advice and mentorship throughout this study. I will always be grateful for his help and what I have learned from him.

I wish to extend my gratitude to my colleagues in the flow induced vibration group at McMaster University and especially to Dr. David Arthurs for his support and help in experimental setup and technical aspects of the experiments done in this study.

Finally, I would like also to thank my family and friends, who has been supportive to me along my educational journey.

Nomenclature

AR Nozzle Aspect Ratio

b Jet Breadth [m]

β Open area ratio of nozzle conditioning screens

δ Boundary Layer thickness [mm]

δ^* Displacement Thickness [mm]

θ Momentum Thickness [mm]

γ Ratio of specific heats of air

CFD Computational Fluid Dynamics

dBA Decibel (A-weighted)

$\frac{\partial U}{\partial Y}$ Stream wise flow shear in Y direction at a measurement point [1/s]

$\frac{\partial V}{\partial Z}$ Cross stream flow shear in Z direction at a measurement point [1/s]

η Isentropic efficiency of the nozzle

f Frequency of dominant oscillations in the flow [Hz]

f_0 Fundamental frequency of system acoustic response [Hz]

f_1	First higher harmonic frequency [Hz]
f_2	Second higher harmonic frequency [Hz]
f_3	Third higher harmonic frequency [Hz]
f'_1	Frequency higher than peak tone frequency f_0 at which acoustic power is halved [Hz]
f'_2	Frequency lower than peak tone frequency f_0 at which acoustic power is halved [Hz]
h	Nozzle thickness (jet thickness) [mm]
H	Shape Factor for shear layer
l	Impingement length for impinging shear flows [m]
L	Nozzle Span length [mm]
LDA	Laser Doppler anemometry
Ma	Mach Number
n	Number of acquired phase angles per cycle
P	Static pressure in the nozzle [Pa]
P_∞	Ambient pressure [Pa]
P_{mag}	Magnitude of absolute pressure at a measurement point [Pa]

PIV	Particle Image velocimetry
Q	Tone quality factor
Re	Reynolds Number
SPL	Sound pressure level [dB] ($P_{\text{ref}} = 20 \mu\text{Pa}$)
St	Strouhal number (based on nozzle diameter St_d , or impingement distance St_z)
τ	Oscillation period [Sec]
Φ	Phase angle of the flow oscillation cycle
U_0	Flow velocity at nozzle exit [m/s]
$U(\Phi)$	Magnitude of flow velocity in Stream wise direction Z at a measurement point at phase angle Φ [m/s]
V_0	Initial flow velocity of the fluid [m/s]
V_{avg}	Average of the instantaneous cross stream velocity component over a complete Oscillation cycle at a measurement point [m/s]
V_{mag}	Velocity magnitude at a measurement point
$V_{\text{mag,avg}}$	Average velocity magnitude over the whole oscillation cycle at a measurement point [m/s]
$V(\Phi)$	Magnitude of flow velocity in the cross stream direction Y at a measurement point at phase angle Φ [m/s]
V_{ϕ}'	Oscillating cross stream velocity components at a measurement point [m/s]

X	Span wise direction [mm]
Y	Cross stream direction [mm]
Z	Stream wise direction [mm]
z	Distance separating the two nozzles exits
z/h	Impingement ratio
ω_{mag}	Vorticity magnitude at a measurement point [1/s]
$\omega_{\text{mag}_{\text{avg}}}$	Average vorticity magnitude over the whole oscillation cycle at a measurement point [1/s]

Table of Contents

Abstract.....	iii
Acknowledgements.....	iv
Nomenclature.....	v
Table of Contents.....	ix
List of Figures	xi
List of Tables.....	xvii
Chapter 1 Introduction.....	1
1.1 Motivation.....	1
1.2 Thesis Layout.....	3
Chapter 2 Background & Literature Review.....	5
2.1 Background.....	5
2.2 Previous Work on Opposing Jets.....	12
2.2.1 Opposing Jets.....	12
2.2.2 Square and Planar Shaped Opposing Jets.....	13
2.2.3 Opposing Jets Oscillation.....	14
2.3 Objectives.....	21
Chapter 3 Experimental Setup.....	22
3.1 Nozzles Geometry.....	22
3.2 Nozzles Setup.....	24
3.3 Acoustic Tone Measurements.....	25
3.4 Flow Field Measurements.....	27
3.4.1 Exit Flow Velocity.....	27

3.4.2 Particle Image Velocimetry.....	30
Chapter 4 Results and Analysis	36
4.1 Acoustic Response.....	37
4.1.1 Acoustic Tone Data Analysis.....	37
4.1.2 Effect of Impingement Ratio.....	39
4.1.3 Effect of Nozzle Exit Velocity.....	46
4.2 Fluid Dynamic Behavior.....	51
4.2.1 Flow Fields Data Analysis.....	51
4.2.2 Flow Fields.....	53
4.2.3 Oscillation Mechanism.....	61
4.2.4 Computational Fluid Dynamics Flow Simulation.....	71
Chapter 5 Discussion and Conclusions.....	78
5.1 Flow Oscillation Mechanism.....	78
5.2 Oscillation Frequency.....	80
5.3 Acoustic Tone Generation.....	83
5.4 Conclusions.....	84
5.5 Suggestion for Future Work.....	86
Bibliography.....	87
Appendix I: CFD Simulation Details.....	95
Appendix II: Uncertainty and Error Analysis	102
Appendix III: Effect of measurement equipment on Acoustic Response	113
Appendix IV: Experimental Equipment Data	119

List of Figures

Figure 2-1 Figure 2-1 Schematic of a Free Jet (Adopted from Arthurs and Ziada, 2012)

Figure 2-2 Schematic of suggested oscillation mechanism by Denshchikov et al., 1978)

Figure 3-1 Planar Air Nozzle (Drawings are adopted from Arthurs & Ziada, 2012)

Figure 3-2 Schematic for the Air Supply System

Figure 3-3 Nozzles Setup, Virtual Image

Figure 3-4 Opposing Planar Jet System Parameters

Figure 3-5 Normalized Jet Velocity profile for nozzles at exit nozzle velocities of $U_0 =$
150, 200, 250 m/s.

Figure 3-6 PIV Experimental Setup

Figure 3-7 Phase-Locking Illustrated

Figure 4-1 Spectrum of the Microphone Signal at $U_0 = 260$ m/s & $z/h = 40$

Figure 4-2 Acoustic Tone Response Spectra at three different impingement ratio a) $z/h =$
40 b) $z/h = 60$ c) $z/h = 80$, respectively at nozzle exit velocity $U_0 = 250$ m/s

Figure 4-3 Waterfall plot showing acoustic response of planar opposing jets at Exit flow velocity $U_0 = 150$ m/s and impingement ratio $7 \leq z/h \leq 130$.

Figure 4-4 Waterfall Plot showing acoustic response of planar opposing jets at Exit flow velocity $U_0 = 200$ m/s and impingement ratio $7 \leq z/h \leq 130$.

Figure 4-5 Waterfall Plot showing acoustic response of planar opposing jets at Exit flow velocity $U_0 = 250$ m/s and impingement ratio $7 \leq z/h \leq 130$.

Figure 4-6 Plots for Acoustic Tone Fundamental Frequency f_0 as a function of the impingement ratio z/h for three jet exit velocities $U_0 = 150, 200$ & 250 m/s.

Figure 4-7 Plots for Strouhal number $St_z = f_0 z / U_0$ as a function of impingement Ratio z/h

Figure 4-8 Waterfall plots showing acoustic tone response of planar opposed jets for a fixed impingement a) $z/h = 40$ & b) $z/h = 50$ for a variable nozzle exit velocity $150 \leq U_0 \leq 260$ m/s

Figure 4-9 Plots for Acoustic Tone Fundamental Frequency f_0 as a function of jet exit velocities U_0 for constant impingement ratio of $z/h = 40$ & 50 .

Figure 4-10 Plots for Strouhal number $St_z = f_0 z / U_0$ as a function of jet exit velocities U_0 for constant impingement ratio of $z/h = 40$ and 50 .

Figure 4-11 Tone Quality Factor Q for various impingement ratio for $U_0 = 200$ m/s

Figure 4-12 Velocity Magnitudes (V_{mag}) at each phase angle (Φ) of the oscillation cycle

Figure 4-13 Vorticity Magnitudes (ω) at each phase angle (Φ) of the oscillation cycle

Figure 4-14 Average Velocity and Vorticity Magnitude over a Complete Oscillation Cycle

Figure 4-15 Crossstream Velocity Component (V_{ϕ}) at each phase angle (Φ) of the oscillation cycle

Figure 4-16 Crossstream Oscillating Velocity Component (V'_{ϕ}) at each phase angle (Φ) of the oscillation cycle

Figure 4-17 Velocity Magnitudes (V_{mag}) and Crossstream Oscillating Velocity Component (V'_{ϕ}) at each selected phase angles ($\Phi=45^{\circ}, 135^{\circ}, 225^{\circ}$ and 315°) of the oscillation cycle

Figure 4-18 Stream lines at each phase angle (Φ) of the oscillation cycle

Figure 4-19 CFD Velocity Magnitude fields at each phase angle (Φ) of the oscillation cycle

Figure 4-20 CFD Crossstream Oscillating Velocity Component (V'_{ϕ}) at each phase angle (Φ) of the oscillation cycle (+ve refers to velocity to the right hand side (+ve Y axis direction))

Figure 4-21 CFD Pressure fields [Pa] at each phase angle (Φ) of the oscillation cycle

Figure 5-1 Schematic of suggested flow oscillation mechanism

Figure 5-2 Schematic of suggested acoustic tone generation mechanism

Figure I-1 Schematic of the Simulation Domain Geometry

Figure I-2 Meshed domain (green) with Boundary conditions for CFD simulation

Figure I-3 Results of Grid Dependence Study

Figure I-4 Results of Time Step Dependence Study

Figure II-1 Plot for Strouhal number (St_z) plot for $U_0=150$ m/s and variable impingement ratio (z/h) with uncertainty error bars

Figure II-2 Velocity Magnitude plot and velocity profiles for case of $z/h = 50$ and $U_0 = 200$ m/s oscillating at $f_0 = 226$ Hz at $\Phi = 90^\circ$

Figure III-1 Schematic Microphone location effect setup

Figure III-2 Waterfall plot for variable Mic Locations at $U_0 = 200$ m/s and $z/h = 30$

Figure III-3 Color plot for variable Mic Locations at $U_0 = 200$ m/s and $z/h = 30$

Figure III-4 Plot for fundamental tone frequency (f_0) with the microphone location [inch]

Figure III-5 Acoustic Tone Spectra for different number of averaged samples for $U_0 = 200$ m/s, $z/h = 40$, and $h = 2$ mm

Figure IV-1 481 Series High-Performance Rotation Stages

Figure IV-2 Velmex™ 2.5 inch wide A25 series screw drive UniSlide vice A2506P40-S2.5

Figure IV-3 VXM Stepping Motor Controller

Figure IV-4 40BP 1/4" high-level microphone

Figure IV-5 Typical frequency response for Type 40BP (without protection grid)

Figure IV-6 Free-field corrections for various angles of incidence (without protection grid)

Figure IV-7 1/4" Preamplifier Type 26AC

Figure IV-8 Specifications for G.R.A.S. 1/4" Preamplifier Type 26AC

Figure IV-9 Typical low-frequency response of Type 26AC for 1/2" (20 pF), 1/4" (6.5 pF) and 1/8" (3 pF) microphones

Figure IV-10 Typical max. rms output signal with 120 V and 30 V supply

Figure IV-11 GRAS™ model 12AA 2-channel power supply module

Figure IV-12 Sound Calibrator Type 42AB

Figure IV-13 Specifications for Sound Calibrator Type 42AB

Figure IV-14 National Instruments NI-9234 data acquisition

Figure IV-15 Validyne DP-15 pressure transducer

Figure IV-16 532nm New Wave Solo 120XT pulsed Nd:YAG laser specifications

Figure IV-17 PowerView Plus 4MP camera Specifications

Figure IV-18 Laser Pulse synchronizer Specifications

List of Tables

Table 2-1 Studies on Opposing Jets for Rejection Injection Molding Applications

Table 2-2 Ontario Regulations Regarding Workplace exposure to noise

Table 2-3 Summary of previous studies related to opposing jets instability

Table I-1 Mesh Properties for CFD Simulation

Table II-1 Uncertainty Analysis for Experiments Acoustic Response Parameters

Table II-2 Results of PIV uncertainty analysis for $z/h = 50$ and $U_0 = 200$ m/s

Table IV-1 Rotary Stage Specification

Table IV-2 Electronic Vice Specifications

Table IV-3 GRAS™ model 40BP ¼” Microphone Specification

Table IV-4 NI-9234 data acquisition specifications

Chapter 1: Introduction

1.1 Motivation

Fluid flow instability has been a topic of investigation since the beginning of the 20th century as the field of aero-acoustics was founded and developed along the past decades. Inherently unstable flows might be associated with organized fluid flow oscillations. Those oscillations are self-sustained by certain excitation mechanisms that give the flow its organized oscillatory behavior. Several excitation mechanisms have been discovered and outlined in the literature, while others remain unexplored. Examples of well-known self-sustained flow oscillations setups are: impinging jet flows such jet-edge, mixing layer-edge, jet-plate, and jet-slot flow oscillations (Rockwell & Naudascher, 1979). These kinds of flow oscillations apply to valves and pipeline applications. Another example is fluid flow around tandem or side by side cylinders which simulates flow instability in heat exchanger applications.

Self-sustained flow oscillations can sometimes be used to improve certain processes. In such cases, it can improve the heat transfer (Viskanta, 1993) and can improve mixing of fluids as well (Shi et al., 2011). In other cases, flow oscillations can be source of undesired vibration that affects the performance of an industrial process; moreover they can be source of high noise level (Arthurs et al., 2008), which causes ergonomic and health problems to labor working in industry, and in extreme cases may

result in shutting down of plants due to failure to adhere to noise bylaws or failure of equipment.

One category of flows that exhibits instability and self-sustained oscillations is impinging free shear flows. Most of the research efforts dedicated to instability of impinging shear flows were focused on setups where unstable free shear layer (example: jet) impinges on a solid surface located downstream of the shear layer. This impingement on the downstream solid surface produces a distortion in the downstream flow field, such distortion propagates back to the free shear layer separation edge (example: jet-edge) and closes that feedback loop enhancing the flow initial instability. Such cases were extensively researched in literature (Rockwell & Naudascher, 1979). On the other hand, little attention was given to a simple other case where a free shear layer impinges on another instead of a solid surface. This is perhaps due to the complexity of the flow, because many of the past investigated setups comprise 3-dimensionality effects and nonlinear flow effects. One way of investigating free shear layer instability is to use a simplified approach that approximates certain flows by a 2 dimensional flow. An example of such simplification is planar jets.

The problem of a jet impinging on another jet relates to many applications such as combustion, mixing in chemical reactors, galvanization processes and micro mixing. Many of the studies which comprise this setup focused on investigating the performance of the process as an input/output approach without examining the underlying physical phenomenon. A planar jet impinging on another planar jet (opposing planar jets) then

seems to be a convenient set-up to begin with to investigate a shear layer impinging on another shear layer because of two main reasons. First, such setup is present in many industrial applications thus studying its behavior could improve the performance of such applications. The second reason is because planar opposing jets are known to produce intense high acoustic tone accompanied by flow oscillation which in some cases is required to be controlled. Based on the previous information, studying such setup will help control the resulting oscillation and the associated noise.

1.2 Thesis Layout

This thesis consists of 5 chapters; in the current chapter motivation for the current study of opposing planar air jets is introduced; then the flow of the thesis contents is presented.

In chapter 2, the author presents the background of opposing jets applications, then we introduce studies that tackled applications related to opposing jets in industry and their findings. Following this, past studies related to instability and oscillation of opposing jets are outlined in general, then the author dedicates special attention to studies that are related to square and planar shaped opposing jets. Finally, the objectives from the current study on opposed planar jets are summarized.

In chapter 3, the experimental setup of the study is described in detail. First, the construction of the used planar air nozzles is introduced, and then a detailed description is

provided on how the planar nozzles were set up, positioned and controlled. Afterward, the procedure used to measure acoustic tone response of the system is presented. Then an outline on the used 2 dimensional Particle Image Velocimetry (PIV) system to measure the flow field is provided. This is then followed by a brief description of the method of measurement that is used for mapping the flow oscillation.

Chapter 4 presents the data analysis procedure and the results of the study. First, the system's acoustic tone response is reported showing the tone frequencies and sound pressure levels for different operating conditions, then a brief discussion of the findings is provided in the context of the current state of knowledge. Afterward, for a chosen operating condition, an explanation on how PIV results were obtained and analysed is provided, then the experimental results of the PIV investigation of the flow fields are introduced. Finally, results are presented for a simple computational fluid mechanics simulation that aids the understanding of the oscillation phenomenon.

In chapter 5, results of this study are discussed with focus on the associated underlying physical phenomenon and conclusions are drawn from the current study; including explanation of flow oscillation mechanism and system behaviour. Finally, some suggestions for future work are given.

Chapter 2: Background and Literature Review

In this chapter, we present an introduction to the topic of opposing jets, its applications and reasons for studying this setup. A comprehensive literature review on opposing jets is laid out for better understanding of various aspects of previous investigations of opposing jets. This is then followed by focusing on the few available studies that were dedicated to square and planar geometry opposing jet. Finally, the objectives of the current study are identified and presented based on current state of knowledge.

2.1 Background

Flow instability is considered as one of the key points in our study; this is because free planar jets are inherently unstable flows. This means that these flows cannot go back to their initial state when an initial disturbance is introduced. In case of free planar jets, velocity fluctuations of certain frequencies dominate the initial region of the jet's flow field; those frequencies are related to the jet flow parameters. This is important in the case of flow oscillation involving jets because the frequency of dominant velocity fluctuations in the flow is likely to scale with the jet oscillation frequency.

Generally, for any type of jets issuing from a nozzle in a still fluid there is a region where the jet merges with the surrounding fluid located at edges of that jet. A thin layer is formed at the jet edge (outlined in Figure 2-1) which combines the two streams (jet and

surrounding) that have different velocities; this layer is referred to as a free shear layer. Such layers exist in a planar jet flow and are known to be unstable by nature, where small velocity perturbations that occur at the jet edge can grow and magnify downstream if the perturbation frequency is within the unstable range.

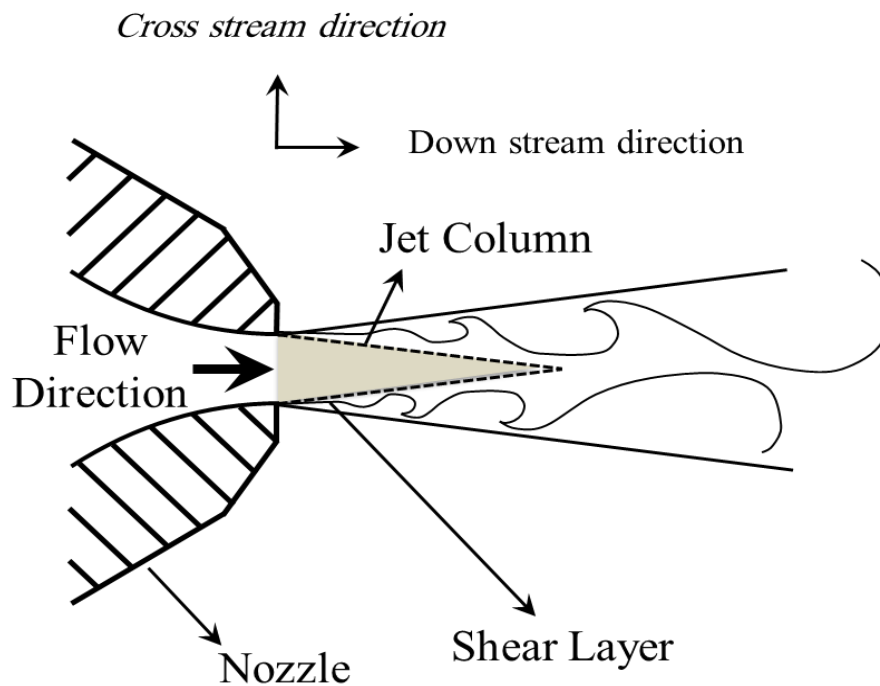


Figure 2-1 Schematic of a Free Jet
(Adopted from Arthurs and Ziada, 2012)

The instability of free shear layers was investigated by many authors over the past decades. For instance, Freymuth (1966) used external acoustic excitation to examine the free shear layer instability of laminar circular and planar jets. It was found in Freymuth's experimental study that the shear layer initial disturbances tend to grow exponentially

downstream. Vortical flow structures were observed downstream of the initial growth region at the jet edge as well. The initial disturbances were found to grow at a rate which scales with the excitation frequency and eventually those disturbances evolve into vortical structures. On the theoretical side, the earliest work on instability of shear layers was done by Lord Rayleigh (1880), where he developed the *linear stability theory* of inviscid free shear flows which ideally predicts the frequencies at which shear layers are unstable as well as the rate at which the initial flow disturbances grow. Later on, Michalke (1964, 1965) used the linear stability theory to calculate the instability frequencies for a hyperbolic shaped initial velocity profile of a free shear layer where this study characterized the frequencies which will receive maximum growth rate in the flow and others which decay in the free shear layer.

Other authors studied the instability for jets as a whole rather than only the shear layer part of the jet. This is done by introducing the velocity fluctuation (disturbances) into jet column (shown in Figure 2-1) rather than into the initial region of the shear layer only. For example, Sato (1960) utilized a two dimensional jet to investigate the resulting velocity fluctuations with and without acoustic excitation. It was found that initial velocity fluctuations grow downstream the jet at certain frequencies depending on the jet thickness and initial velocity profile. Furthermore, by numerically solving the perturbed Navier-Stokes equations for a laminar velocity profile, Sato (1960) predicted frequencies at which velocity fluctuations would receive high amplification downstream. Sato's experimental results were in agreement of his numerical solutions and indicated that the jet oscillations depend on the jet column instability. Later on, Bajaj & Garg (1977)

extended Sato's numerical analysis for different velocity profiles and Reynolds number and provided predictions for the dominant velocity fluctuation frequencies. On the other hand, it was found for all cases that the jet column instability frequency is lower than shear layer instability frequencies.

Studying free planar jet instabilities might give an insight into the behavior of two planar opposing jets instabilities and oscillation. Based on Sato (1960) and Bajaj & Garg (1977) studies, the dominant disturbance frequencies for flow conditions of the jets in current study should be in the range of 6 kHz to 10 kHz. However, the oscillations observed in the current study are much lower than this frequency range. This underlines the necessity to explore the underlying oscillation phenomenon in the current study.

A key parameter which is often used to characterize flow instabilities is the Strouhal number. The Strouhal number is a dimensionless frequency and typically defined as the ratio between the vortex shedding frequency to the velocity of the fluid divided by the characteristic length for the flow. This can be written in the following mathematical form:

$$St_{\text{characteristic length}} = \frac{\text{Frequency} \times \text{Characteristic Length}}{\text{Flow Velocity}}. \quad (2-1)$$

The value of Strouhal number for flow instability may vary according to the type of flow setup, the flow velocity, and dimensional parameters. For jet flows, the Strouhal number can be based on various characteristic lengths depending on the predominant

instability mechanism in the flow. For example, for shear layer instability of free jets, the Strouhal number is usually based on the momentum thickness (θ) at the nozzle exit, which can be represented by the following equation:

$$St_{\theta} = \frac{f \theta}{V_0}. \quad (2-2)$$

where f is the frequency of dominant oscillations in the flow, while V_0 is the initial fluid velocity. In this case, the frequency scales with the momentum thickness giving a specific Strouhal number for the flow depending on the flow velocity magnitude and shape of shear layer.

For jet column instability of free jets the Strouhal number is usually based on the jet breadth (b) (which is defined as the cross stream distance from the jet centerline to the point where the jet velocity is half the centerline velocity), and can be represented by the following equation:

$$St_b = \frac{f b}{V_0}. \quad (2-3)$$

In this case, the frequency scales with the jet breadth and gives a specific Strouhal number for the flow which depends on the magnitude of the flow velocity and the shape of the jet velocity profile.

On the other hand, for a case when a jet impinges on a solid boundary which is one type of flows that is commonly referred to as impinging shear layers, the Strouhal number can be based on the impinging length (which is the distance between the separation edge of the shear layer and the solid boundary), and is defined as:

$$St_l = \frac{f l}{V_0}. \quad (2-4)$$

where f is the frequency of the flow oscillations and l is the impingement length.

The latter case of impinging free shear layer flows received considerable attention as the frequency of flow oscillations was found to be related to a feed-back mechanism which was outlined and studied by Powel (1961, 1988) and afterwards by several other authors. In this case the initial small disturbances at the edge of shear layers grow downstream until they are faced by the solid boundary on which impingement happens; the impingement produces feedback waves which travel upstream and enhance the initial disturbances only and when they are in phase with the initial disturbances. These feedback mechanisms are categorized into 3 types according to Rockwell & Naudascher (1979): The first is *the fluid-elastic mechanism*, where the disturbance feedback is generated by the vibrations of a solid boundary; this can happen when a flow passes over flexible downstream body (Ziada, 2002). Extreme cases happen when the vortex shedding frequency matches with the natural frequency of the solid body where this causes high flow and structural oscillation amplitudes. The second feedback mechanism is the *fluid-*

resonant mechanism; this mechanism occurs when the vortex shedding frequency reaches a value near to that of the acoustic resonance frequency of the setup. As this happens acoustic feedback waves are generated by the resonant sound field which sustains the flow oscillation (Ziada, 2001). The third mechanism is *the fluid-dynamic mechanism*, in this case feedback of disturbances results from flow impingement on a downstream solid boundary (Ziada, 1995). All pervious mentioned oscillations can be critical to many applications in the industry where flow oscillations might not cause favorable effects.

One of the latest studies tackling impinging shear layers was done by Arthurs (2010, 2012). The authors of this study utilized a high speed subsonic planar jet impinging on a plate, and classified the jet acoustic tone frequencies into two types. The first type results from a fluid-dynamic feedback mechanism and the second type results from a fluid-resonant feedback mechanisms. In this study a modified feedback model was developed based on Powel's earlier work on similar setups to predict the genertaed acoustic tone frequncy. The importance of the latter study becomes more apparent from the fact that in the current studywmploys the same air nozzle that was used by Arthurs (2012), however, in the current invistigation the plate was replaced by another (but identical) planar nozzle adjusted to a thickness of 2 mm. The tone frequencies and strouhal numbers obseved in Arthur's study were typically in a range of one order of magnitude higher than the frequencies observed in current study, which suggests that the oscillation mechanisms involved in the current study are different from those described by Arthurs and Ziada (2010, 2012)

2.2 Previous Work on Opposing Jets

Opposing planar jets are important for several industries, such as production of galvanized sheet steel, air/fuel mixing in combustion applications, and for reactors used in the chemical industry. In these applications, the opposing planar jet system can be problematic due to self-excited oscillations. These oscillations can produce excessive pressure pulsations which can act as source of vibrations. It can also produce high noise levels which can cause problems which limit their use due to ergonomic noise restrictions on the industrial process. On the other hand, such flow oscillations can be highly desirable in certain applications like fluids mixing in chemical and combustion industries.

Although opposing planar jets have a variety of applications, their aero-acoustic response and fluid mechanics behaviour have received very little investigation to date with only few studies in the literature considering such a flow configuration. Thus, it is essential for us to study this setup in order to reach a satisfactory understanding of the behaviour of such a system under various operating parameters. This study will accordingly help the industry to utilize this knowledge towards process control and optimization of the flow oscillation associated with the opposing planar jet system.

2.2.1 Opposing Jets

Opposing jets can be generally categorized according to the nozzle geometry. They can be circular, rectangular or planar shaped. The jets can operate in an unconfined space, or they can be confined by walls. Several studies were dedicated to opposing jets

in the reaction injection moulding process, most of them are circular in shape and confined by walls. Table 2-1 presents a brief description of some studies related to this application. Most of these studies focused on the process efficiency as input/output experimental parameters, moreover the opposing stream velocities were relatively low compared to the speed of sound. Only few studies reported an oscillation phenomenon in the opposing jets in reaction injection moulding (Wood et al., 1991, Teixeira et al., 2005, Santos et al., 2009), with almost no data about the oscillation fluid mechanics or the acoustic response of the system. Other studies were dedicated to chemical mixing reactors, in which opposing jets were reported to increase the mixing efficiency due to faster mixing rates in comparison to normal mixing reactor designs (Wei-Feng, et al. 2010, Mahajan & Kirwan 1996, Liu & Fox 2006). This assures that opposing jets have a promising future application provided that research dedicates enough effort to the dynamic behaviour and its oscillation mechanism so as to be able to control any flow oscillations and employ it for each specific application that the industry requires.

2.2.2 Square and Planar Shaped Opposing jets

Opposing jets of square shape have an importance in industries related to air/fuel mixing in combustion processes where such a mixing setup is beneficial for side-dump combustion applications in vertical takeoff and landing jets. In this application, the opposing jet instability results in pressure waves with frequencies that affect the performance of jet engines. On the other hand, square and planar shaped opposing jets

can be used in applications like micro-mixing and valve designs as reported by Tesař (2002, 2009).

Planar opposing jets are used in hot dip galvanization process. Hot dip galvanization is a process of producing sheet steel in which a vertical steel strip passes between two high speed planar air nozzles; each planar nozzle issues a jet that wipes the hot zinc off the steel sheet, leaving a thin coating over the steel sheet that protects it from oxidation. This wiping process is associated with high level of noise. In such industrial applications, planar opposing jet instabilities are key factor in operation, as jet oscillation can pose adverse effects on process quality. Planar opposing jets can also result in excessive undesirable vibrations due to jet instability. Moreover, during hot dip galvanization, ergonomic factors are very important for mass production. Noise regulations are strict regarding exposure times to high noise levels in the work place. In Canada, Ontario's regulations prohibit exposure to noise levels of 91 dBA more than two hours as shown in Table 2-2 (ACT 2006). Thus, investigation of the noise generation mechanism is essential in order to control and optimize production.

2.2.3 Opposing Jets Oscillation

The oscillation phenomenon of opposing jets has received little attention in the literature. To date, only few studies are known that tackled this topic. Limited data is available concerning acoustic response or fluid dynamic behavior of planar opposing jets. In this section we briefly introduce the work of authors who studied similar problems related to planar opposing jets; results of such work are summarized in Table 2-3.

Worker Maximum Exposure Time (hours)	Noise Level (dBA)
8	85
4	88
2	91
1	94
0.5	97
0.25	100

Table 2-2 Ontario Regulations Regarding Workplace exposure to noise

Among the earliest studies is the work done by Denshchikov et al. (1978). They studied the behavior of two plane water jets immersed in a water tank and impinging on each other, and assumed that the opposing planar jets are similar to two opposing air streams that collide in local hurricane formation phenomenon (boras). In that study, they found that the water jets oscillate perpendicular to the flow plane. They suggested that the oscillations are self-excited and can be determined by the system parameters; they derived empirical formulae for the flow oscillation as a function of flow speed and distance between planar water nozzles exits. In their efforts to find an explanation for the jet oscillation, Denshchikov et al. (1978) proposed a mechanism suggesting that these jets oscillate based on the pressure in the flow field. Although they didn't have any pressure data in the flow field, Denshchikov et al. (1978) suggested that when the jets collide, the pressure increases in middle region between the two jets due to the fact that the jets slow

down as they impinge on each other as shown in Figure 2-2a. This increase in pressure deflects both jets from their original direction, forming two deflected jet streams (shown in Figure 2-2b) and a new faster velocity flow region in between.

Such new higher velocity region is associated with a pressure decrease in the region between the two jets, this draws back the deflected jets to their original position as shown in Figure 2-2c, and then the jets deflect towards the opposite side, eventually resulting in the oscillatory manner as the cycle continues. Denshchikov et al. (1983) carried out further studies on their jets trying to specify the frequency of oscillation empirically and determine the range of onset of oscillation.

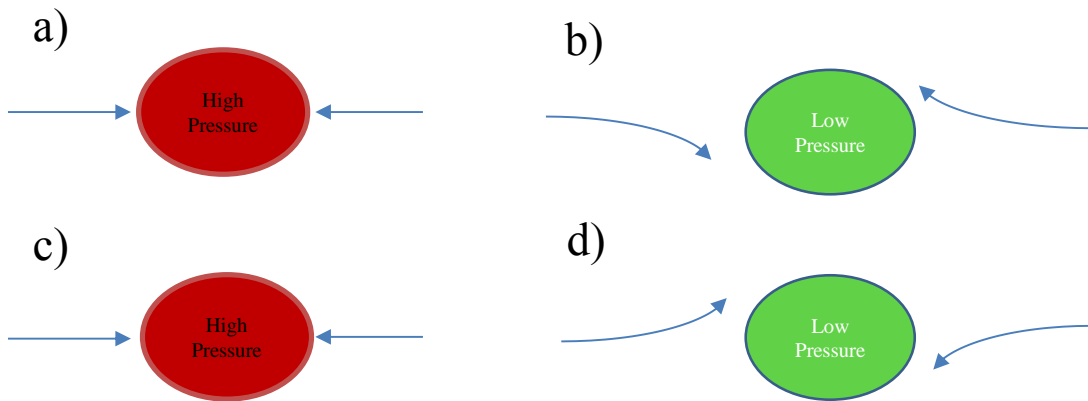


Figure 2-2 Schematic of suggested oscillation mechanism by

(Denshchikov et al., 1978)

Author (year)	Country	Set up geometry (Jet/Confinement)	Working Fluid	Exit Reynolds number or Exit Velocity	Velocity Measurement Apparatus	Strouhal number (St_d)
Santos et al. (2008)	Portugal	Circular (1.5mm) / Vertical Cylindrical (10X50 mm)	Glycerine + Water	Re = 250~500	LDA	0.099/0.04-0.05
Santos et al. (2008)	Portugal	Circular (1.5mm) / Vertical Cylindrical (10X50 mm)	Glycerine + Water	Re = 100~150	PIV	Not reported
Teixeira (2005)	Portugal	Circular (1.5mm) / Vertical Cylindrical (10X50 mm)	2 Aqueous	Re =50~600 V= 1.66~10.9 m/s	LDA	0.04
Berman et al (2000)I	Israel	Circular (5-10mm)/ Horizontal Cylindrical (18~60 X20~80 mm)	SO2-flue gas mix	7-20 m/s	N/A	Not reported
Berman et al (2000)II	Israel	Circular (2 mm)/ Horizontal Cylindrical (60X40mm)	SO2-flue gas mix	0.44-0.1 m/s	N/A	Not reported
Liu & Fox (2005)	USA	Circular (0.5mm) / Vertical Cylindrical (2.38X1 mm)	p=962.5 kg/m ³ , μ=0.001995 kg/m.s	0.14~16 m/s	CFD	Not reported
Gavi et al (2007)	Italy	Circular (0.5-1 mm) / Vertical Cylindrical (2.38X1 mm)	Aqueous solution 25% ethanol	Re= 704-2696 V=2.81~9.16 m/s	CFD	No Oscillation Reported
Johnson & Prud'homme (2003)	USA	Circular (0.5mm) / Vertical Cylindrical (2.38X1 mm)	Aqueous solution 25% ethanol	0.04~16.0 m/s	N/A	Not reported
Wu et al (2007)	China	Circular (80mm) / Vertical Cylindrical (750X950 mm)	Air and SO2	7~10 m/s	N/A	Not reported
Wood et al (1990)	Canada	Circular (2.38 mm) / Vertical Cylindrical (25.4X 159 mm)	Mineral oil	Re= 50-130	LDA	0.0083- 0.096

Table 2-1 Studies on Opposing Jets for Rejection Injection Moulding Application

Another attempt to characterize the opposing jets setup was a study done by Nosseir & Behar (1986). The authors also used water as a working fluid, with rectangular shaped nozzles and a confinement of two parallel plates. The aim of that study was modeling a side dump combustor. Nosseir & Behar (1986) reported jet oscillation and observed vortices located downstream of the confined space and near to the confinement boundaries. They reported that the vortex generation frequency is proportional to the jet velocity and inverse of confinement size. Thus, they suggested that downstream vortex generation frequency in the confinement is related to jet oscillation frequency.

Later, Nosseir et al. (1987) studied opposing round shaped air jets in a confinement, where they observed vortices at the edge of the jet along the confinement surface. They reported ‘‘symmetric’’ and ‘‘anti-symmetric’’ oscillation modes, where those oscillation modes were specified depending on vortex attachment to the edge of the jets. The authors also reported peak frequencies for the confinement surface pressure fluctuations, and categorized the frequency peaks into high and low frequencies. Nosseir et al. (1987) suggested that for the high frequency peaks; the oscillation resonance frequency satisfies a standing wave relationship based on the distance between the nozzles, while for the low frequency; they proposed a convective resonance model where they assumed a virtual sound source at the radius of reattachment of the flow after impingement. The authors of the later study also proposed a feedback mechanism to explain the self-induced vibrations producing these tones. On the other hand, concerning opposing jet oscillation in combustion chambers, Samaniego et al. (1993) were among those who proposed that the observed oscillation frequency was related to acoustic modes of the confinement.

Author	Working Fluid	Nozzles Aspect Ratio	Nozzles Exit Velocity	Nozzle Thickness	Impingement distance	Impingement ratio	Strouhal number St_z
Tesar 2002	Water	2.034	0.21 m/s	0.35 mm	1.26 mm	3.6	No Oscillation for that range
Tesar 2009	Water	0.44	0.14 m/s	3.4 mm	10.2 mm	3	0.12
Denshchikov et al. 1978	Water	20 and 11.4	0.02 to 0.2 m/s	0.4 to 0.7 cm	5 to 25 cm	Not Specified	0.166
Denshchikov et al. 1983	Water	26.66	0.2 to 1 m/s	0.3 cm	5 to 20 cm	Not Specified	Not Specified
Nosseir and Behar 1986	Water	Not Specified	4 to 5 m/s	4 cm	5.2 to 10	1.3 to 2.5	0.15 - 0.25
Nosseir et al. 1987	Air	Circular Nozzle	1 m/s	D=4.87 cm	4.87 to 20 cm	1 to 2.5	0.11 - 0.25
Samaniego et al. 1993	Propane-Air mixture	12	15 to 100 m/s	5 mm	70 mm	14	0.1 to 0.2
Johnson and Wood 2000	mineral oil	Circular Nozzle	1 to 5 m/s	2 to 4 mm	20 and 25.4 mm	5 to 10	0.08 to 0.26
Kim et al. 2003	Nitrogen	> 20	125 m/s	1 mm	20 mm	20	0.16
Arthurs et al. 2008	Air	> 20	100 m/s	1 mm	5 mm to 30 mm	5 to 30	0.105 to 0.15
Wei-Feng Li et al 2010	Air	15	1.18 to 9.44	10 mm	10 to 200 mm	1 to 20	0.1 to 0.2
Wei-Feng Li et al 2013	Air	12	1 to 13 m/s	2.77 mm	2.77 to 83.1 mm	1 to 30	0.195

Table 2-3 Summary of previous studies related to opposing jets instability

Some more recent studies were done, such as Johnson & Wood (2000) who performed an experiment of a round mineral oil jet-jet impingement in an enclosure of both rectangular and round shaped at low flow speeds ($90 < Re_d < 150$), however, their study focused on specifying the range of the onset of the oscillation. While others like Kim et al. (2003) numerically studied the behavior of two planar opposing jets to better understand the cause of over-coating at the sheet steel edge in hot dip galvanization. They predicted that planar opposing jets will oscillate and their oscillation frequency will increase as the distance separating the nozzle decrease, no experimental data was available to confirm those predictions. Lately, Arthurs (2007) and Arthurs et al. (2008) reported that high sound pressure level acoustic tones are generated at low frequencies by the opposing planar jets used in sheet steel galvanizing lines.

Several authors reported that the dynamic behaviour of planar jets is considerably different from that of axisymmetric jets (Wei-Feng, et al. 2010). For instance, Arthurs & Ziada (2011, 2012) showed that impinging planar jets oscillate over a wider range of Mach number and impingement distance than those of axisymmetric jets. Wei-Feng et al. (2010) performed limited experiments at low flow speed using smoke wire technique for axisymmetric and planar jets, and showed differences between both setups. Lately, Wei-Feng et al. (2013) continued their experiments on low speed opposing jets using smoke wire visualization and high speed camera; They reported ‘deflecting’ opposing jets oscillation and regarded that behavior to originate from anti-symmetric structures which appear downstream in low speed free planar jets (Michalke, 1972), and described the

oscillation to be self-sustained by ‘periodic pressurizing and release of pressure in the impingement region’.

Despite all previous attempts, the unsteady flow field of the opposing jets remains largely unexplored, especially at high flow velocities comparable to those used in industrial applications.

2.3 Objectives

Based on the previous overview of state of knowledge regarding the opposing planar jets, the objective of the current study is to bridge the gap between the insufficient experimental data on planar opposing jet oscillation and its acoustic response at higher speeds. Thus, in this study we experimentally investigate the aero-acoustic behavior of two high speed subsonic opposing planar air jets. This objective is achieved in two stages:

- Stage I: Investigate the acoustic tone of the system under different operating parameters in order to understand how these parameters control the acoustic tone.
- Stage II: Investigate the fluid dynamics of the system in some detail in order to understand the nature of the flow oscillation.

In the following chapter, the experimental set up will be presented in detail in order to provide knowledge of the jet system and the measurement facilities.

Chapter 3: Experimental Setup

In this Chapter we provide an overview for the experimental setup of the current study, with description of the used equipment and its assembly. Detailed specifications and data sheets for the used equipment can be found in Appendix IV.

3.1 Nozzles Geometry

Planar air nozzles were used for this study; Figure 3-1 represents one of the two identical CNC machined aluminum nozzles that were available for use. Each nozzle has a span length of $L= 100$ mm and an adjustable thickness. The thickness used for the current experiments was adjusted to be $h= 2$ mm using high precision filler gauges (± 0.01 mm). The overall aspect ratio of each nozzle was $L/h=50$. Conditioning screens were positioned before the nozzle contraction area in order to provide uniform air flow.

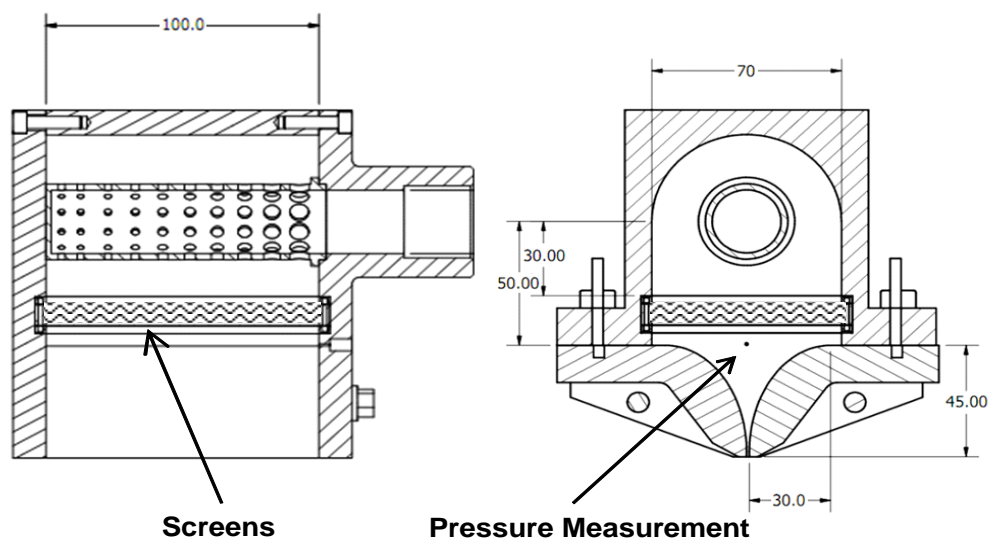


Figure 3-1 Planar Air Nozzle (Dimensions in mm)
(Drawings are adopted from Arthurs & Ziada, 2012)

The conditioning screens are made of a fine stainless steel cloth-like material, with 70 wires per inch and an open area ratio of $\beta \approx 0.58$. For the contraction geometry, nozzles had an elliptical profile as shown in Figure 3-1, major and minor dimensions of ellipse axes were 45mm and 30mm respectively, where the major ellipse axis was positioned parallel to the jet flow direction. Each nozzle contraction ratio is $\sim 35:1$ for a nozzle thickness of $h=2$ mm.

Compressed atmospheric air was used for this study; a schematic for the air supply system is shown in Figure 3-2. A constant pressure air supply of 80 psi was available. Air passes through a 2 inch pressure regulator in the beginning of the line, followed by a 2 inch globe valve, 2 inch gate valve. Air then enters a T-shaped manifold, where the air flow is controlled by a 1 inch pressure control valve for each nozzle. Air then enters jet plenum through a 25.4 mm diameter hose adapter. Afterward, air enters a flow distribution tube shown in Figure 3-1 which was designed to provide even distribution of the flow along the jet span.

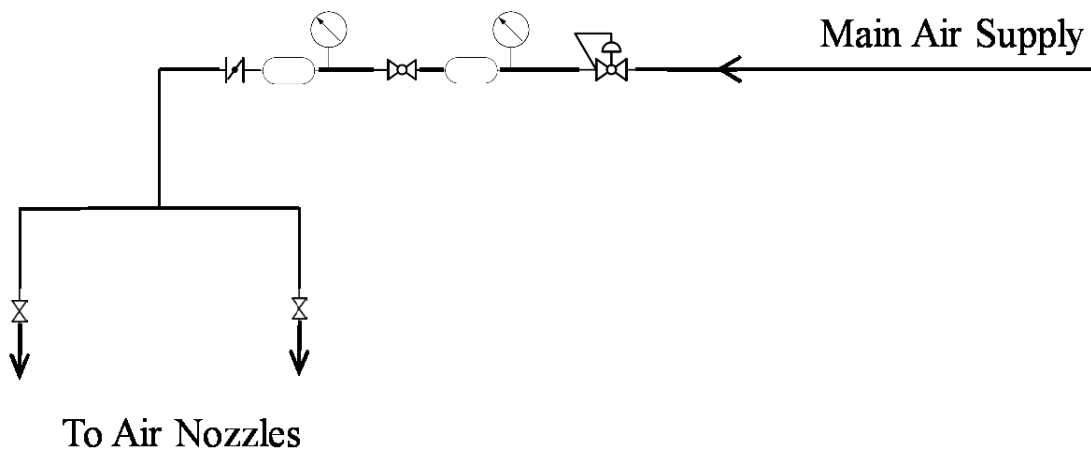


Figure 3-2 Schematic for the Air Supply System

3.2 Nozzles Setup

The two air nozzles were set in a special way for the current study. Figure 3-3 shows a 3-D virtual image of the setup. Each nozzle was bolted to a Newport™ 481-A series high-performance rotation stage with a sensitivity of 30 arc sec and a resolution of 0.008° . One nozzle-rotation stage assembly was mounted on a manual Velmex™ 2.5 inch wide A25 series screw drive UniSlide Vice with a resolution of 0.01 mm. The second nozzle-stage assembly was mounted on an electric motor operated vice which was controlled by a PC using Cosmos® software. The electric motor-vice system consisted of a model VXM-3 Velmex™ power supply with Slo-syn stepper motors; the system could linearly move the nozzle with a resolution of 50 microns. The two vices carrying each nozzle-stage assembly were positioned perpendicular to each other then were bolted to a 1 inch thick rectangular plate made of steel. The steel plate carrying the nozzles was mounted on 3 leveling screws and placed on the experiment table.

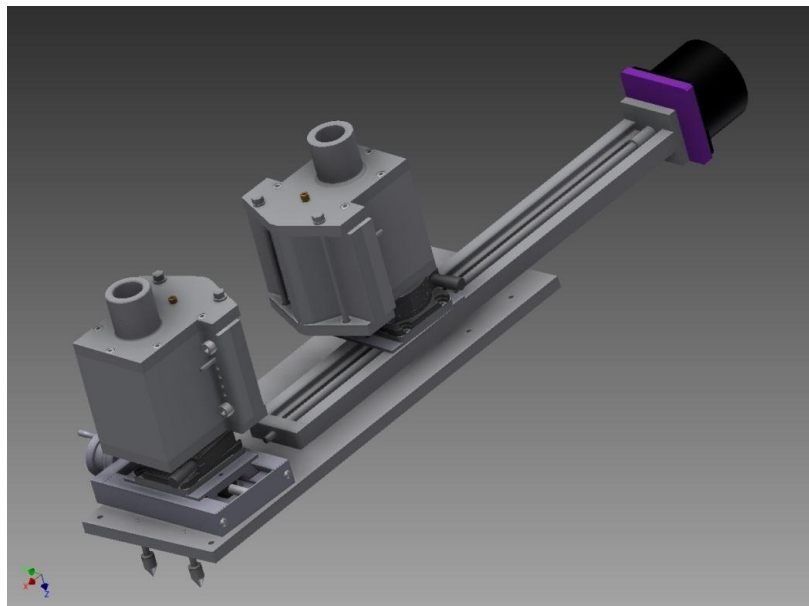


Figure 3-3 Nozzles Setup (Virtual Image)

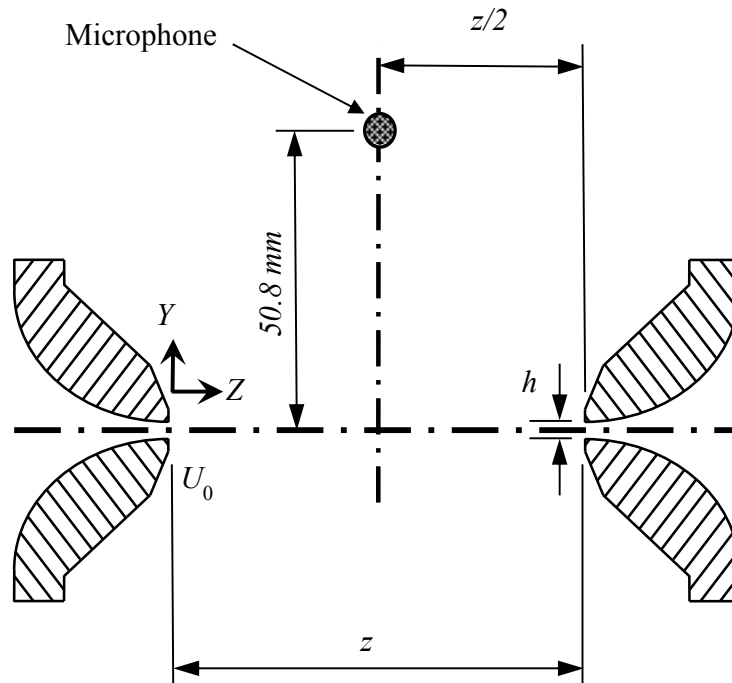


Figure 3-4 Opposing Planar Jet System Parameters

Figure 3-4 shows the opposing planar jets operation parameters, the axes are defined as Z and Y , where Z is the axis parallel to the downstream flow direction (parallel to the common centerline of the two jets), and Y is the axis parallel to the cross stream flow direction (perpendicular to the common centerline of the two jets). The nozzles have a width denoted by h and they issue air at an exit velocity U_0 . The distance separating the two nozzles' exits is denoted by z . Another system parameter is the impingement ratio which is defined as the ratio between the distance z and the nozzle width h .

3.3 Acoustic Tone Measurements

Measurements in the acoustic free field were obtained using a GRAS™ model 40BP ¼" high-level microphone. The microphone has a flat frequency response of 4 Hz-70 KHz ($\pm 2\text{dB}$). The microphone then connects to a GRAS™ model 26AC preamplifier

that has a flat frequency response of 2.5 Hz-200 kHz (± 0.2 dB). The microphone-preamplifier assembly is powered by GRAS™ model 12AA 2-channel power supply module with a flat frequency response of 3.5 Hz - 200 kHz (± 0.2 dB) set to a +20 dB gain. This system was calibrated using a GRAS™ Type 42AB sound calibrator. The microphone was mounted on an aluminum adapter connected to a 0.5 inch steel bar; then the bar was bolted to a motor operated / PC controlled electronic Velmex™ vice (having 50 microns resolution) similar to the one carrying one of the nozzles. Mounting the microphone to the electronic controlled vice system allowed a precise adjustment of the position of the microphone. The microphone was positioned at a distance of 50.8 mm from the midpoint between the exit of two nozzles and perpendicular to the line connecting the two nozzle exits. The microphone was positioned on a vertical plane that is located 25.4 mm above the nozzles' top surface plane. The microphone location was chosen out of the flow interaction plane so as not to interfere with the fluid flow field and at the midpoint between the two jets at a symmetry point. The microphone location has a minor effect on the acquired acoustic tone; such effect is outlined in Appendix III.

Data acquisition was performed using a National Instruments NI-9234 data acquisition card of 24-bit resolution and 102 dB dynamic ranges. The acoustic tone measurements were done by acquiring the pressure time signal at a sampling rate of 51.2 kHz for 50 seconds. Spectral analysis was performed by breaking the time signal into 100 equally sized blocks of 51,200 samples with 50% overlap, where the effects of averaging on acoustic spectra and choice of 100 acoustic tone samples are discussed in Appendix III. Labview® software was used for data acquisition; the software calculates the ampli-

tude spectrum of RMS acoustic pressure for each time signal block. Then, the resulting spectra was averaged; for each measurement case 100 frequency spectra were averaged to produce a final average acoustic spectrum. Each resultant amplitude spectrum has a frequency range from 0 Hz to 26.5 kHz which corresponds to the linear range of the system and a spectral resolution of 2 Hz. The average spectrum was truncated to a range of 0 Hz to 3000 Hz for viewing purposes.

3.4 Flow Field Measurements

3.4.1 Exit Velocity Profile

Nozzle exit velocity was calculated based on the nozzle plenum pressure. The nozzle plenum static pressure was measured using a Validyne[®] DP-15 pressure transducer fitted with an 8.0 Psi diaphragm that has full scale accuracy of $\pm 2.5\%$, it was calibrated using a Crystal is33 pressure calibrator and Ralston DPPV-0000 air pump. The transducer measures the static pressure at a centerline point positioned in the middle of the nozzle contraction as shown in Figure 3-1. By measuring nozzle plenum static pressure, flow velocity at the nozzle exit can be calculated using the following equation.

$$M = \eta \sqrt{\frac{2}{\gamma - 1} \left[\left(\frac{P + P_\infty}{P_\infty} \right)^{\frac{\gamma - 1}{\gamma}} - 1 \right]} \quad (3-1)$$

where γ is the ratio of specific heats of air, P and P_∞ are the static pressure in the nozzle and the ambient pressure respectively, and η is the isentropic efficiency of the nozzle. The

isentropic efficiency of the nozzle (η) was found to be in excess of $\eta=0.96$ for a complete range of Mach number (Arthurs & Ziada, 2012).

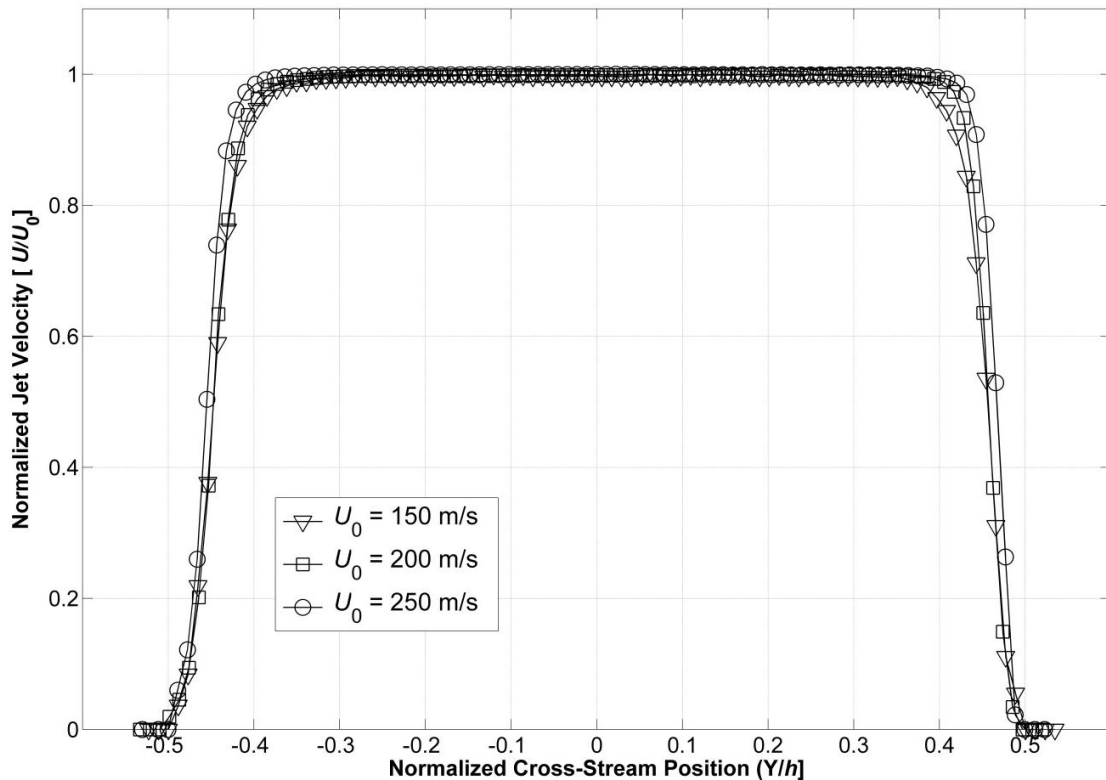


Figure 3-5 Normalized Jet Velocity profile for nozzles at exit nozzle velocities of $U_0=$ 150, 200, 250 m/s. (Private Communication from Arthurs)

The calculated nozzle exit velocity based on plenum static pressure was confirmed by measuring the exit velocity profile using a total pressure transducer that was previously used by Arthurs & Ziada (2012) to measure the exit velocity profiles for the same nozzle. Figure 3-5 shows the corresponding non-dimensional velocity profiles at exit nozzle velocities of $U_0= 150$, 200, and 250 m/s respectively, the velocity profiles are top-hat shaped with a very thin shear layer present at the edge of the flow. The exit nozzle veloc-

ity, using equation (3-1), was also confirmed by the velocity measurements using particle image velocimetry performed in this study.

Table 3-1 shows a summary of values for the boundary layer thickness δ and displacement thickness δ^* and momentum thickness θ for the nozzle measured velocity profiles at exit nozzle velocities of $U_0 = 150, 200, 250$ m/s. It is observed that the value of the boundary layer thickness δ decreases as the exit nozzle velocity increases, which is a characteristic of boundary layer flows, while the value of the displacement thickness and the momentum thickness slightly decreases as the velocity increases as well. The boundary layer thickness remains in the range around $\sim 15\%$ of the total jet thickness. The shape factor of the boundary layer is relatively high for the tested exit nozzle velocities and varies between 3.71 and 4.82. These values of shape factor means that the boundary layer at the exit of nozzle acts like a laminar boundary layer at the exit before developing into the flow field. This laminar boundary layer arises from the used nozzle contraction outlined in Figure 3-1, where the high contraction ratio stabilizes the flow over the inside curved boundary of the nozzle as the flow accelerates.

It comes to no surprise that the shape factor in this the current study is relatively higher than that of investigated by Arthurs & Ziada (2012), where the contraction ratio in the current nozzle is substantially higher than that of the latter study which creates more stabilizing effect and thus increase the shape factor of the velocity profile.

	$U_0=150$ m/s	$U_0=200$ m/s	$U_0=250$ m/s
Boundary Layer thickness δ [mm]	0.381	0.32	0.203
Disturbance Thickness δ^* [mm]	0.128	0.103	0.089
Momentum Thickness θ [mm]	0.034	0.021	0.018
Shape factor $H = \delta^* / \theta$	3.73	4.9	4.85

Table 3-1 Shear layer thicknesses (δ , δ^* , θ) and shape factor (H) at exit nozzle velocities of $U_0 = 150, 200, 250$ m/s.

3.4.2 Particle Image Velocimetry (PIV)

Flow field measurements were done using a two dimensional Particle Image velocimetry system built by TSI[®]. The high aspect ratio of the nozzle geometry (Aspect Ratio, AR= 50) and the periodic oscillation exhibited by the jets allows us to assume that the flow is two dimensional; where the 3rd component of the velocity vector in the direction of the nozzle span vanishes. The effect of aspect ratio on the 2 dimensionality of the flow was previously studied by several authors such as Deo (2005) and Mi et al. (2005), who both confirmed that the flow can be assumed as two dimensional in excess of AR=30. Moreover, two dimensional flow measurements were captured at different span wise vertical planes, and same flow fields were observed. Thus, a two dimensional PIV system was suitable for capturing flow fields in this study.

Figure 3-6 shows an isometric virtual image of the experimental setup of the used opposing planer jet system equipped with the PIV system. As shown, a laser sheet is projected in a horizontal plane which is perpendicular to the span of the jet, and a high speed camera is positioned above the laser sheet plane to capture images of the flow.

A special seed material was used to track the air particles in the flow fields, the commercial name of the seed material is Bis(2-ethylhexyl) sebacate, having a technical grade of 90% and its linear chemical formula is $[-(\text{CH}_2)_4\text{CO}_2\text{CH}_2\text{CH}(\text{C}_2\text{H}_5)(\text{CH}_2)_3\text{CH}_3]_2$. The seed material is issued through a seeder machine model no. 9307-6 manufactured by TSI[®]. The seeder machine is operated via compressed air and it produces seed particles of a 1 micrometer diameter. The smoke-like seed issued from the seeder machine mixes with incoming supply air in a T-shaped pipe junction positioned before the nozzle air control valves to ensure fair distribution of air seed among the two nozzles.

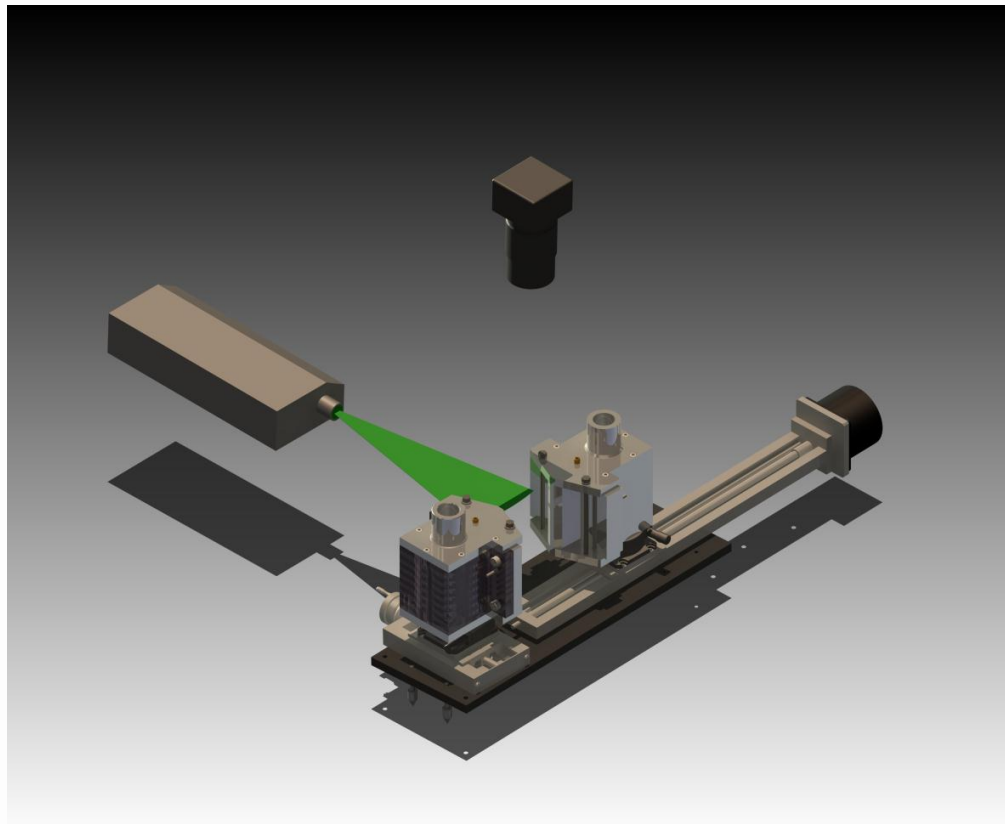


Figure 3-6 PIV Experimental Setup

3.4.2.1 Laser and Image Acquisition

The flow field was illuminated by a 532nm New Wave Solo 120XT pulsed Nd:YAG laser. The laser had an adjustable output with a maximum of 125 mJ per pulse; this maximum output was used for capturing flow field in the current study. The laser passes by a 500 mm focal length spherical lens then a -15 mm focal length concave lens to produce an illuminating laser sheet. The laser machine was positioned at a distance of 70 mm away from the centerline of the two jets and was leveled to issue a flow illuminating laser sheet located at the mid span horizontal plane of the air nozzles as shown in Figure 3-6. Laser pulse timing was controlled by a TSI[®] laser pulse synchronizer model 610035.

The flow field image acquisition was done by a single PowerView[®] 4 mega pixel 12 bit digital camera with a resolution of 2048×2048 pixels. The camera was positioned at a vertical elevation of 70 mm above the laser sheet. The camera was equipped with optics consisted of a Sigma[™] 105 mm *f* 2.8 lens, a Teleplus[™] model MC4 1.4X magnifying lens and Kenko[™] 20 mm extension tube.

For the tested operating conditions a time difference of 450 nanoseconds between two consecutive images was adjusted to achieve each frame of flow field. A vector validation of more than 99 % for all measured velocity fields was attained in the current study. An error analysis showed that the maximum occurred stream wise velocity displacement gradient had a value of $(\partial u/\partial y)_{\max} = 0.1$ pixel/pixel. While the cross stream displacement gradient had a value of $(\partial v/\partial x)_{\max} = 0.011$ pixel/pixel. This corresponded to

uncertainty in particle displacements of $\varepsilon_u = 0.06$ pixel in stream wise direction and $\varepsilon_v = 0.004$ pixel in the cross stream direction. This accordingly resulted an uncertainty in velocity gradients of $\varepsilon_{\left(\frac{\partial u}{\partial y}\right)} = 0.0096$ pixels/pixel and $\varepsilon_{\left(\frac{\partial v}{\partial z}\right)} = 0.0006$ pixels/pixel, which eventually led to relative uncertainty in vortices gradients of $\varepsilon_{(\partial u/\partial y)/(\partial u/\partial y)_{\max}} = 9.6\%$ in stream wise direction and $\varepsilon_{(\partial v/\partial x)/(\partial v/\partial x)_{\max}} = 5.4\%$ in the cross stream direction. Details about the PIV measurements uncertainty can be found in Appendix III. Vector fields were processed using insight 3G software provided by TSI[®]. To obtain vector fields, image processing was performed using multi-grid, 1st order deformation correlation scheme with Gaussian sub-pixel interpolation. A multi-grid refinement step was used with a series of iteration steps for the interrogation window. Window sizes of 32×32 and 8×8 pixels were used for the initial and final interrogation regions. Vector processing and frame adjustment resulted 391×360 vector points per frame.

3.4.2.2 Phase Lock Measurement technique

Flow measurements in this study were performed using the phase-averaged measurement technique; this method uses the acoustic tone pressure signal acquired by a microphone to trigger PIV measurements at a particular instant in the flow oscillation cycle. A similar unsteady flow measurement technique was employed previously by Arthurs & Ziada (2012), Fleming et al. (2012), and Kim et al.(2002). A simple illustration for phase locking is shown in Figure 3-7, where the measurement frame is acquired at a certain designated point with respect to the shown sinusoidal signal. The signal in our study was an instantaneous acoustic signal acquired by the same setup used for acoustic tone meas-

urement. In order to avoid the noise associated with the main tone coming from the experiment, two 2nd order Butterworth HI/LO pass analogue acoustic filters with adjustable cutoff frequencies were added to our system. The cut off frequencies were adjusted to be 280 Hz for the high pass filter and 150 Hz for the low pass filter where the investigated fundamental tone frequency was $f_0=226$ Hz.

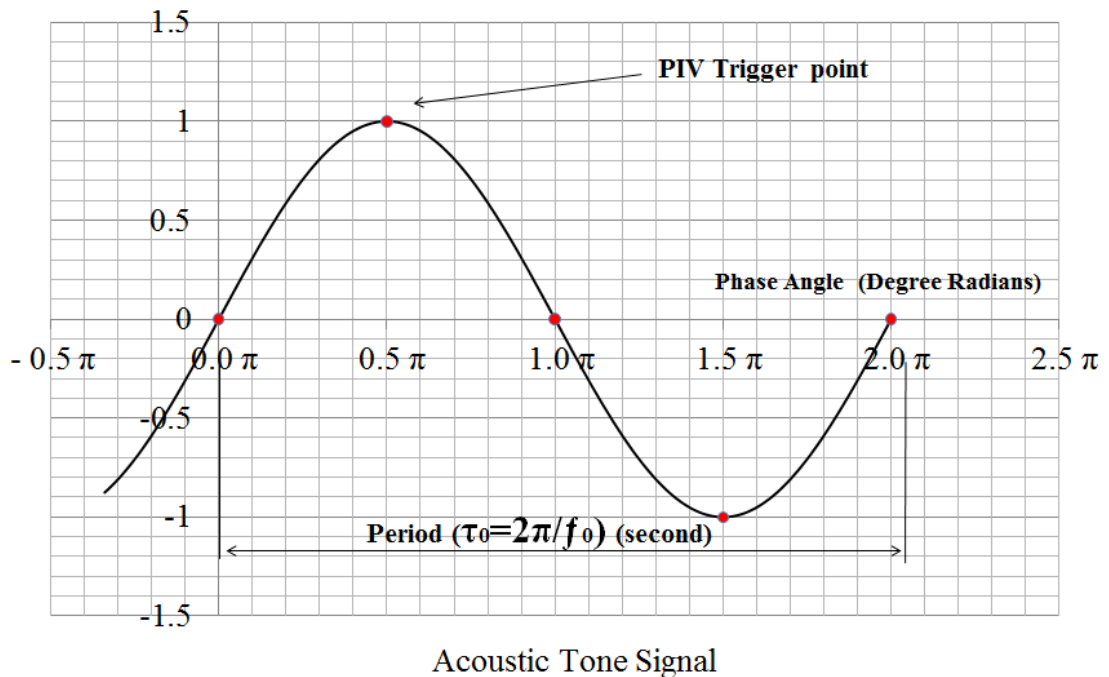


Figure 3-7 Phase-Locking Illustrated

The filtered acoustic signal is then fed into a custom designed trigger generator circuit that uses an input acoustic signal and outputs a triggering pulsed signal at a predefined point of the input signal. The output trigger signal is then sent to the laser synchronizer that operates the laser to capture the velocity field at this instant. To obtain flow fields at multiple instants of the flow oscillation cycle, a calculated time delay is added between the trigger signal and the laser operation instant. A number of flow fields (instan-

taneous frames) are obtained for each point (instant) in the oscillation cycle. Those *phase-locked* flow fields are then averaged to obtain a phase-averaged flow field at each point of the flow oscillation cycle. Then, by combining these *phase averaged* flow fields, the average flow oscillation cycle can be constructed.

For the current study, *phase averaged* flow fields were obtained at a series of eight phase angles (instants) distributed evenly over the flow oscillation cycle with 100 *phase-locked* flow fields being averaged at each point in the phase. Phase averaging was performed by a fluid flow toolbox provided by TSI[®] using Tecplot[®] software. The process of phase averaging removes small random turbulent velocity fluctuations associated with the flow and leaves out the large scale periodic velocity fluctuations related to the oscillation of the flow field.

Chapter 4: Results and Analysis

In this chapter, we present the results of the experimental study of the two opposing planar jets. The first part of this chapter presents how acoustic tone data was processed and analyzed, then results are provided showing acoustic response of the system when varying the two main operating parameters; first, the impingement ratio (z/h) which was defined earlier as ratio of the distance between the two nozzles exits to the nozzle width; and second, the nozzle exit velocity (U_0).

The second part of this chapter outlines the fluid dynamic behavior for a chosen case of $z/h = 50$ and $U_0 = 200$ m/s. First, the post-processing method of flow field is presented. Thereafter, results of flow field parameters that show the oscillation cycle are provided (Velocity Magnitude, Stream-wise and Cross-stream Velocity Components, Vorticity field, and Streamlines). Then the average flow field is given over the oscillation cycle along with the oscillating components for selected flow field quantities. This helps in revealing the oscillation phenomenon. Finally, an explanation is provided for the system oscillation with the aid of results shown, and with the help of a preliminary computational fluid mechanics (CFD) simulation for the system using the same operating conditions as the chosen experimental case that we investigated.

4.1 Acoustic Response

4.1.1 Acoustic Tone Data Analysis

The acoustic tone data was acquired for each measurement setup. First, each nozzle is manually adjusted by the rotary stage so that the two jets have the same centerline. Second, the two jets are positioned opposite to each other at the desired distance between the nozzle exits using the electronic stepper motor vice which is controlled by a PC. Third, the air flow into each nozzle is adjusted so that the two jets have the same exit nozzle velocity. Finally, the microphone sends the acoustic signal to the data acquisition system which accordingly inputs it into Labview software. A customized acoustic data viewing and acquisition program was constructed on Labview which outputs the following data in *.lvm file format: frequency [Hz] against acoustic pressure [Pa] and sound pressure level [dB], the average nozzle pressure for the two nozzles along the measurement run [Bar], and the nozzle exit velocity for the two nozzles [m/s] calculated from Eqn. 3-1 (See Chapter 3). Each of these *.lvm files is then imported into Matlab software using a special coded function available on Mathworks website (Hopcroft, 2008), which then can be plotted using Matlab.

A sample acoustic tone measurement is shown in Figure 4-1, where this measurement was taken at $U_0 = 260$ m/s & $z/h = 40$. The sound pressure level SPL [dB] ($P_{\text{ref}} = 20 \mu\text{Pa}$) is plotted against the frequency [Hz], with a spectral resolution of 2 Hz. The tone spectrum was truncated to the desired ranges of 6000 Hz and 3000 Hz for

viewing purposes. As shown in Figure 4-1, a sharp peak representing a pronounced acoustic tone is observed at a fundamental frequency of $f_0 = 400$ Hz and its amplitude reaches about 106 dB. Several harmonics are also present at multiple integers of the fundamental frequency f_0 .

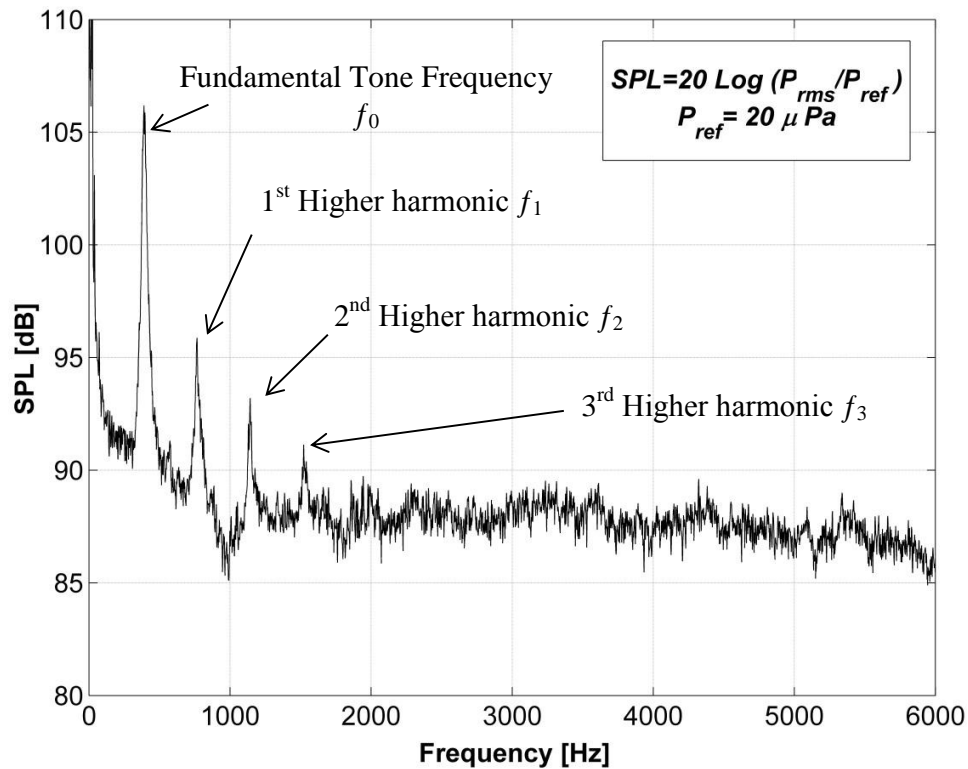


Figure 4-1 Spectrum of the Microphone Signal at $U_0 = 260$ m/s & $z/h = 40$

This process of data acquisition is repeated for each measurement case by variation of the following parameters: (a) variation of impingement distance (z/h) at a constant exit nozzle velocity (U_0), and (b) variation of exit nozzle velocity (U_0) at a constant impingement distance. This allows us to construct waterfall plots (Figure 4-2)

that map the acoustic tone along the variation of the parameters (a) and (b). The waterfall plots are plotted using the function `plot3` in Matlab software after running a special custom-made code by the author to organize the imported *.lvm spectra data files in matrices to be able to plot them easily.

Additional detailed analysis of the acoustic tone data, such as peak tone frequency f_0 [Hz] and peak sound pressure level (Peak SPL) [dB] detection was done for each measurement case. The spectral peaks were detected using a special coded function available on Mathworks website (Yode, 2009). This function simply returns peaks locations for a 1-D array of SPL data (with adjustable threshold and selected array data), and the peak locations are then matched with the corresponding frequency and SPL from the constructed frequency-SPL matrices using a custom made Matlab coded by the author. This peak detection method was tested against manual peak detection from the frequency-SPL matrices and proved successful and reliable before being used. Once peak frequencies and SPL are detected for each measurement, Strouhal Number St can be calculated, and thus all previous quantities were plotted for analysis shown in the following section.

4.1.2 Effect of Impingement Ratio

In this section, the effect of changing the impingement ratio (z/h) on the acoustic response of the opposing planar jets is investigated. Three sets of experiments were performed, and in each set, the impingement ratio is changed at a constant exit nozzle

velocity. The impingement ratio was varied from $z/h=7$ up to 130 by changing the distance between the nozzles exits z . This was done for each of the runs having a constant nozzle exit velocities of $U_0= 150, 200$ and 250 m/s. The microphone that measured acoustic tone time signal was positioned at a midpoint location between the two jets at all times despite varying the distance between the nozzles z . This was achieved with the help of an electronic controlled vice which the microphone was mounted on.

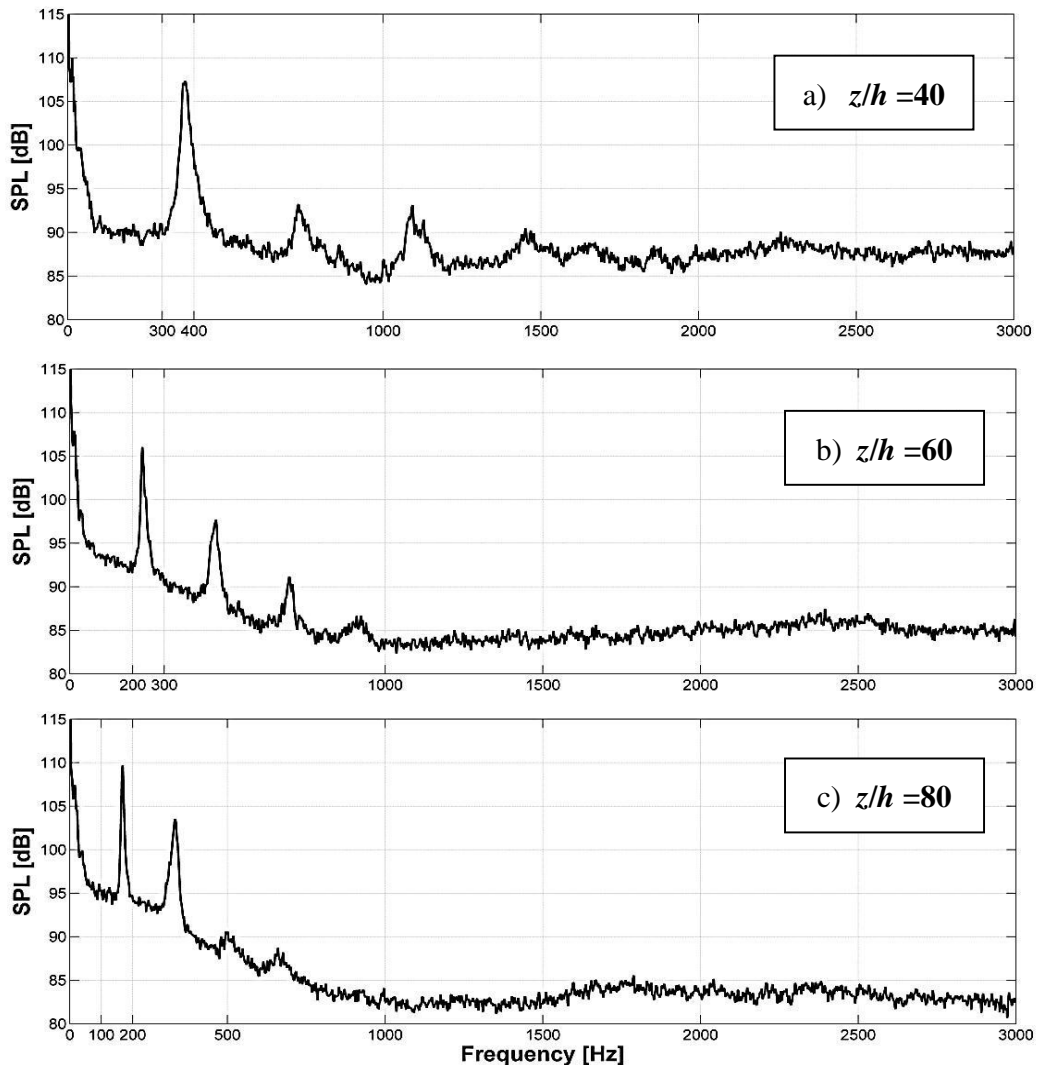


Figure 4-2 Acoustic Tone Response Spectra at three different impingement ratio a) $z/h = 40$ b) $z/h = 60$ c) $z/h = 80$, respectively at nozzle exit velocity $U_0= 250$ m/s

Figure 4-2 shows the acoustic tone at different impingement ratios. In Fig. 4-2a we observe the fundamental tone at frequency (f_0) of 372 Hz for an impingement ratio of $z/h= 40$, while in Fig. 4-2b, the corresponding fundamental tone frequency (f_0) shifts to the left to be 230 Hz for an impingement ratio of $z/h= 60$. Finally, in Fig. 4-2c, the fundamental tone at (f_0) shifts to the left again to be 168 Hz for an impingement ratio of $z/h= 80$. This behavior can be better observed by plotting a waterfall plot that shows the tone spectra over the whole investigated range of impingement ratios.

Accordingly, in the following part of this section, waterfall plots are presented for the acoustic response of the system for the previously mentioned set of experiments. These plots are useful as noise maps for our systems that give a general overview of both the sound pressure level and frequency behavior at the impingement ratio changes for each set of experiments. In Figure 4-3, the system acoustic response for an exit velocity of $U_0= 150$ m/s and a variable impingement ratio is observed. There are two main features for the acoustic response of our system; first, the existence of a distinct well defined fundamental tone at a frequency (f_0) accompanied by at least two higher harmonic tones (f_1, f_2). The second feature is that the tones frequency exists over a very wide range of impingement ratio. This frequency trend is certainly distinctive in comparison to those observed for other planar jet cases, such as the jet-edge, the jet-wall impingement. In the later cases, frequency jumps and discontinuities may exist when the operating conditions change over a wide range. This poses a question on the nature of the mechanism that governs this kind of oscillation phenomenon.

Figure 4-4 and Figure 4-5 show the acoustic response of the opposing planar jet system at exit flow velocities of $U_0 = 200$ m/s and $U_0 = 250$ m/s, respectively. In comparison to Figure 4-3, it is observed that the acoustic tone pattern is slightly shifted to the right in both Figures 4-4 and 4-5, moreover higher harmonic tones (f_1, f_2) appear to be better defined and persistent over the investigated range. In Figure 4-5, additional higher harmonic tones (f_3, f_4, f_5) appear and are observed to have a much lower SPL and a slight persistence over the range of impingement ratio.

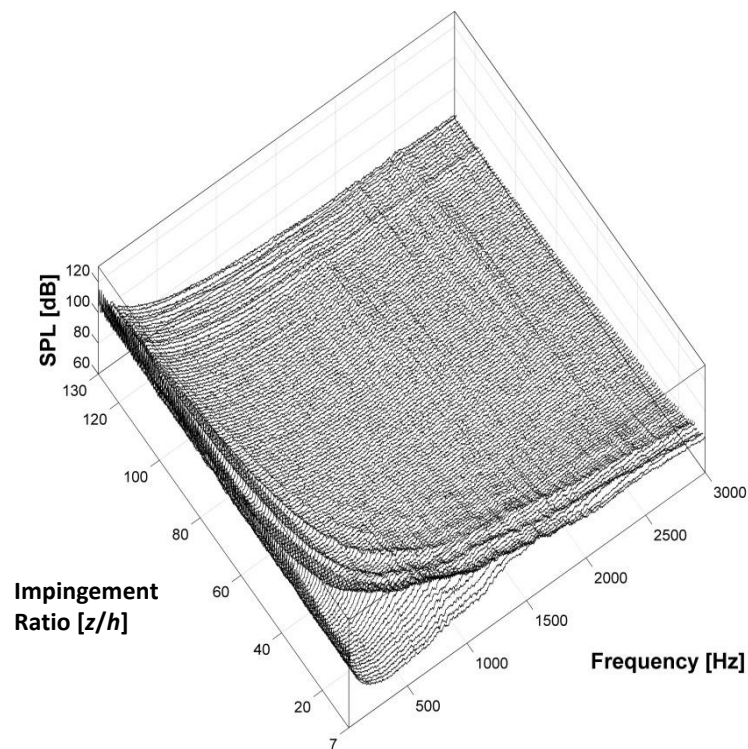


Figure 4-3 Waterfall plot showing acoustic response of opposing planar jets at Exit flow velocity $U_0 = 150$ m/s and impingement ratio $7 \leq z/h \leq 130$.

With the aim of further specifying the behavior of the main acoustic tone frequency of the system, Figure 4-6 shows the fundamental acoustic tone frequency (f_0) behavior versus changes in the impingement ratio (z/h) for the 3 investigated flow

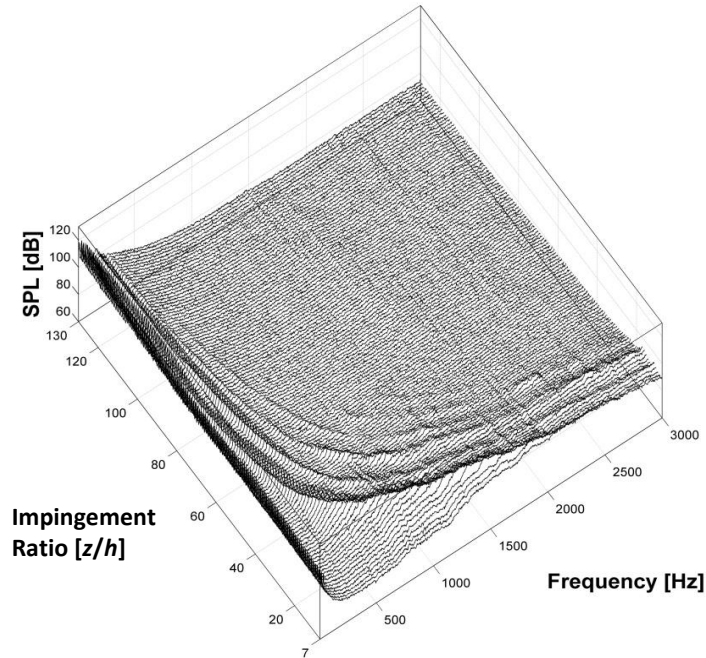


Figure 4-4 Waterfall Plot showing acoustic response of opposing planar jets at Exit flow velocity $U_0 = 200$ m/s and impingement ratio $7 \leq z/h \leq 130$.

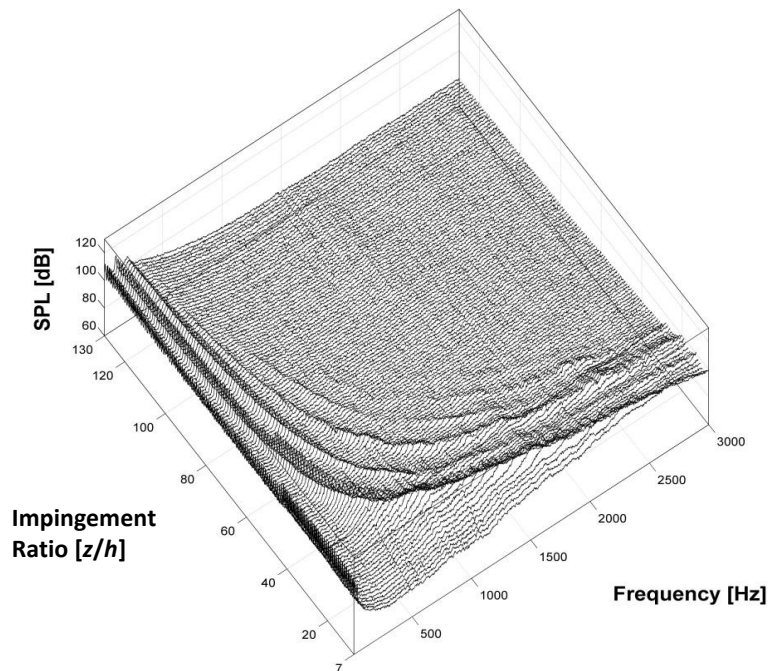


Figure 4-5 Waterfall Plot showing acoustic response of opposing planar jets at Exit flow velocity $U_0 = 250$ m/s and impingement ratio $7 \leq z/h \leq 130$.

velocities of $U_0 = 150, 200$ and 250 m/s which were shown previously using waterfall plots. We observe that for the 3 investigated flow velocities ($Ma \approx 0.44, 0.59$ and 0.73 , respectively), the frequency varies inversely with the impingement ratio (z/h), where the fundamental frequency (f_0) falls from the highest value of 2662 Hz down to 64 Hz over the whole investigated range of velocities and impingement ratios with a *hyperbolic* trend. Comparing the 3 plots in Figure 4-6, we observe that higher exit velocity (U_0) always had higher frequency (f_0) at the same impingement ratio z/h . Moreover, there were no frequency jumps, discontinuities, or hysteresis effects during the investigation where the system proved to be highly robust during variation of both impingement ratio and exit nozzle velocity.

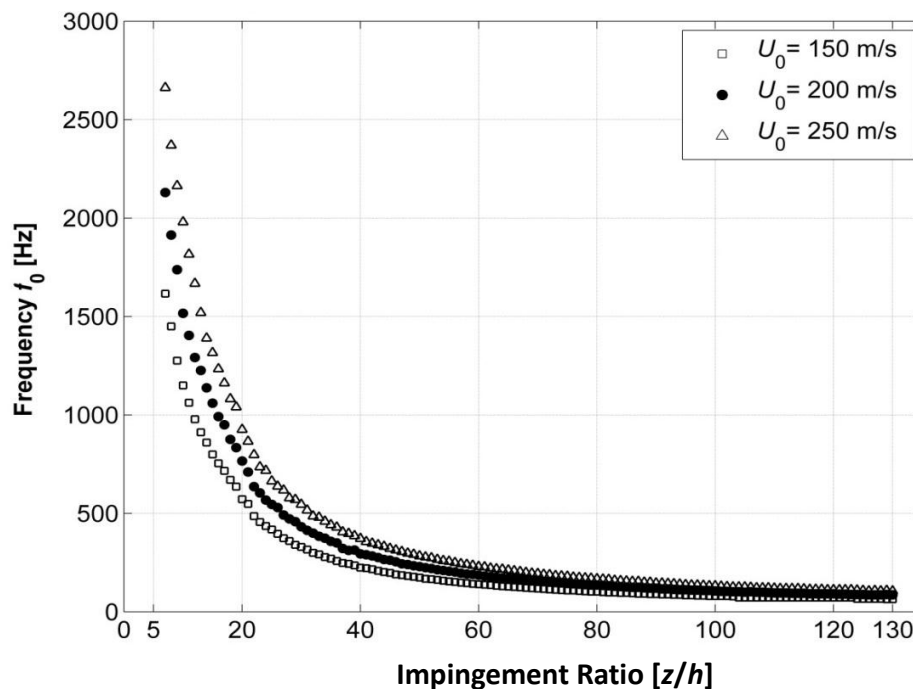


Figure 4-6 Plots for Acoustic Tone Fundamental Frequency f_0 as a function of the impingement ratio z/h for three jet exit velocities $U_0 = 150, 200$ & 250 m/s.

The first step in understanding the oscillation mechanism after observing the fundamental frequency behavior for the system is finding the appropriate length scale that should be used to non-dimensionalize the frequency. The Strouhal number ($St_z = f_0 z / U_0$) is plotted versus impingement ratio by using the impingement distance between the two nozzles z as the characteristic length scale and the nozzle exit velocity (U_0) as a velocity scale. In Figure 4-7, the Strouhal number is observed to remain in the range between 0.1 and 0.17 which indicates that the flow oscillation is excited by the same mechanism over the whole investigated range of nozzle exit flow velocities and impingement ratios.

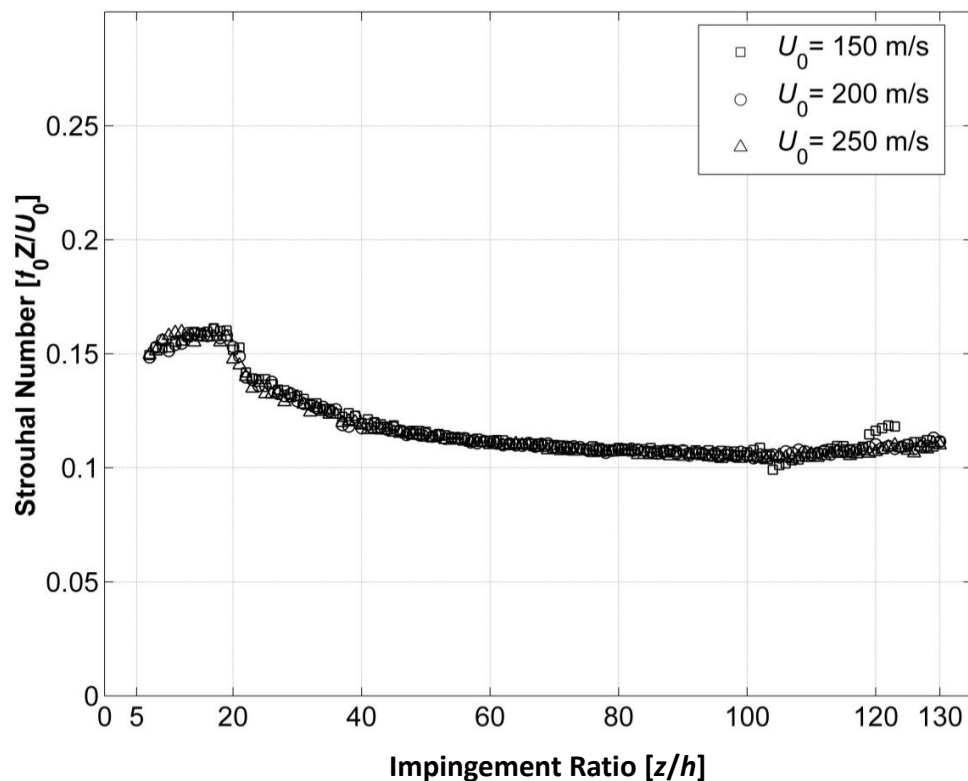


Figure 4-7 Plots for Strouhal number $St_z = f_0 z / U_0$ as a function of impingement Ratio z/h

The variation observed in the Strouhal number versus the impingement ratio is related to the change in the disturbance (instability) convection velocity. At larger separation distances, the potential core is a small fraction of the flow field and the actual convection velocity further downstream becomes smaller than that at the potential core. However, the Strouhal number is based on the nozzle exit velocity which doesn't account for the decrease of the convection velocity for larger impingement distances, and therefore the Strouhal number is relatively smaller at larger impingement ratio.

In brief, experiments showed that for opposing planar jets the acoustic fundamental tone frequency (f_0) varies inversely with the impingement ratio (z/h) at a constant nozzle exit velocity (U_0). The Strouhal number remains at a constant range for a wide range of impingement ratios. The reported frequency behavior outlined in Figure 4-6 confirms speculations of the CFD simulation by Kim et al. (2003) about the change of oscillation frequency of the two jets as nozzle separation distance z increases.

4.1.3 Effect of Nozzle Exit Velocity

This section investigates the effect of changing the nozzle exit velocity (U_0) on the acoustic response of the opposing planar jets. Two sets of experiments were done where the nozzle exit velocity (U_0) was changed at a constant impingement ratio (z/h) in each set. The nozzle exit velocity (U_0) was varied from $U_0=150$ m/s up to 260 m/s by changing the air flow rate in the nozzles. This was done for each set of experiments having a constant impingement ratio of $z/h = 40$ and 50.

In Figure 4-8, a waterfall plot for the acoustic tone spectra of the system is presented. In Figure 4-8 the impingement ratio is kept constant ($z/h = 50$) and the nozzle exit velocity ($150 \leq U_0 \leq 260$) varied. It is observed that the fundamental tone frequency (f_0) and existing harmonic tone (f_1) shifted their location to the right as nozzle exit velocity increases.

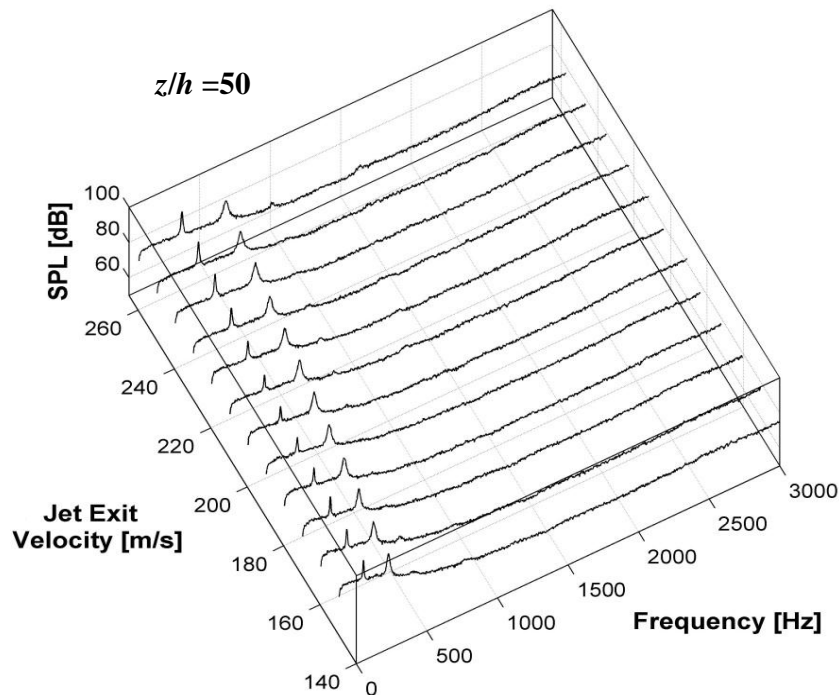


Figure 4-8 Waterfall plots showing acoustic tone response of planar opposed jets for a fixed impingement ratio $z/h = 50$ for a variable nozzle exit velocity $150 \leq U_0 \leq 260$ m/s

Further investigation of the tone frequency behavior is shown in Figure 4-9, where the fundamental tone frequency (f_0) is plotted against the nozzle exit velocity (U_0) for both cases of $z/h = 40$ and 50 . In Figure 4-9, the fundamental tone frequency (f_0) varies

linearly with the nozzle exit flow velocity (U_0) at a constant impingement ratio. This variation is robust over the whole investigated range of velocities, where no frequency jumps or hysteresis effects were observed. This range of velocities was chosen as the system does not produce distinctive tone below $U_0=150$ m/s, while the available air pressure for the system did not allow the exit flow velocity to be increased beyond $U_0=260$ m/s.

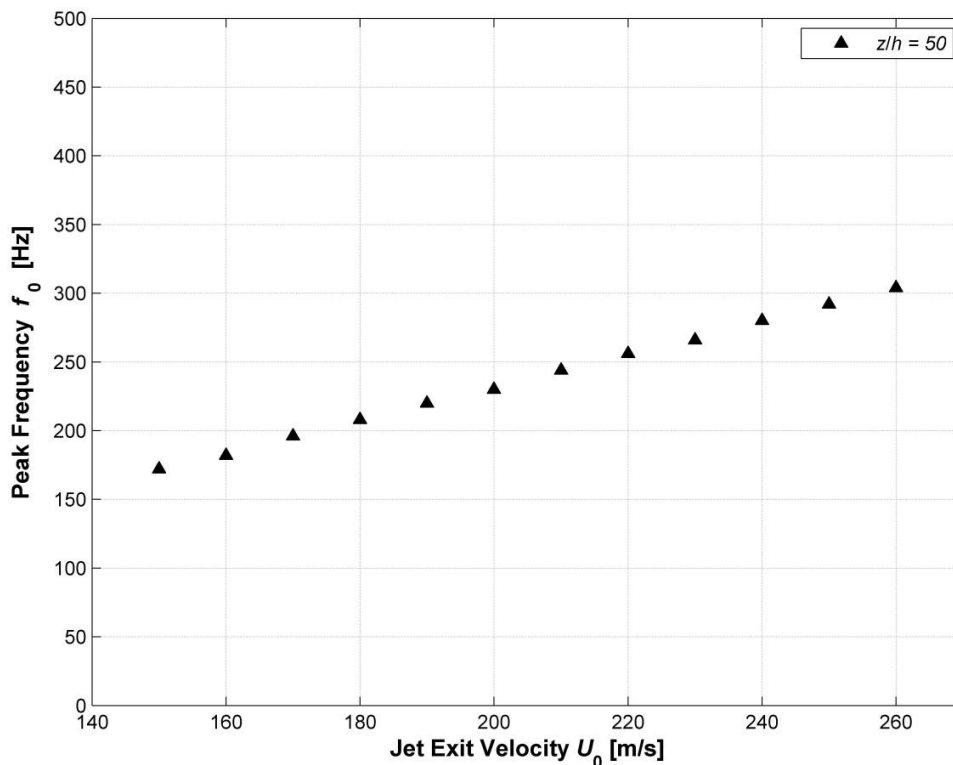


Figure 4-9 Plots for Acoustic Tone Fundamental Frequency f_0 as a function of jet exit velocities U_0 for constant impingement ratio of $z/h = 50$.

When observing the Strouhal number based on impingement distance (St_z) in Figure 4-10, it is found that the Strouhal number remains constant despite changing the nozzle exit velocity (U_0) at a fixed impingement ratio (z/h) which indicates that the frequency of oscillation increases linearly with changes in the nozzle exit velocity, however, it doesn't change the mechanism of oscillation itself. When comparing Strouhal number at a fixed flow velocity, a slight decrease in Strouhal number is observed. This slight decrease matches with the measured data presented in Figure 4-7 for the same range of impingement ratios.

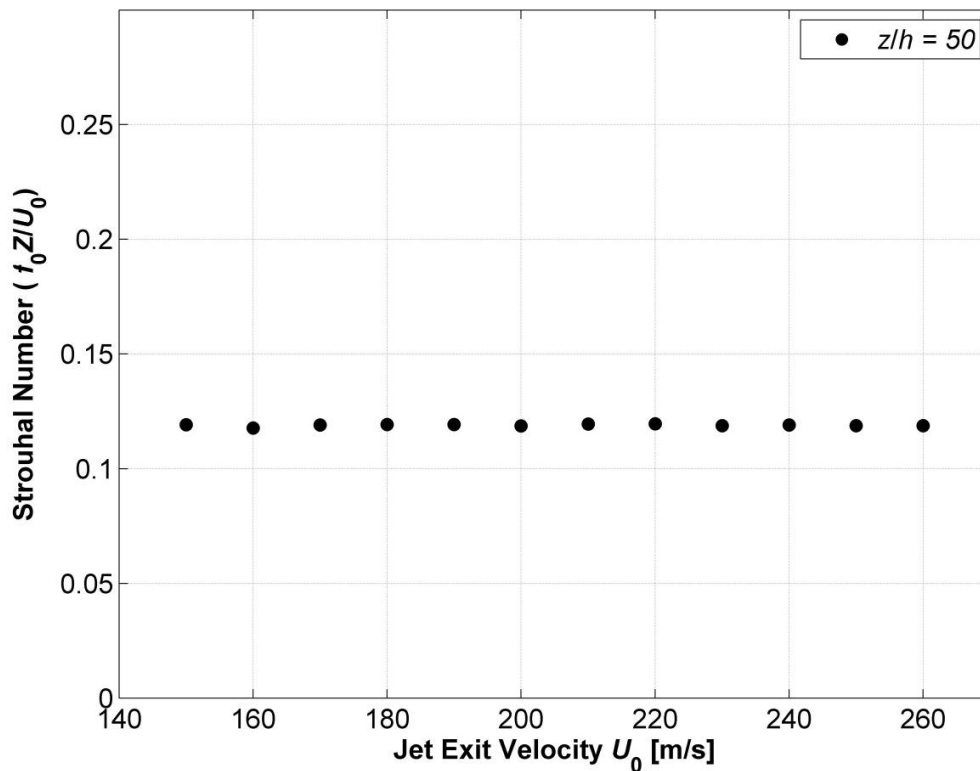


Figure 4-10 Plots for Strouhal number $St_z = f_0 z / U_0$ as a function of jet exit velocities U_0 for constant impingement ratio of $z/h = 50$.

In brief, investigating the effect of nozzle exit velocity on opposing planar jets revealed that the fundamental tone frequency of the system is proportional to the nozzle exit velocity (U_0), while the oscillation mechanism producing that tone remains the same as the exit velocity is varied. Accordingly, this means that when investigating the fluid mechanics of the system one exit velocity would be representative for describing the oscillation mechanism for that system. This oscillation mechanism will be explored in the following section of this chapter. It is worth also to note that up to date there is no available studies in the literature that map the acoustic tone spectra or the frequency exclusively for two planar opposing jet. The closest available study was done by Arthurs (2007) who mapped noise characteristics for gas wiping process. The later mentioned study comprised both planar jet-plate impingement and planar opposing jets in one setup and investigated limited ranges of nozzle separation distance (z) compared to the current study.

4.2 Fluid Dynamic Behavior

4.2.1 Flow field Data Analysis

As mentioned before in Chapter 3, the flow field was acquired by means of a 2-D PIV system. For the current section, the fluid dynamic behavior was investigated for a case where best suitable measurement conditions were available. The best condition for phase locked measurement technique is when the system's tone quality factor (Q) is highest, where a high value of Q indicates strong system oscillation. The tone quality factor is defined by the following relationship:

$$Q = \frac{f_0}{\Delta f} . \quad (4-1)$$

where f_0 [Hz] is the fundamental tone frequency, and $\Delta f = f'_1 - f'_2$ [Hz], where f'_1 and f'_2 are frequencies higher and lower than the peak tone frequency, respectively, at which the acoustic power is halved. A higher tone quality factor means that the system is producing consistent and strong acoustic tone at the selected impingement ratio (z/h) and flow velocity (U_0). Figure 4-11 shows the tone quality factor (Q) versus impingement ratio (z/h) for the chosen exit nozzle velocity $U_0 = 200$ m/s, based on analysis of acoustic tone data in section 4.1 of this study. It is observed that in the range of $40 < z/h < 70$, tone quality factor is highest. Accordingly, the case of $z/h = 50$ and $U_0 = 200$ m/s oscillating at $f_0 = 226$ Hz was chosen for phase-locked PIV measurements. The microphone was

positioned above the top plate of the nozzles, at a 45 degrees angle from the centerline of the two jets and at a distance of 2 inches away from the centerline.

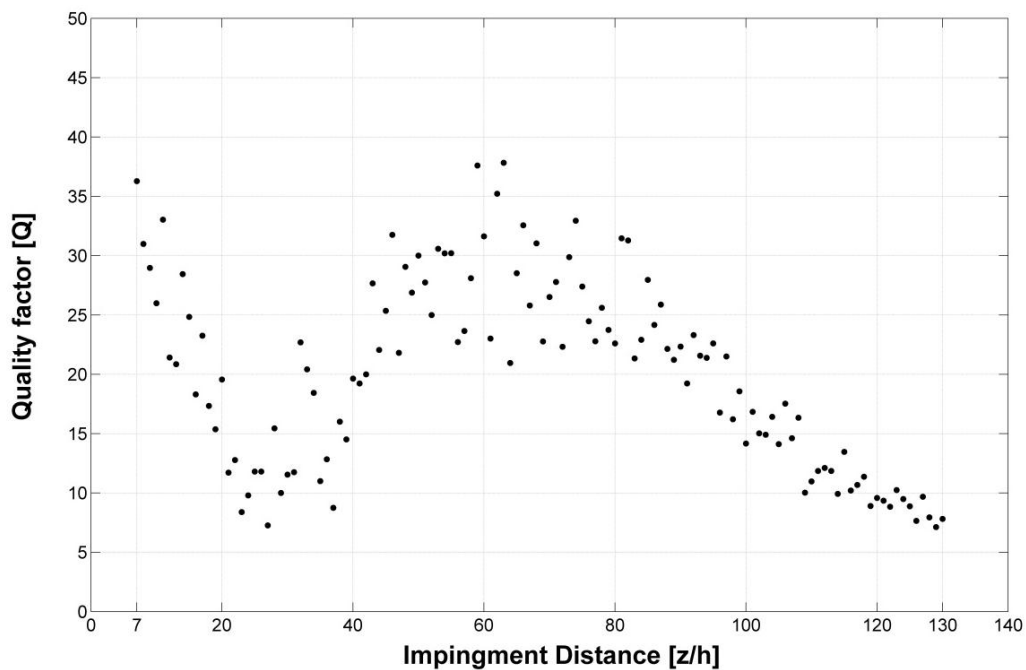


**Figure 4-11 Tone Quality Factor (Q) for various impingement ratio
for $U_0 = 200$ m/s**

It is noteworthy that the tone quality factor (Q) behavior, which is shown in Figure 4-11, has several unique features. There exist two peaks where the first peak appears below the impingement ratio of $z/h = 20$, while the second peak can be observed above $z/h = 50$ in the range of $40 < z/h < 70$. Further research is needed to clarify the reason for this. The other feature is the existence of two regions of low tone quality factors, one starting at $z/h = 22$ and extending up to $z/h = 30$, while the other lie above $z/h = 100$. The large spread in the value of Q is likely caused by the relatively coarse frequency

resolution of the frequency spectra and associated frequency interpolation corresponding to the half power frequencies.

For the PIV data processing, after completing flow field measurements, 800 flow field images were produced, with 100 image per phase which results 8 phases. First, the phase locked images were sorted at each phase, and then phase averaged using a special software provided by TSI[®]. Streamlines for each average phase were plotted using Tecplot[®] software. The velocity components for each phase of the 8 phases was then saved in *.dat file format so it can be imported to Matlab[®] software for further processing. The data is then imported to Matlab[®] in a square matrix format, where a custom code made by the author was used to calculate and plot the following quantities at each measurement point in the flow field: (a) Vorticity fields (b) Velocity vector magnitudes (c) Oscillating stream wise and cross stream components for velocity vector (d) Streamlines.

4.2.2 Flow Field

In the current section we investigate the main flow fields' components with the aim of outlining the oscillation behavior of the system, and laying the foundation for further explanation of the flow oscillation phenomenon. We first examine the velocity magnitude (V_{mag}) which is defined as:

$$V_{\text{mag}} = \sqrt{U(\Phi)^2 + V(\Phi)^2} . \quad (4-2)$$

at each measurement point, where $U(\Phi)$ is the magnitude of flow velocity in stream wise direction Z , and $V(\Phi)$ is the magnitude of flow velocity in the cross stream direction Y for each phase (instant) of the oscillation cycle.

Figure 4-12 shows the velocity magnitude V_{mag} fields for each investigated instant of the oscillation cycle; starting at instant $\Phi=0^\circ$ at the top left of the Figure and moving down through the first column as the phase angle (Φ) increases, and ending the oscillation cycle at instant $\Phi=315^\circ$ at the bottom right of Figure 4-12. The oscillation phenomenon is observed with the increasing phase angles Φ in Figure 4-12. We observe that at instant $\Phi=90^\circ$ of the figure, the bottom jet column is deflected to the left-hand side, whereas the upper jet is deflected to the right. At 180° later, instant $\Phi=270^\circ$, the flow pattern is reversed, where the bottom jet is deflected to the right and the top jet to the left side. In the two top instants $\Phi=0^\circ$ and $\Phi=180^\circ$ also separated by 180° , the two jet columns exhibit the least deflection from their common axis and seem to have the shortest length due to their direct impingement on each other. This motion is described as a *flapping* motion where the two jets deflect away from their common centerline to reach a maximum deflection position then deflect back to their common centerline, then crossing the common centerline to deflect away from it again but on the opposite side. The motion is also described as *anti-symmetric* motion as the two jets move in opposite directions as the oscillation cycle progresses, where mirror like images are observed at each row of instants in Figure 4-12.

The *anti-symmetric flapping* oscillation is the main pattern of flow oscillation for the tested range of impingement length and flow velocity in the current study. This presumption stems from the fact that the oscillation Strouhal number remains virtually constant as indicated in Figure 4-7. In other words, the period (τ) of the shown oscillation cycle is proportional to the impingement ratio, while the deflection of the jets away from the centerline was observed to increase as the impingement ratio is decreased.

The oscillation behavior observed in this study has been reported in the literature, where one of the earliest studies was performed by Denshchikov et al. (1983) who used water jets in a tank. More recently, Wei-Feng et al. (2010) and Wei-Feng et al. (2013) used smoke wire technique to visualize low-speed planar jets and observed similar oscillation. While Kim et al. (2003) performed unsteady flow simulation and also predicted similar oscillation behavior at a frequency comparable to the present measurements in the current study; however, their numerical investigation was enticed to better understand the mechanism of edge over-coating rather than the excitation mechanism of flow-induced noise and vibration.

Second, we investigate the vorticity magnitude (ω_{mag}) which is defined as:

$$\omega_x = \frac{\partial U}{\partial Y} - \frac{\partial V}{\partial Z}. \quad (4-3)$$

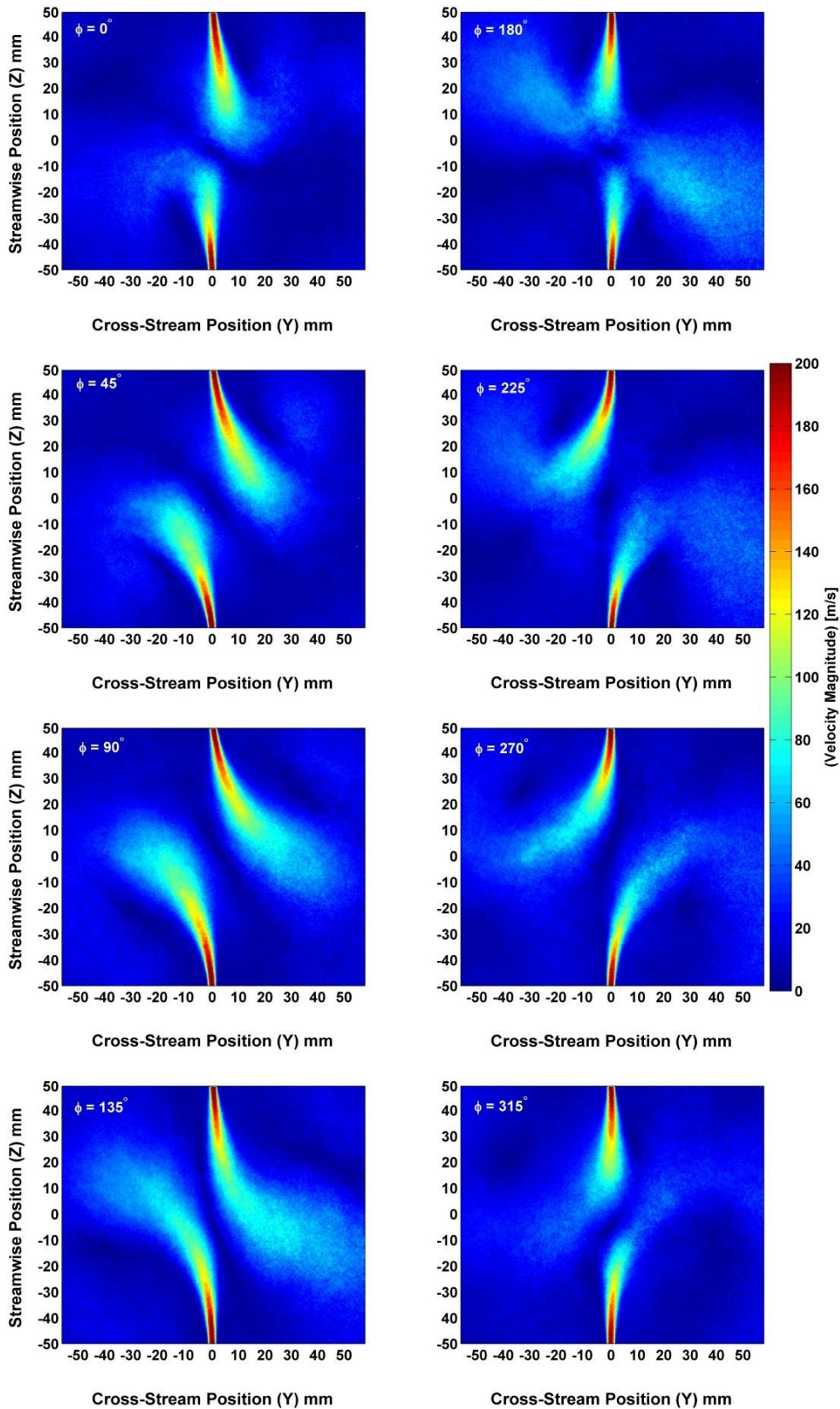


Figure 4-12 Velocity Magnitudes (V_{mag}) at each phase angle (Φ) of the oscillation cycle

at each measurement point , where $\frac{\partial U}{\partial Y}$ is the stream wise shear in Y direction and $\frac{\partial V}{\partial Z}$ is the cross stream shear in Z direction.

Figure 4-13 presents the vorticity magnitude (ω_{mag}) fields over the whole oscillation cycle where each phase angle (Φ) is plotted and positioned similar to Figure 4-12. The vorticity field shows the same oscillation pattern as that of the velocity magnitude. For example, in the instants $\Phi=90^\circ$ & $\Phi=270^\circ$, we observe a “mirror like” like patterns because the flow images are separated by 180° .

On the other hand, several interesting characteristics in the vorticity fields are observed. The upper and lower jets at each field in Figure 4-13 contain regions of high vorticity magnitude existing at the shear layers of the jet (up to 30,000 1/s for the displayed range, where positive vorticity values correspond to anti-clockwise rotation). This high level of vorticity decreases as each jet flow develops downstream. It is surprising that the vorticity field does not show the formation of coherent structure near the impinging jets. In fact, the positive and negative vorticity fields at either side of the jet columns display intense, but small scale vorticity concentrations which seem to break down without agglomerating into large scale vortical structures. This feature is in contrast with other impinging planar jet oscillators flow configurations which develop large scale vortical structures, such as the jet-plate, (Arthurs & Ziada, 2010, 2011, 2012), jet-edge/slot (Ziada, 1995, Staubli & Rockwell, 1987) and mixing layer-edge systems (Ziada & Rockwell, 1982).

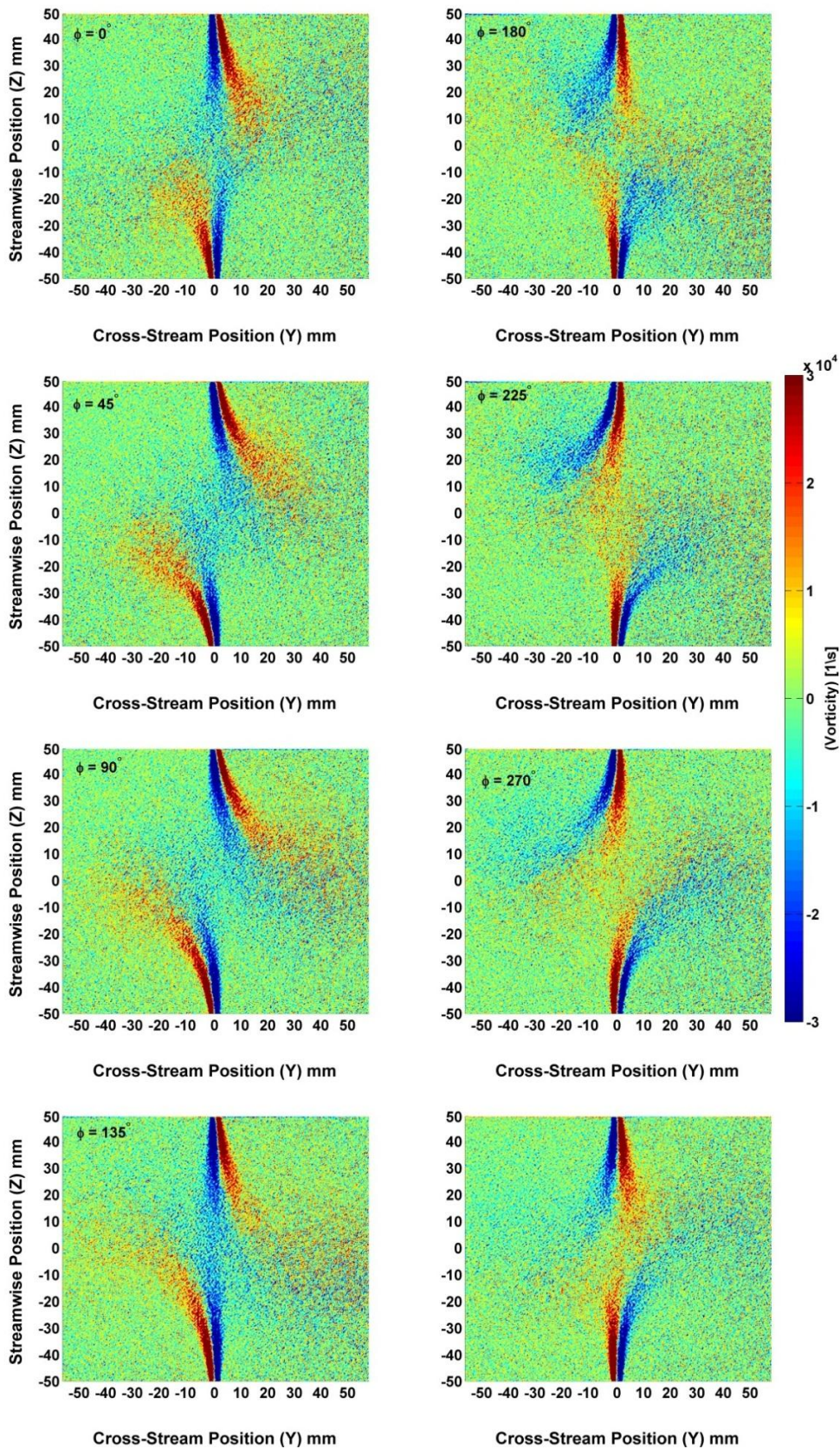


Figure 4-13 Vorticity Magnitudes (ω) at each phase angle (Φ) of the oscillation cycle

However, it is worth to note that the non-dimensional frequency present in the previously mentioned flow configurations is substantially higher than the current study. In the present case, no large scale vortical structures seem to develop. The large vortical structures are absent because the oscillation frequency in the current study lies in a range much lower range than that at which vortical structures usually develop according to linear stability theory (Michalke 1965, 1972, Freymuth, 1966, Husain & Hussain, 1979). Accordingly, the wave length of the flow oscillation, which corresponds to formation length of vortical structures, is substantially higher than the distance at which vortical structures develop and substantially larger than the nozzle separation distance. Thus, large scale vortical structures are not formed.

Third, we investigate the average velocity magnitude and average vorticity magnitude fields which are defined as follow:

$$V_{\text{mag}_{\text{avg}}} = \frac{\sum_{\phi=0^{\circ}}^{\phi=360^{\circ}} V_{\text{mag}}}{n}, \quad (4-4)$$

where, $V_{\text{mag}_{\text{avg}}}$ is the average velocity magnitude over the whole oscillation cycle and V_{mag} is the velocity magnitude at each phase (instant) of the complete oscillation cycle, n is the number of averaged phases ($n=9$). Similarly for the vorticity:

$$\omega_{\text{mag}_{\text{avg}}} = \frac{\sum_{\phi=0^{\circ}}^{\phi=360^{\circ}} \omega_{\text{mag}}}{n}, \quad (4-5)$$

where, $\omega_{mag,avg}$ is the average vorticity magnitude over the whole oscillation cycle and

ω_{mag} is the vorticity magnitude at each phase (instant) of the oscillation cycle.

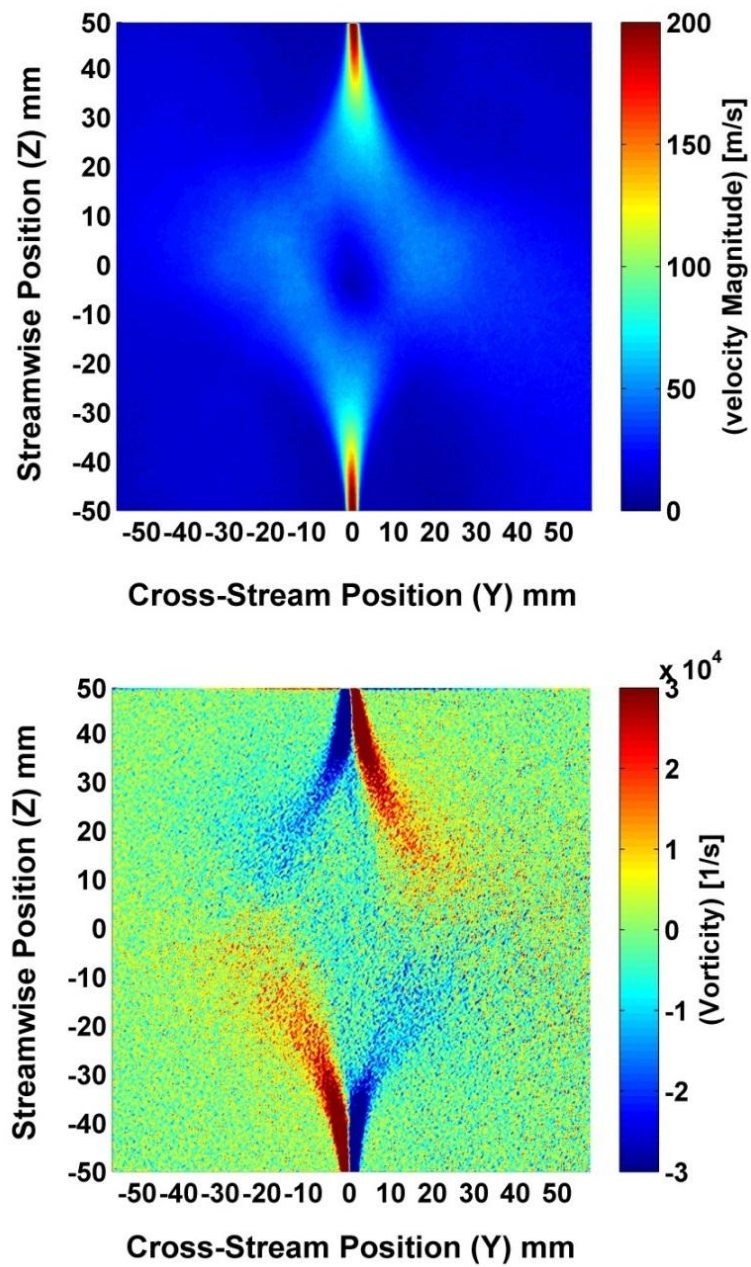


Figure 4-14 Average Velocity and Vorticity Magnitude over a Complete Oscillation Cycle

Figure 4-14 shows the average velocity magnitude (top) and the average vorticity magnitude (bottom) for the complete oscillation cycle, where we observe symmetric pattern on both sides of the common centerline for both average velocity and vorticity fields. The jet spread of the planar jets is enhanced as a result of the opposing jet oscillation compared to jet spread in a free planar jet arrangement (Deo, 2005). Such demonstration of enhancement of jet spread rate has a substantial effect on the rate of mixing which makes this setup efficient in mixing applications.

4.2.3 Oscillation Mechanism

In this section, relevant flow field components are investigated in order to explain the oscillation mechanism. Since the *anti-symmetric flapping* oscillation deflects the flow from its original path along the common centerline of the two jets to the cross stream direction, it is useful to inspect cross stream velocity component ($V(\Phi)$) which is defined as the component flow velocity in the cross stream direction (Y). $V(\Phi)$ may provide an explanation for the flow oscillation behavior.

Figure 4-15 presents the cross stream velocity component ($V(\Phi)$) fields at each phase angle (instant) of the flow oscillation cycle. The velocity $V(\Phi)$ at each measurement point in the flow field is represented by color code where positive (red color) values refer to velocity components moving to the right-hand side (positive Y axis) direction, while the negative (blue color) values refer to velocity components moving to the left-hand side. As the cycle starts, instant $\Phi=0^\circ$, we observe that the upper jet is

moving to the right (red) while the bottom jet is moving to the left at this particular instant. Later at the following instants, $\Phi=45^\circ, 90^\circ$, the upper jet continues to move to the right-hand side and the bottom jet to the left-hand side as seen at each of the instants, respectively. It is also observed that the magnitude of the cross stream component $V(\Phi)$ increases as the flow develops downstream as the jets spread until they impinge on one another. The magnitudes of the cross stream velocity components reach up to 55 m/s, which is about 28 % of the initial exit flow velocity (U_0); indicating that a considerable flow momentum transfers from its original stream wise direction (Z) to the cross stream direction (Y) as the oscillation cycle develops. Later at instant $\Phi=135^\circ$ of Figure 4-15, we observe that the jets start to deflect back to their common centerline, while the magnitude of the cross stream component ($V(\Phi)$) decreases for both the upper jet (red color moving to the right-hand side) and the bottom jet (moving to the left side) at this instant compared with the previous instants $\Phi=45^\circ, 90^\circ$. Afterwards, it is observed that the jet motion is reversed at the next instant $\Phi=180^\circ$, where the upper jet is moving to the left side (blue) while the bottom jet is now moving to the right-hand side (red). Such sequence continues as the flow oscillates, however, the previous observations doesn't explain neither why the jets deflect away from the center nor why they return back to the common centerline and crossing it to the other direction.

Accordingly, further examination was performed of the oscillating cross stream velocity components (V_ϕ') at each instant of the flow oscillation, which is defined as:

$$V_{\phi}' = V(\Phi) - V_{\text{avg}} \quad (4-6)$$

where V_{ϕ}' is the cross stream oscillating velocity magnitude, $V(\Phi)$ is the instantaneous cross stream velocity component at a measurement point at this specific phase (instant) of the oscillation cycle, and V_{avg} is the average of cross stream velocity component over a complete oscillation cycle which is calculated from:

$$V_{\text{avg}} = \frac{\sum_{\phi=0^{\circ}}^{\phi=360^{\circ}} V(\Phi)}{n} \quad (4-7)$$

In Figure 4-16 each phase angle of the oscillation cycle is observed for the oscillating cross stream velocity components (V_{ϕ}'). In the beginning at instant $\Phi=0^{\circ}$ of Figure 4-16, the oscillating velocity V_{ϕ}' at the upper jet is positive (red), i.e. in the right-hand side direction, and the opposite applies for the bottom jet which has V_{ϕ}' components to the left direction. This pattern continues up to instant $\Phi=90^{\circ}$ of Figure 4-16, where at instant $\Phi=135^{\circ}$ of the same figure, the velocity V_{ϕ}' at both sides of the bottom jet column (between $-50 < Y < -10$, $-40 < Z < 0$ and $10 < Y < 50$, $-40 < Z < 0$) have positive values (red) moving to the right-hand side. Similarly, for the instant $\Phi=315^{\circ}$, which displays a mirror like image for previous V_{ϕ}' components explained for instant $\Phi=135^{\circ}$.

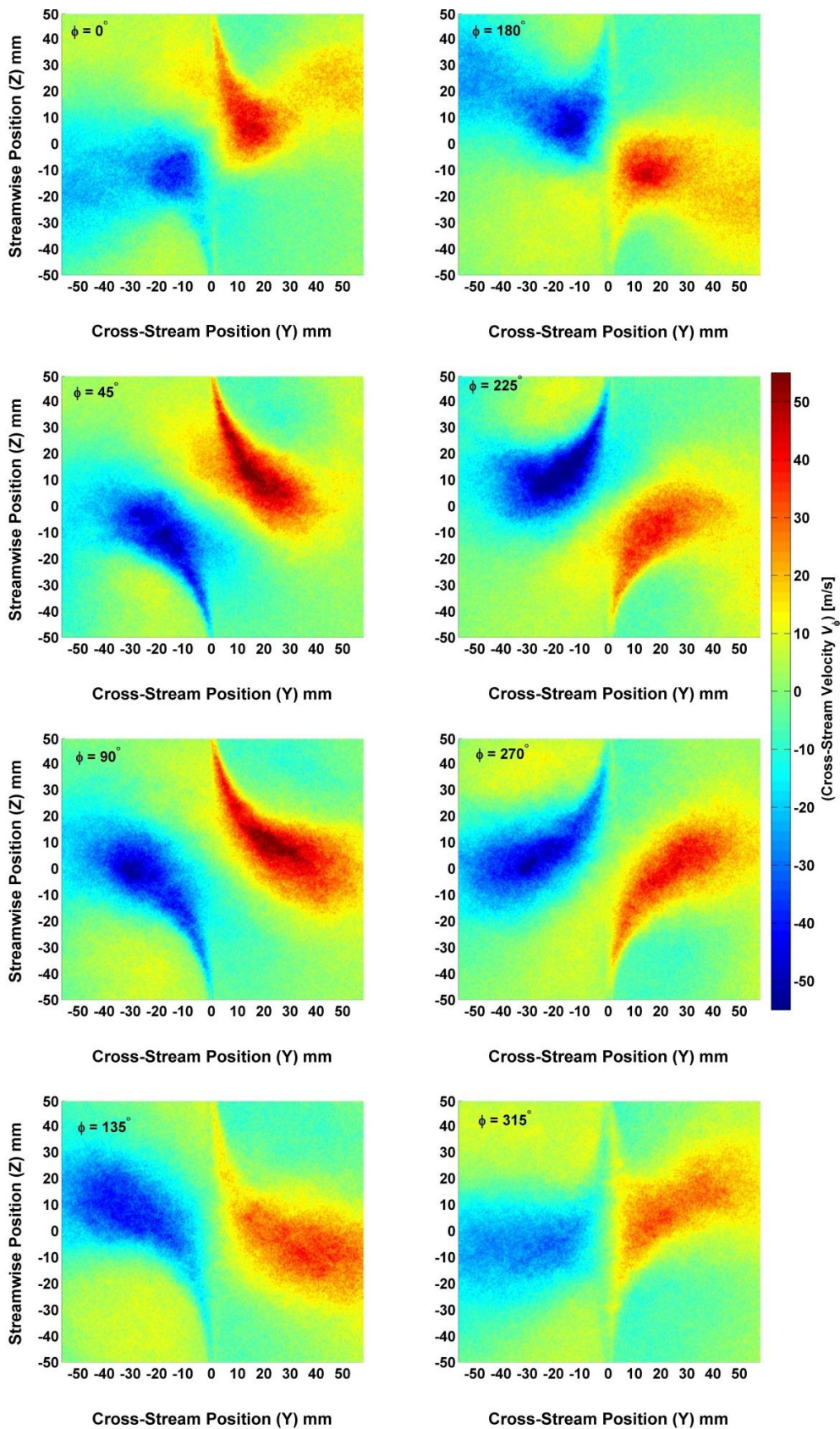


Figure 4-15 Crossstream Velocity Component ($V(\Phi)$) at each phase angle (Φ) of the oscillation cycle

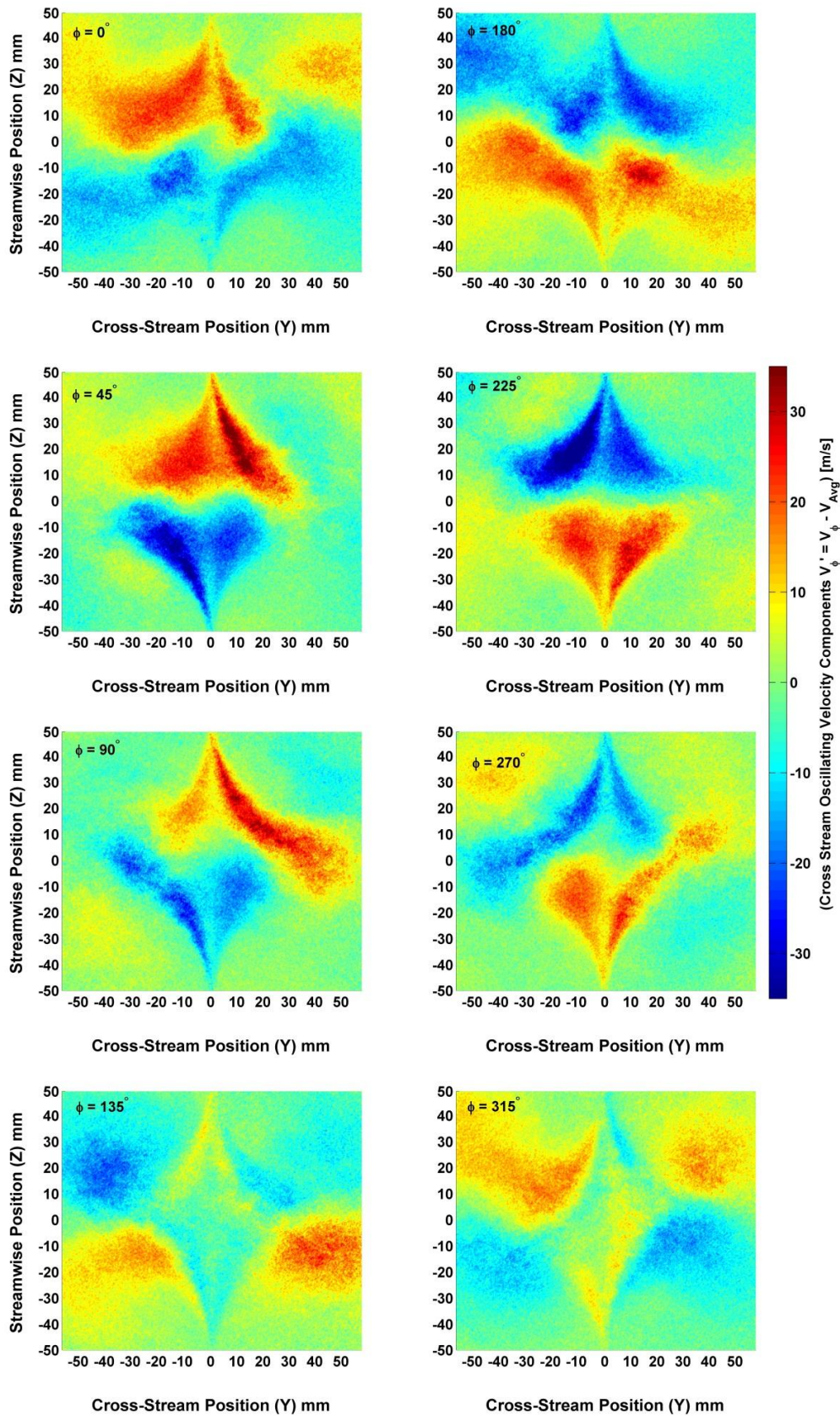


Figure 4-16 Crossstream Oscillating Velocity Component (V'_ϕ) at each phase angle (Φ) of the oscillation cycle

The cross stream oscillating velocity components V_{ϕ}' are believed to assist the jet columns deflection back to their common center. Instants a1 and a3 of Figure 4-17 show velocity magnitudes (at $\Phi=45^{\circ}$ and 225°) of the oscillation cycle, where the jets are deflecting away from their common centerline. This goes along with V_{ϕ}' components observed in instants b1 and b3 respectively of the same figure, where the bottom jet location matches with V_{ϕ}' components pointing towards the left direction in instant b1 and towards the right-hand direction in instant b3. The upper jet location corresponds to V_{ϕ}' components pointing towards the right-hand side direction in instant b1 and towards the left direction in instant b3 of the same figure. Later in the oscillation cycle, the jets are observed to deflect back to the common centerline. This is highlighted by velocity magnitudes represented in instant a2 and a4 of Figure 4-17 (at $\Phi=135^{\circ}$ and 315°), where this coincides to V_{ϕ}' components represented at instants b2 and b4 of Figure 4-17. It is observed that the locations corresponding to the jet sides contain V_{ϕ}' components that induce the jets to deflect back to their common centerline. For example, at instant b2 of Figure 4-17, the flow regions on both sides of the bottom jet contain V_{ϕ}' components pointing towards the right-hand side, forcing it to move to the right-hand direction, while the flow regions on both sides of the upper jet contain V_{ϕ}' components pointing towards the left-hand side forcing it to move to the left direction. As a result, we observe that at instant a3 of Figure 4-17 the jets succeed in deflecting back to their common centerline; crossing it with a high speed due to their inherent inertia, eventually the bottom jet deflects

to the right-hand side and the upper jet deflects to the left-hand side as the oscillation cycle continues.

A noteworthy observation is that the values of V_{ϕ}' displayed in instants b2 and b4 of Figure 4-17 at regions located on the sides of the bottom jet are in range ($10 < V_{\phi}' < 30$), which is higher than the V_{ϕ}' values at locations corresponding to the jet column (which are in range of $V_{\phi}' \approx 10$ m/s). As for the upper jet, the velocity V_{ϕ}' at both sides of the jet column have negative values which are higher values than those at the locations of jet column and thus assisting the upper jet to deflect to the left-hand side. It is obvious from the presented results that the flow behavior at side regions of the jets essentially contributes to the oscillation mechanism, where substantial amount of flow momentum is converted to the cross stream direction due to the impingement of the jets.

Accordingly, a further investigation was performed of jet side regions along with the middle impingement region by examining the flow streamlines at each phase of the oscillation cycle. Figure 4-18 shows the stream lines at each instant of the *anti-symmetric flapping* oscillation where highly organized entrained flow regions are observed at jet sides for all instants of the oscillation cycle.

At instant $\Phi=0^\circ$ of Figure 4-18, two entrained flow regions are observed; one present on the left side of the bottom jet while the other one present on the right side of

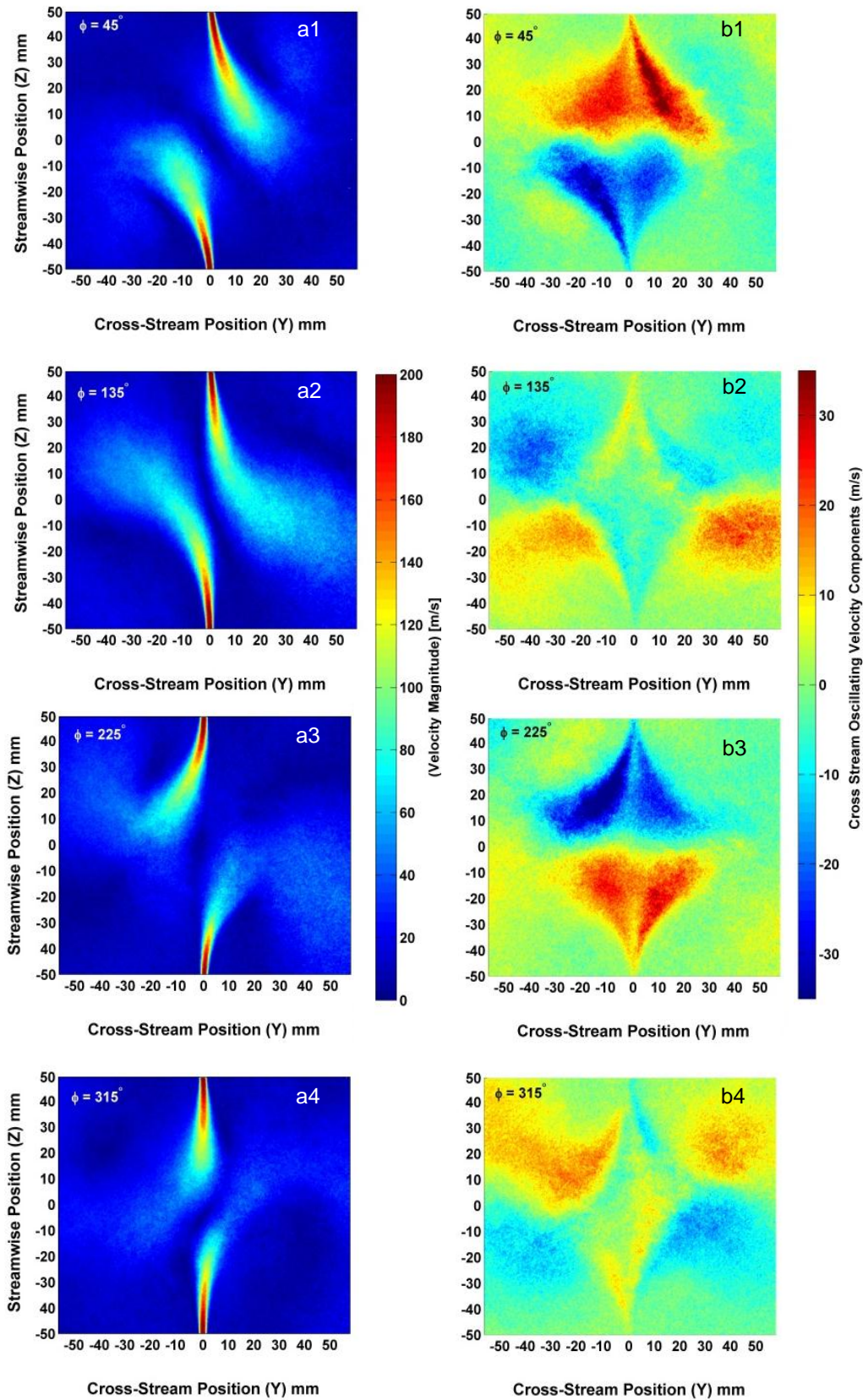


Figure 4-17 Velocity Magnitudes (V_{mag}) and Crossstream Oscillating Velocity Component (V_{ϕ}) at each selected phase angles ($\Phi = 45^\circ, 135^\circ, 225^\circ$ and 315°) of the oscillation cycle

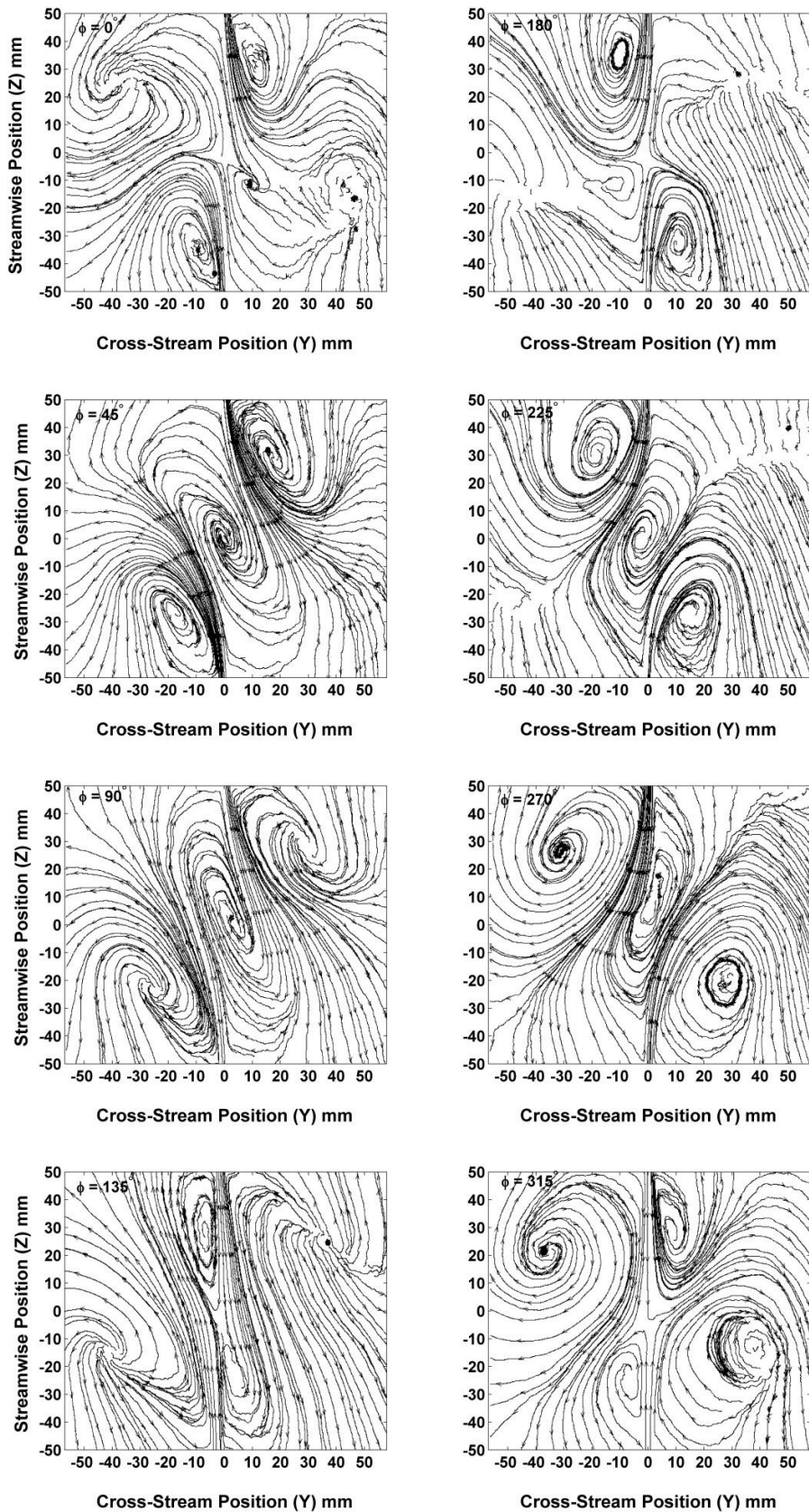


Figure 4-18 Stream lines at each phase angle (Φ) of the oscillation cycle

the upper jet. At instant $\Phi=45^\circ$ a new entrained flow region is observed at the impingement region between the two jets along with the two existing entrained flow regions on the sides of the two jets. Later, at instant $\Phi=90^\circ$, the middle entrained flow region is observed to deform and becomes stretched in stream wise direction (Z). Further at instant $\Phi=135^\circ$, the middle entrained flow continues to stretch in Z direction while the two entrained flow regions at jets sides become weaker. The continuous vertical stretching of the middle entrained flow at instant $\Phi=135^\circ$ splits and forms two new entrained regions which appear at the sides of the two jets at instant $\Phi=180^\circ$. This observation is more clear in instant $\Phi=315^\circ$ of the figure, where the stream wise stretching region between the two jets is seen at instant $\Phi=270^\circ$ to divide into two newly formed entrained flow regions on the right-hand of the upper jet and left-hand side of the bottom jet. The two newly formed entrained flow regions continue to develop in the following instants of the cycle corresponding to phase angles of $\Phi=0^\circ, 45^\circ, 90^\circ$.

The jet side entrained flow regions are believed to largely contribute to the flow oscillation. Those entrained flow regions are observed to continue to grow in size, such as those which start to form at instant $\Phi=0^\circ$ of Figure 4-18 and continue to grow to have maximum size at instant $\Phi=135^\circ$, and those which start to form at instant $\Phi=180^\circ$ and grow in size up to maximum size at instant $\Phi=315^\circ$. While the middle entrainment region starts to become highly organized at instant $\Phi=45^\circ$ and instant $\Phi=225^\circ$, and stretch vertically until it divides into two newly formed entrained flow regions at the jets sides as the oscillation cycle continues. One can see that the jets affect the locations of the middle entrained flow region while they deflect in Y direction away from their common

centerline, this consequently converts considerable part of jet momentum from stream wise (Z direction) to cross stream (Y direction). Furthermore, as the middle entrained flow region stretches in stream wise direction (Z), the jets deflect back to their common centerline where stream wise jet momentum becomes dominant. At this instant, the middle entrainment region becomes divided into two side entrained regions, completing the oscillation cycle.

In order to shed more light on the flow mechanism controlling the flapping jet oscillation, a preliminary numerical simulation was performed to explore the pattern of the pressure fields in a simplified flow setup similar to our study, including similar dimensions and inlet flow conditions. The details of the numerical simulation setup are presented in Appendix I, but the results are briefly presented in the next section.

4.2.4 Computational Fluid Dynamics Flow Simulation

In this section we present results for a simple computational fluid dynamics (CFD) flow simulations that was done to better understand the pattern of the pressure field in the flow. The Ansys CFX Version 14.0 CFD software package was used for the simulation on the current study. The simulation utilized similar geometry parameters as the PIV flow field setup case which had an impingement ratio of $z/h=50$, while the constructed CFD domain had dimensions of 100mm×100 mm (i.e. distance between two nozzle exits $z=100$ mm and cross stream width of 100 mm). The velocity profile at the nozzle exit ($h=2$ mm) was imported from experimental results shown in Figure 3-5 in Chapter 3 where

$U_0 = 200$ m/s. The used working fluid for the simulations was atmospheric air at 25 degree Celsius. The flow was modeled as an unsteady compressible turbulent flow, where the two equation k- ϵ turbulence model was chosen for this simulation. The flow simulation total time was 0.3 seconds with a chosen time step of 1E-6 Sec. A detailed description for the simulation and its chosen parameters can be found in Appendix I. The resulting oscillation had frequency of 229 Hz and the corresponding flow fields were plotted at 8 chosen phases of the oscillation cycle in order to compare simulation flow fields with the experimental results. However, it should be stressed that the simulated flow showed a high degree of transient response and that steady state oscillation was observed only for a few cycles. The frequency of oscillation of those few cycles was 229 Hz compared to $f_0 = 226$ Hz for the experiments. This gives an indication that the current numerical simulation represents the main features of the experimental observations.

Figure 4-19 shows fields of velocity magnitude (V_{mag}); illustrating that the simulated oscillation cycle has similar *anti-symmetric flapping* oscillation which is highlighted in Figure 4-12. The positions of the two jets along the presented oscillation cycle in Figure 4-19 are relatively close to those of experimental results, where at instants $\Phi = 0^\circ$ and $\Phi = 180^\circ$ the two jet columns experience the least deflection from their common centerline as they directly impinged on each other, while mirror-like images are observed for every two flow fields in each row of the same figure.

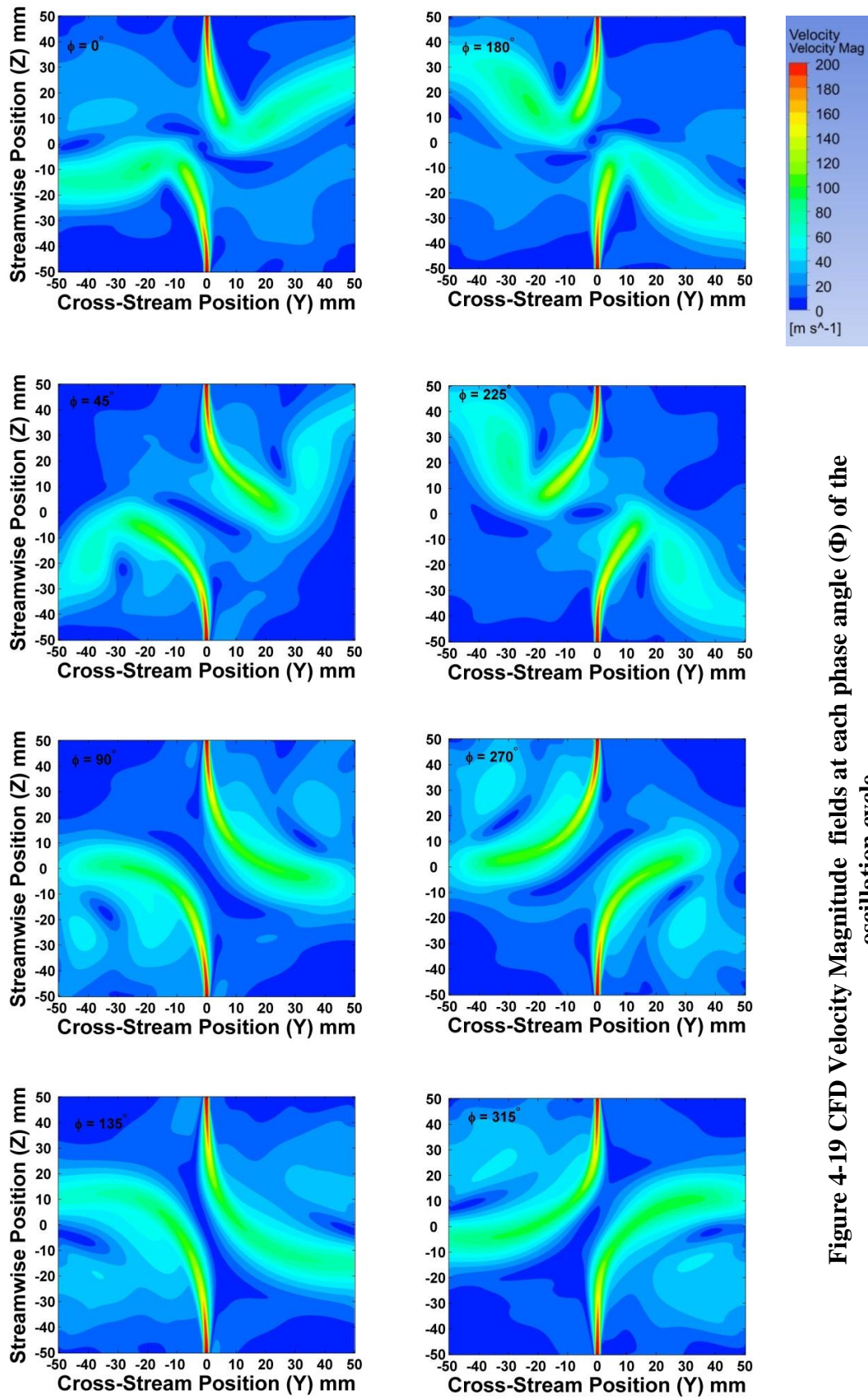


Figure 4-19 CFD Velocity Magnitude fields at each phase angle (Φ) of the oscillation cycle

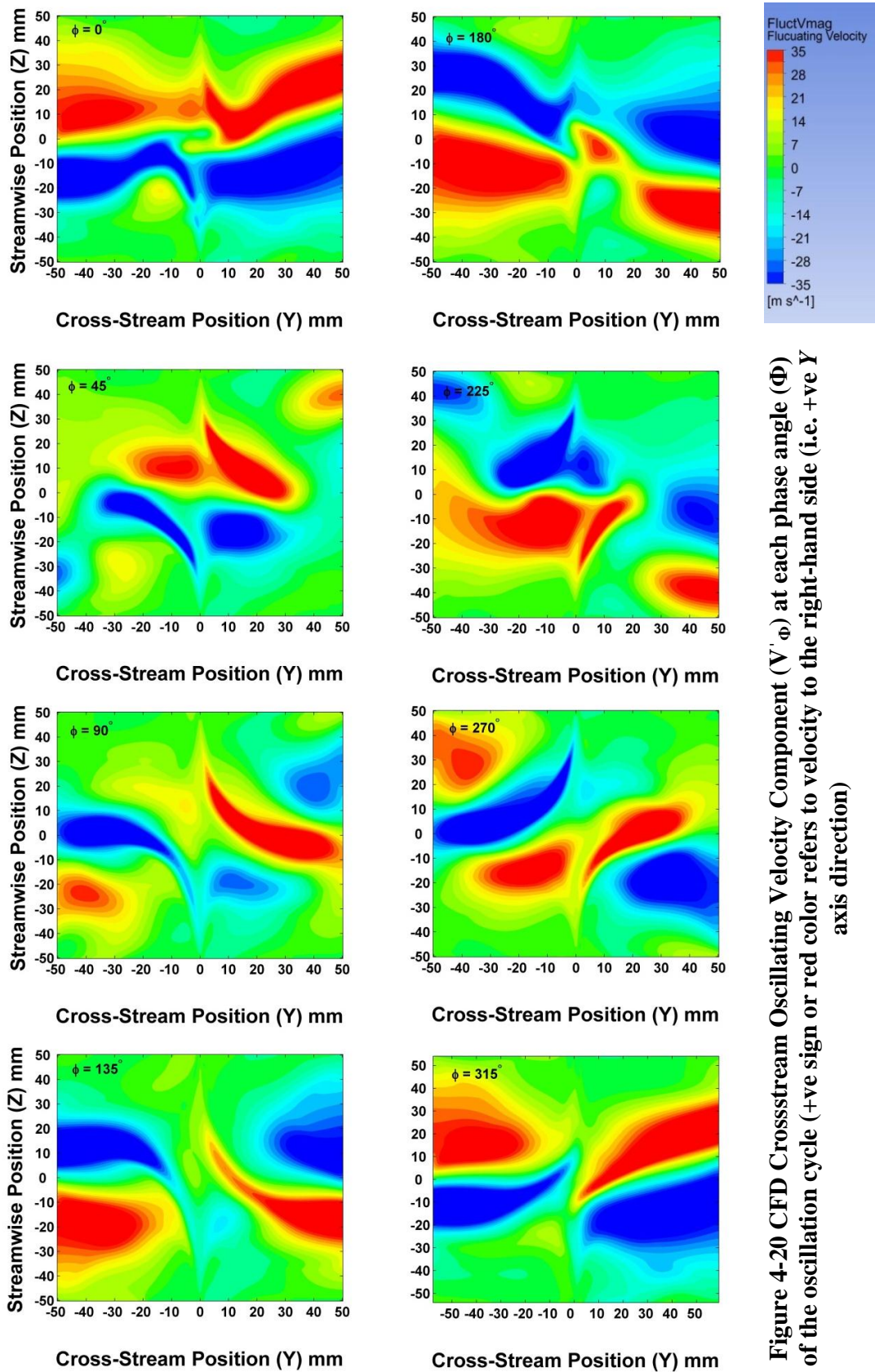


Figure 4-20 CFD Crossstream Oscillating Velocity Component (V'_ϕ) at each phase angle (Φ) of the oscillation cycle (+ve sign or red color refers to velocity to the right-hand side (i.e. +ve Y axis direction))

In Figure 4-20, the oscillating cross-stream velocity components (V_{ϕ}') at each instant of the flow oscillation (which was defined in section 4.2.3) is presented for the CFD simulation. A similar pattern to experimental data shown in Figure 4-16 is observed, where the key instants at $\Phi=135^{\circ}$ and 315° of Figure 4-20 provide an insight how the entrained flow regions at the sides of each jet play a role in the oscillation mechanism. For example, in Figure 4-19 in instant $\Phi=135^{\circ}$ on the left-hand side of the bottom jet an area is observed to have positive V_{ϕ}' which assists the bottom jet to deflect to the right-hand side direction (+ve Y axis) and thereby deflects the bottom jet to the right as can be seen at instant $\Phi=180^{\circ}$. While at instant $\Phi=315^{\circ}$, the right-hand side of the bottom jet shows a negative V_{ϕ}' region that assists the bottom jet to deflect to the left to start a new oscillation cycle at instant $\Phi=0^{\circ}$.

Figure 4-21 shows CFD results of the pressure fields (P_{mag}) along corresponding oscillation cycle resulting from the simulation. At instant $\Phi=0^{\circ}$ the impingement region hosts a relatively high pressure region, while the regions located at upper jet right-hand side and lower jet left side contain lower pressure regions. The high pressure at impingement region assists the jets deflecting away from their common axis once the jets move back to cross their common centerline. For example, instant $\Phi=45^{\circ}$ corresponds to upper jet deflection to the right and lower jet to the left side; where the jets move towards the sides of lower pressure regions.

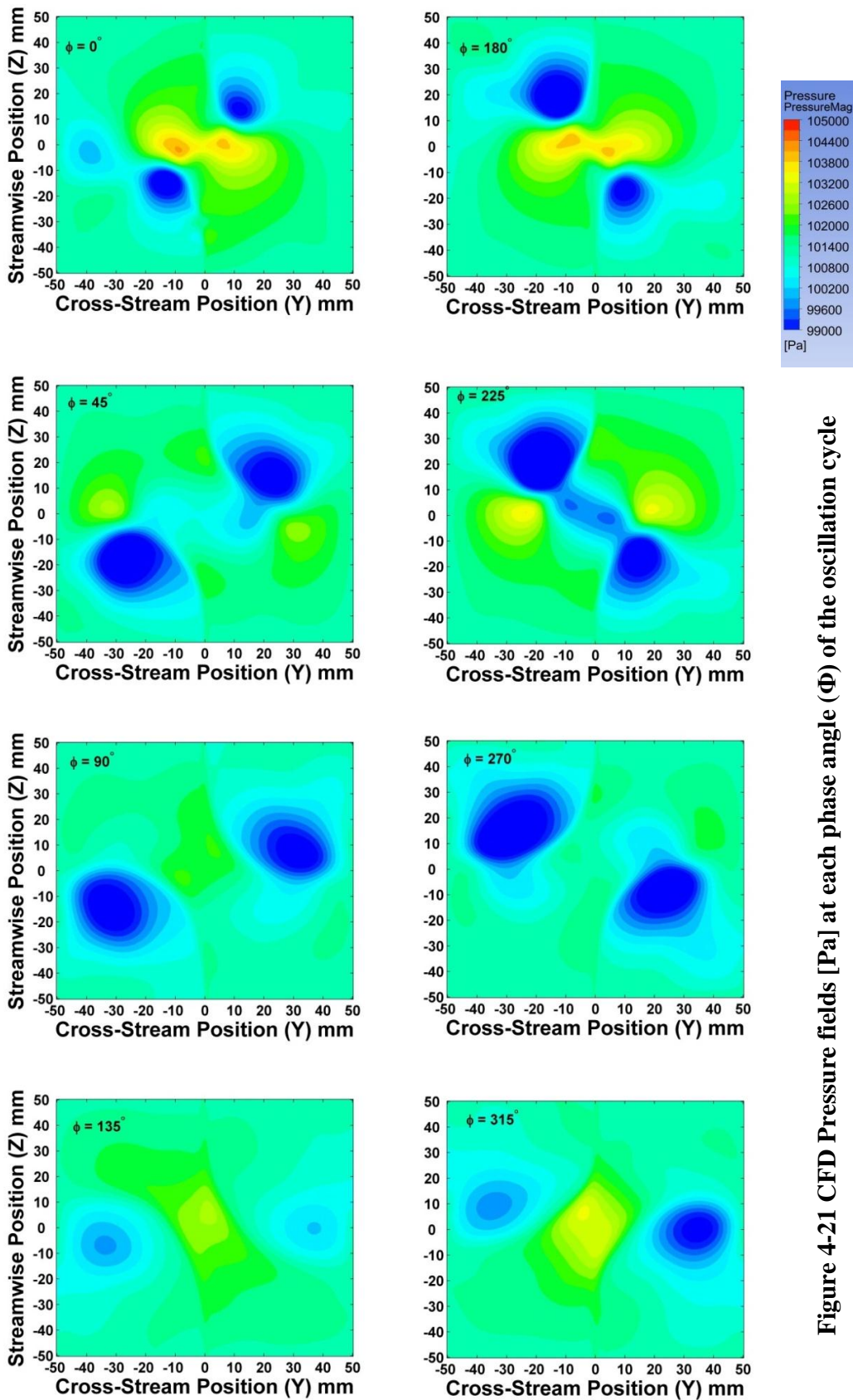


Figure 4-21 CFD Pressure fields [Pa] at each phase angle (Φ) of the oscillation cycle

As the oscillation cycle progresses, namely at instants $\Phi=45^\circ, 90^\circ, 135^\circ$; it is observed that the highest pressure region at impingement divides then fades in the flow field's diagonal direction, however, the middle impingement region remains to have relatively higher pressure. As for the side regions of the two jets, those regions are observed to have distinct low pressure field that grows in size and advect in cross stream direction (Y). Moreover, mirror like images are observed for the pressure fields as the cycle progresses at instants $\Phi=180^\circ, 225^\circ, 270^\circ, 315^\circ$; where the jets continue their flapping oscillation.

In brief, the entrained flow regions in the flow field exhibit oscillating pressure values from high to low pressure, which contribute to both of the oscillation mechanism and the acoustic tone generation which is going to be discussed in the next chapter.

Chapter 5: Discussion and Conclusions

This chapter provides a discussion of the system's fluid dynamic behavior and the flow oscillation frequency in order to explain the flow oscillation mechanism. The chapter also presents an explanation of the tone generation mechanism. Finally, the chapter ends with suggestions for future work on the current topic.

5.1 Flow Oscillation Mechanism

In the previous chapter, flow dynamics of the reported *anti-symmetric flapping* oscillation were explored. Figure 5-1 further presents findings of the current study; it is suggested that the following oscillation mechanism takes place as follows:

- As the two jets directly impinge on each other, they start deflecting away from their common centerline in opposite directions. This deflection is accompanied by conversion of jets flow momentum from stream wise direction Z to cross stream direction Y due to the jet-jet impingement that occur in the middle entrained flow region, while two entrainment regions are formed on sides of the jets as shown in Figure 5-1a. The jets' deflection is believed to be initially assisted by high pressure arising from the impingement at the middle region between the two jets which is demonstrated in Figure 4-20.
- As the two jets further deflect away from the centerline the middle entrained flow region stretches in stream wise direction , where downstream flow momentum

continues to develop, while side entrainment regions at jets sides grow in size as represented in Figure 5-1b (which is a characteristic of single planar free jet flow).

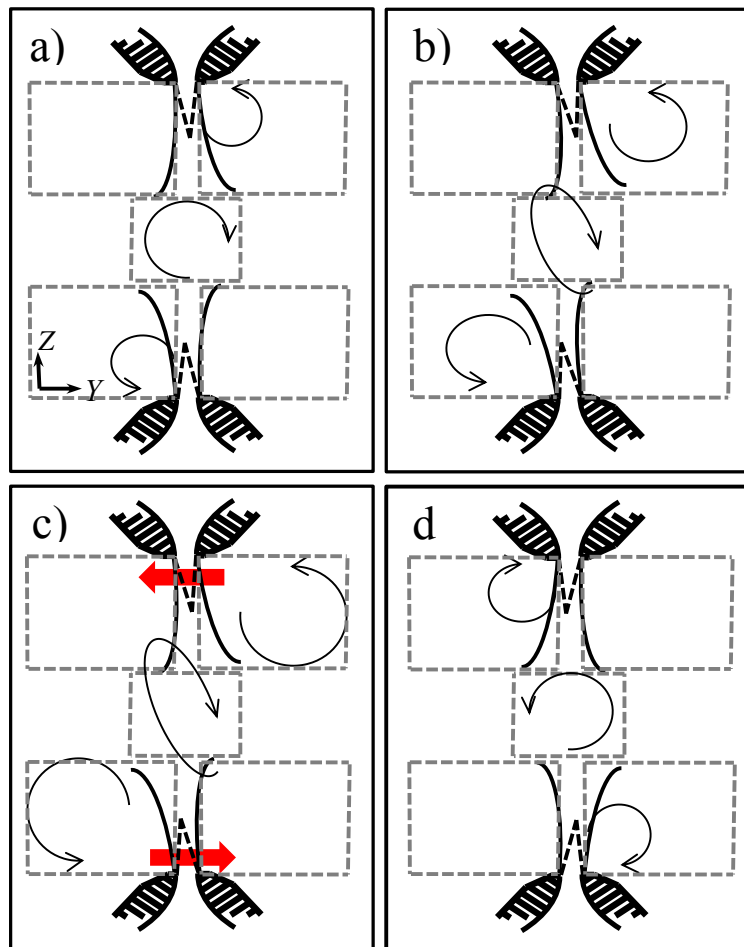


Figure 5-1 Schematic of suggested flow oscillation mechanism

- After the jets reach maximum deflection away from the common centerline, the middle entrained flow region continues to stretch in stream wise direction while the entrained flow regions at the jets' sides continue to grow in size and advect in Y direction. The two jets then start to deflect back towards their common centerline due to oscillating cross stream velocity components at jets' sides that

forces the initial region of the jets back to the common centerline as shown in Figure 5-1c. With this initial deflection, the jets revert back to the common centerline due to their inherent stream wise momentum at their exits.

- As the jets deflect back to their common centerline, they acquire enough momentum to cross the common centerline rapidly and deflect towards the other side as seen in Figure 5-1d.

In the above described oscillation mechanism, it is suggested that the entrained flows located at the jets' sides generate the oscillating cross stream velocity components (V_{ϕ}') which play a fundamental role in sustaining the oscillation mechanism. It seems that the vortex structures do not play a role in the oscillation mechanism. Moreover, it is observed that the oscillation exists in the absence of any confinement around the two jets; this suggests that any vortex structures that might appear in cases of confined setups as reported in previous studies do not play a significant role in the *anti-symmetric flapping* oscillation mechanism of planar opposing jets.

5.2 Flow Oscillation Frequency

The flow oscillation frequency was found to depend on two operation parameters for the investigated constant jet thickness (h). First, the oscillation frequency varies inversely as impingement ratio (z/h) increases. Second, the frequency is directly proportional to the nozzle exit velocity (U_0). The Strouhal number ($St_z = f_0 z / U_0$) remains in

a defined range (0.1 to 0.16) with variation of both impingement ratio (z/h) at a constant exit velocity (U_0) and variation of nozzle exit velocity (U_0) at a constant impingement ratio (z/h). The oscillation frequency (f_0) and Strouhal number (St_z) in the current study are found to be substantially lower than those reported in other types of setups like planar jet-plate, planar jet edge, or mixing-layer edge oscillations. This raises the question about factors controlling the system's oscillation frequency.

According to the available literature, there are two well-known mechanisms that can be responsible for sustaining oscillations of impinging free shear flows. The first mechanism is the jet shear layer instability which has been investigated in detail by Michalke (1965) and many other authors. In this mechanism, the disturbance frequency that receives maximum amplification – thus this frequency prevails in the flow velocity fluctuations - scales with the shear layer momentum thickness, where this thickness corresponds to a point near the center of the linear growth region of disturbances. Examples of this case were reported by Staubli & Rockwell (1987), Ziada (1995), and Ziada (2001) for mixing layer-edge setup and by Ziada (2001) for jet-slot oscillators. This mechanism can occur with no resonance effects, where the small disturbances introduced in the separation region are amplified in the stream wise direction, and eventually impinge on the downstream solid boundary. The impingement distorts the vorticity field downstream, and its effect propagates back upstream to produce new disturbances at the flow separation point; thus the feedback loop of the excitation mechanism is completed. However, in the present case, the frequency estimated from the

linear stability theory for the momentum thickness (θ) near separation is several orders of magnitude higher than the observed flow oscillation frequency, and therefore the oscillation of the opposing planar jets cannot be attributed to instability of the jet shear layers.

The second relevant mechanism is the instability of the planar jet column, where the disturbance frequency receiving maximum amplification depends on the jet thickness and velocity profile at separation. Such mechanism was investigated by Sato (1960), Bajaj & Garg (1977) and Monkewitz & Huerre (1982); while experimental examples of impinging flow oscillations dominated by jet column instabilities can be found in Powell (1961), Ziada (1995), and (Arthurs & Ziada 2012). Typical frequencies associated with this oscillation mechanism (based on jet breadth b) are considerably lower than those associated with the initial shear layer instabilities. According to the available analysis based on the linear stability theory (Sato, 1960, Bajaj & Garg, 1977), the estimated instability frequency of the planar jet column based on the present jet characteristics is considerably higher than the observed frequencies for the current opposing planar jets. Therefore, the oscillation in our study does not seem to be controlled by the jet column instability mechanism either.

It should be also noted that the oscillation period ($\tau_0=1/f_0$) observed in the current study is much larger than the time required for the fluid to travel from the nozzle to the impingement plane between the two jets. In addition, because the oscillation frequency is very low, the wavelength of jet oscillation is much larger than the impingement length.

Thus, the impingement length represents a small fraction of the instability wavelength corresponding to the jet oscillation frequency. This may explain the absence of large scale vortex formation in the oscillating flow field. For the investigated impingement ratios (z/h), the stream wise distance available for jet development is not large enough to allow the formation of vortex structures, as has been explained with the aid of the vorticity field images and streamlines contours shown in Chapter 4.

Furthermore, the described mechanism in the current study suggests that the acoustic modes of the opposed planar jet volume do not play any role in the reported *anti-symmetric flapping* oscillation mechanism either in contrast to confined opposing jet cases like the study by Samaniego et al. (1993) where the authors suggested that the confinement acoustic modes are related to the jets oscillation frequency.

5.3 Acoustic Tone Generation

In this section, a possible mechanism of the acoustic tone generation is highlighted. Since entrained flow regions at jet sides are essentially associated with the flow oscillation, the oscillating pressure fields in those regions, which are described in section 4.2.3, are expected to produce continuous compressions and rarefaction at these locations. Figure 5-2 shows a suggested acoustic tone generation mechanism, where each of the 4 entrainment regions on jet sides experience a maximum pressure (compression) and a minimum pressure (rarefaction) during the *anti-symmetric flapping* oscillation

shown at left and right sides of the figure. The system thus has an acoustic sound source where four adjacent regions of fluctuating pressure field contribute to sound generation.

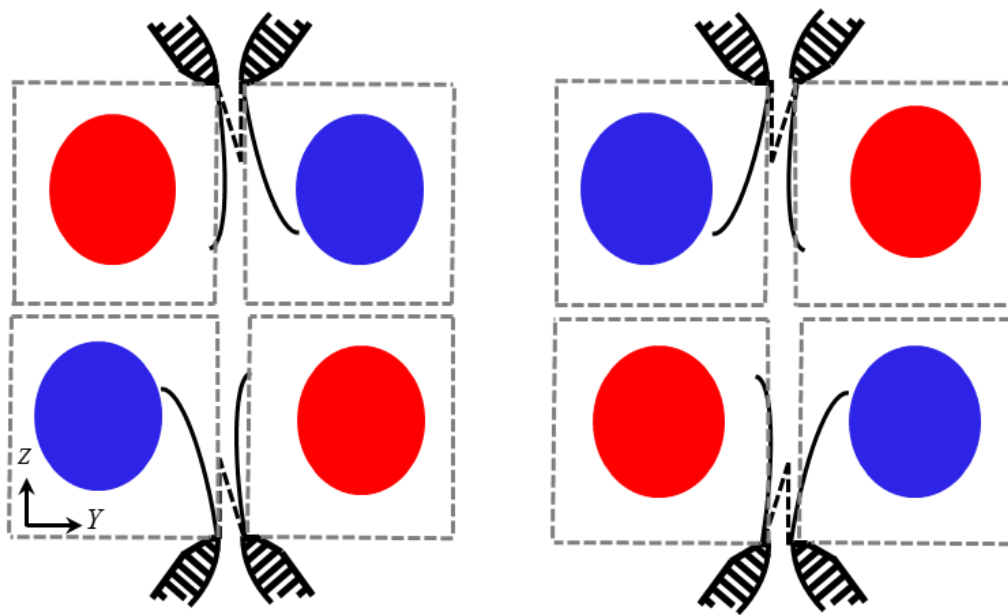


Figure 5-2 Schematic of suggested acoustic tone generation mechanism

5.4 Conclusions

In this study the opposing planar jets were investigated, in which two jets having thickness of $h = 2$ mm were used. The acoustic response for the impingement ratios starting from $z/h = 7$ up to 130 was recorded for different exit nozzle flow velocities of $U_0 = 150, 200$ and 250 m/s. The fluid mechanics of the two interacting opposing jets at $z/h=50$ and $U_0 = 200$ m/s were explored where the jets oscillate on a cycle having a frequency of 226 Hz. Conclusions for the current study are summarized in the following:

1. Acoustic response of the opposing planar jets showed that the opposing jets produce intense acoustic tones at distinct frequencies for the whole tested range of impingement ratios and exit flow velocities. These findings were unique in comparison to any other acoustic response for impinging shear layers in regards to the substantially wider range of impingement ratios at which the tones are generated for the current study. Moreover the system is very robust with no reported frequency jumps or hysteresis effects.

2. The acoustic tone fundamental frequency (f_0) for the opposing planar jets has an inverse hyperbolic trend as the separation distance between the jets increases at a constant nozzle exit flow velocity (U_0) and vice versa. On the other hand, the fundamental frequency (f_0) has a linear proportional trend as the nozzle exit flow velocity (U_0) increases at a constant impingement ratio (z/h).

3. The Strouhal number (St_z) for opposing planar jets remains virtually constant for the investigated jet thickness ($h = 2$ mm), which indicates that the oscillation mechanism for all cases in the current study is the same.

4. The acoustic tone resulted from the current system was found to be produced from *anti-symmetric flapping* oscillation behavior, where the two planar jets deflect away/towards their common center in an oscillatory manner.

5. The reported *anti-symmetric flapping* oscillation behavior is believed to be sustained by the cross stream oscillating velocity components which induce the jets to have its

oscillatory behavior along with the high pressure in the impingement region between the two jets.

6. The acoustic tone generation is suggested to be resulting from an oscillating pressure fields associated with the opposing planar jet oscillations.

5.4 Suggestions for Future Work

The current setup has promising applications in fields of combustion and chemical industry, below are some suggestions for future work that will help further study current setup's behavior:

- Experimental investigation of pressure fields at various locations of the flow field.
- Investigating the effect of entrainment by adding solid boundaries in cross stream direction of the flow field.
- Examining the effect of acoustic excitation on the system at different operating conditions.
- Investigating the acoustic tone source of the system also at various operating conditions.

Bibliography

- Arthurs, D. (2007). *Noise Generation in the Gas Wiping Process*. Hamilton, Ontario, Canada: McMaster University.
- Arthurs, D. (2012). Self-Excited Oscillations of the Impinging Planar Jet. *Open Access Dissertations and Theses. Paper 7380.*, 250-253.
- Arthurs, D., & Ziada, S. (2010). Self-Sustained Oscillations of High Speed Impinging Planar Jets. *ASME 2010 7th International Symposium on Fluid-Structure Interactions, Flow-Sound Interactions, and Flow-Induced Vibration and Noise: Volume 3, Parts A and B. 3*, pp. 703-712. Quebec: ASME.
- Arthurs, D., & Ziada, S. (2011). The planar jet-plate oscillator. *Journal of Fluids and Structures*, 27, 105–120.
- Arthurs, D., & Ziada, S. (2012). Self-excited oscillations of a high-speed impinging planar jet. *Journal of Fluids and Structures*, 34, 236-258.
- Arthurs, D., Ziada, S., & Goodwin, F. (2008). Noise Generated by Wiping Air Knives in Hot-Dip Galvanizing. *100th Galvanizers Association Meeting, Baltimore, Maryland*.

Bajaj, A., & Garg, V. (1977). Linear stability of jet flows. *Journal of Applied Mechanics*, 44, 378-384.

Berman, Y., Tanklevsky, A., Oren, Y., & Tamir, A. (2000). Modeling and experimental studies of SO₂ absorption in coaxial cylinders with impinging streams. Part I. *Chem Eng Sci.*, 55, 1009–1021.

Berman, Y., Tanklevsky, A., Oren, Y., & Tamir, A. (2000). Modeling and experimental studies of SO₂ absorption in coaxial cylinders with impinging streams. Part II. *Chem Eng Sci.*, 55, 1022–1032.

Coleman, H., & Steele, W. (1999). *Experimentation and Uncertainty Analysis for Engineers* (2nd Edition. ed.). Wiley-Interscience.

Denshchikov, V., Kondrat'ev, V., & Ramshov, A. (1983). Auto-oscillations of planer colliding jets. *Translated from Izvestya Akademii Nuak SSSR, Mekhanika Zhidkosti I Gaza*, 3, 148-150 UDC 532.522.2.

Denshchikov, V., Kondrat'ev, V., & Ramshov, A. (1978). Interaction between two opposed jets. *Translated from Izvestya Akademii Nuak SSSR, Mekhanika Zhidkosti I Gaza.*, 6, 165-167 UDC 532.522.

- Deo, R. C. (2005). Experimental Investigations on the Influence of Reynolds Numbers and Boundary Conditions on a Plane Air Jet. *PhD Thesis*. The University of Adelaide, Australia. .
- Fleming, A., Penesis, I., Macfarlane, G., Bose, N., & Hunter, S. (2012, March). Phase averaging of velocity fields in an oscillating water column using splines. *Proceedings of the Institution of Mechanical Engineers, Part M: Journal of Engineering for the Maritime Environment*.
- Freythuth, P. (1966). On transition in a separated laminar boundary layer. *Journal of Fluid Mechanics*, 25, 683–704.
- Gavi, E., Marchisio, D., & Barresi, A. (2007). CFD modelling and scale-up of confined impinging jet reactors. *Chem Eng Sci.*, 62, 2228–2241.
- Husain, Z., & Hussain, A. (1979, January). Axisymmetric Mixing Layer: Influence of the Initial and Boundary Conditions. *AIAA Journal*, 17(1), 48-55.
- Johnson, D., & Wood, P. (2000). Self-sustainable oscillations in opposed impinging jets in an enclosure. *Can J Chem Eng.*, 78, 867–875.
- Johnson, B., & Prud'homme, R. (2003). Chemical processing and micromixing in confined impinging jets. *AIChE J.*, 49, 2264–2282.

- Kim , S., Cho, J., Ahn, K., & Chung, M. (2003). Numerical Analysis of Edge Overcoating in Continuous Hot-dip Galvanizing. *ISIJ Int (Iron Steel Inst Jpn)*, 43(10), 1495-1501.
- Kim, K., Lee, M., Yoon, S., Boo, J., & Chun, H. (2002, March). Phase averaged velocity field in the near wake of a square cylinder obtained by a PIV method. *Journal of Visualization*, 5(1), 29-36.
- Liu, Y., & Fox, R. (2006). CFD predictions for chemical processing in a confined impinging-jets reactor. *AIChE J.*, 52, 731–744.
- Liu, Y., & Fox, R. (2006). CFD predictions for chemical processing in a confined impinging-jets reactor. *AIChE J.*, 52, 731–744.
- Mahajan, A., & Kirwan, D. (1996). Micromixing effects in a two-impinging-jets precipitator. *AIChE Journal*, 42, 1801-1814. .
- Mi, J., Deo, R., & Nathan, G. (2005). Characterization of turbulent jets from high-aspect-ratio rectangular nozzles. *Phys. Fluids*, 068102 (4 pages).
- Michalke, A. (1965). On spatially growing disturbances in an inviscid shear layer. *Journal of Fluid Mechanics*, 23, 521–544.

Michalke, A. (1972). The instability of free shear layers. *Progress in Aerospace Sciences*, 12, 213-216.

Monkewitz, P., & Huerre, P. (1982). The influence of the velocity ratio on the spatial instability of mixing layers. *Phys. Fluids*, 25, 137-43.

Nosseir, N., & Behar, S. (1986). Characteristics of Jet impingement in a side dump combustor. *AIAA Journal*, 24(11), 1752-1757.

Nosseir, N., Peled, U., & Hildebrand, G. (1987, Oct.). Pressure field generated by jet-on-jet impingement. *AIAA Journal*, 25, 1312-1317.

OCCUPATIONAL HEALTH AND SAFETY ACT. (2006, December 19). *ONTARIO REGULATION 565/06*. Retrieved April 8, 2013, from <http://www.e-laws.gov.on.ca/>: http://www.e-laws.gov.on.ca/html/source/regs/english/2006/elaws_src_regs_R06565_e.htm

Pope, S. (2000). *Turbulent Flows* (1st ed.). Cambridge University Press.

Powell, A. (1961). On the Edgetone. *Journal of the Acoustical Society of America*, 33, 395–409.

Powell, A. (1988). The sound-producing oscillations of round underexpanded jets impinging on normal plates. *Journal of Acoustical Society of America*, 55.

- Raffel, M., Willert, C., Wereley, S., & Kompenhans, J. (2007). *Particle image velocimetry: a practical guide*. (2nd edition. ed.). Springer Publishing, Berlin.
- Rayleigh, L. (1880). On the stability or instability of certain fluid motions. *Proceedings of the London Mathematical Society.*, 11, 57–70.
- Rockwell, D., & Naudascher, E. (1979). Self-sustained oscillations of impinging free shear layers. *Annual Review of Fluid Mechanics.*, 11, 67–94.
- Samaniego, J., YIP, B., Poinsett, T., & Candel, S. (1993). Low-Frequency Combustion Instability Mechanisms in a Side-Dump Combustor. *Combustion and flame*, 94, 363-380.
- Santos , R., Erkoç, E., Dias, M., Teixeira, A., & Lopes, J. (2008). Hydrodynamics of the mixing chamber in RIM: PIV flow-field characterization. *AIChE J.*, 54, 1153–1163.
- Santos, R., Erkoç, E., Dias, M., & Lopes, J. (2009). Dynamic behavior of the flow field in a RIM machine mixing chamber. *AIChE J.*, 55, 1338–1351.
- Sato, H. (1960). The stability and transition of a two-dimensional jet. *Journal of Fluid Mechanics*, 7, 53-80.

- Scarano, F., & Riethmuller, M. (2000). Advances in iterative multigrid PIV image processing. *Experiments in Fluids.*, 29, 51–60.
- Shi, Y., Fox, R., & Somashekar, V. (2011). Visualization of turbulent reactive mixing in a planar microscale confined impinging-jet reactor. *Journal of Micromechanics and Microengineering*, 22(11).
- Staubli, T., & Rockwell, D. (1987). Interaction of an unstable planar jet with an oscillating leading-edge. *J. Fluid Mech.*, 176, 135-167.
- Teixeira, A., Santos, R., Costa, M., & Lopes, J. (2005). Hydrodynamics of the mixing head in RIM: LDA flow-field characterization. *AIChE J.*, 51, 1608–1619.
- Tesař, V. (2002, September). Microfluidic Turn-down Valve. *Journal of Visualization*, 5(3), 301-307.
- Tesař, V. (2009, December). Oscillator micromixer. *Chem Eng J.*, 155(3), 789-799.
- Viskanta, R. (1993). Heat transfer to impinging isothermal gas and flame jets. *Experimental Thermal and Fluid Science.* , 6, 111–134.
- Wei-Feng, L., Guo-Feng, H., Gong-Yi, T., Hai-Feng, L., & Fu-Chen, W. (2013). Experimental study of planar opposed jets with acoustic excitation. *Phys. Fluids*, 25, 014108.

- Wei-Feng, L., Tian-Liang, Y., Hai-Fen, L., & Fu-Chen, W. (2010). Experimental investigation of flow regimes of axisymmetric and planar opposed jets. *AIChE J.*, *57*, 1434–1445.
- Wood, P., Hrymak, A., Yeo, R., Johnson, D., & Tyagi, A. (1991). Experimental and computational studies of the fluid mechanics in an opposed jet mixing head. *Phys Fluids A*, *3*, 1362–1368.
- Wu, Y., Li, Q., & Li, F. (2007). Desulfurization in the gas-continuous impinging stream gas-liquid reactor. *Chem Eng Sci.*, *62*, 1814–1824.
- Yu, Z. (2007). Development and demonstration plant operation of an opposed multi-burner coal-water slurry gasification technology. *Front Energy Power Eng China.*, *1*, 251–258.
- Ziada, S. (1995). Feedback control of globally unstable flows: impinging shear flows. *Journal of Fluids and Structures*, *9*, 907–923.
- Ziada, S. (2001). Interaction of a jet-slot oscillator with a deep cavity resonator and its control. *Journal of Fluids and Structures*, *15*, 831–843.
- Ziada, S., & Rockwell, D. (1982). Vortex-leading edge interaction. *J. Fluid Mech.*, *118*, 79–107.

Appendix I: CFD Simulation Details

In this section, details are provided on the computational fluid mechanics simulation that was used to describe the pressure field for the corresponding investigated experimental conditions of $z/h = 50$ and $U_0 = 200$ m/s.

Software

Ansys Workbench was used to generate the simulation domain and for meshing that domain. While solution was done by CFX Version 14.0, displaying the results and plotting flow fields was done using CFD post provided by Ansys. A Windows 7 based PC was used for this simulation.

Domain Geometry

The domain of the current simulation was constructed having geometry similar to that of the PIV experimental setup, where the simulated nozzle thickness is $h = 2$ mm, while the spacing between the two nozzles is 100 mm ($z/h = 50$), and cross stream width of 100 mm. Figure I-1a shows a schematic drawing for the used domain geometry where the domain is constructed by drawing a plane which contains two inlet nozzle, then extruding that plane to chosen thickness. The extruded domain was modeled as 3 bodies connected with default fluid-fluid interface that provides conservative interface flux for momentum and turbulence. The thickness of the domain was chosen to be 0.8 mm which

gives an aspect ratio of relative to the nozzle thickness of $h/0.8=2.5$, moreover a thickness of 0.8 mm is larger than the turbulent energy containing eddies provided that the turbulent integral length scale has same magnitude of the nozzle thickness. (Pope, 2000)

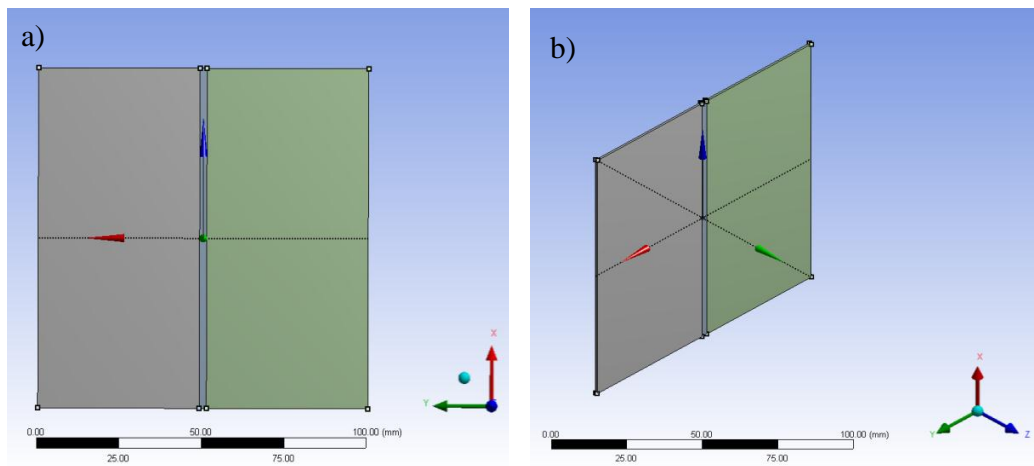


Figure I-1 Schematic of the Simulation Domain Geometry

Mesh

A rectangular grid was used in meshing the simulation domain where the grid size varies along the domain, and one mesh element was used in the domain extrusion direction. Figure I-2 shows the meshed simulation domain which is relatively fine near to the nozzle exit and coarser in the stream wise and cross stream direction. This mesh has fine meshed areas near to the nozzle exit where initial shear layers interact with the atmosphere. Table I-1 presents the mesh properties; the mesh contained 105040 nodes

and 51657 elements. This choice of mesh size is discussed in the following sections of this appendix.

Property	value
Min Size	0.2 mm
Max face Size	1 mm
Growth rate	1.1
Minimum edge length	0.8 mm
Nozzle Sizing	0.2 mm
Cross stream initial Edge Size	0.4 mm
Stream wise initial edge size	0.5 mm
Cross stream/Stream wise edge bias factor	3
Number of solution nodes	105040
Number of solution elements	51657

Table I-1 Mesh Properties for CFD Simulation

Flow Setup and Boundary Conditions

The used working fluid for this simulation was chosen to be atmospheric air at 25 degrees Celsius, the buoyancy effects where neglected.

The used turbulence model was k- ϵ (Jones & Launder, 1972), as it provides a good start for a solution for many types of jet flows. Using k- ϵ model also resulted in stable solution within a reasonable amount of total simulation time.

As for the domain boundary conditions Figure I-3 shows the meshed domain with corresponding boundary conditions. First, the domain edges in the cross stream direction

were modeled as openings boundary condition which is defined as a boundary that allows the flow in and out across the surface (pressure outside the domain is taken to be atmospheric pressure). The surfaces in the span wise direction of the nozzles were modeled as symmetry boundary condition, which accounts for the high aspect ratio of the nozzle and the two dimensionality behavior. The boundary condition at the nozzles was modeled as an inlet boundary condition where the initial velocity profile at the nozzle exit was generated based on the experimental velocity profile data outlined in Chapter 3

The simulation was run for a total simulated time of 0.3 second with time step of $1E-6$ in order to get a stable flapping oscillation at frequency of 229 Hz where the choice of time step is discussed in the last section of this appendix.

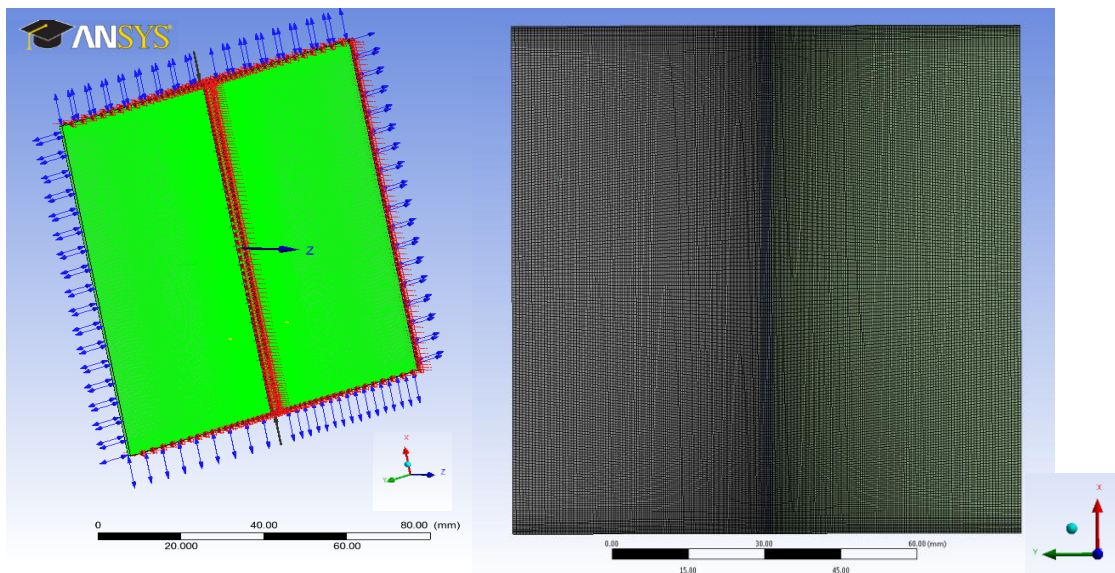


Figure I-3 Meshed domain (right) and corresponding Boundary conditions (left) for CFD simulation

Grid Dependence

In this section, brief results are presented for grid independence study which was done before running the simulation to choose the proper grid for the study. The used time step for the grid dependence for is $1\text{E-}6$ seconds. Three different grids were used in the current studies, which will be referred to as grid A, B and C. where A being coarsest grid (double element size of B) and C being the finest grid (Half element size of B).

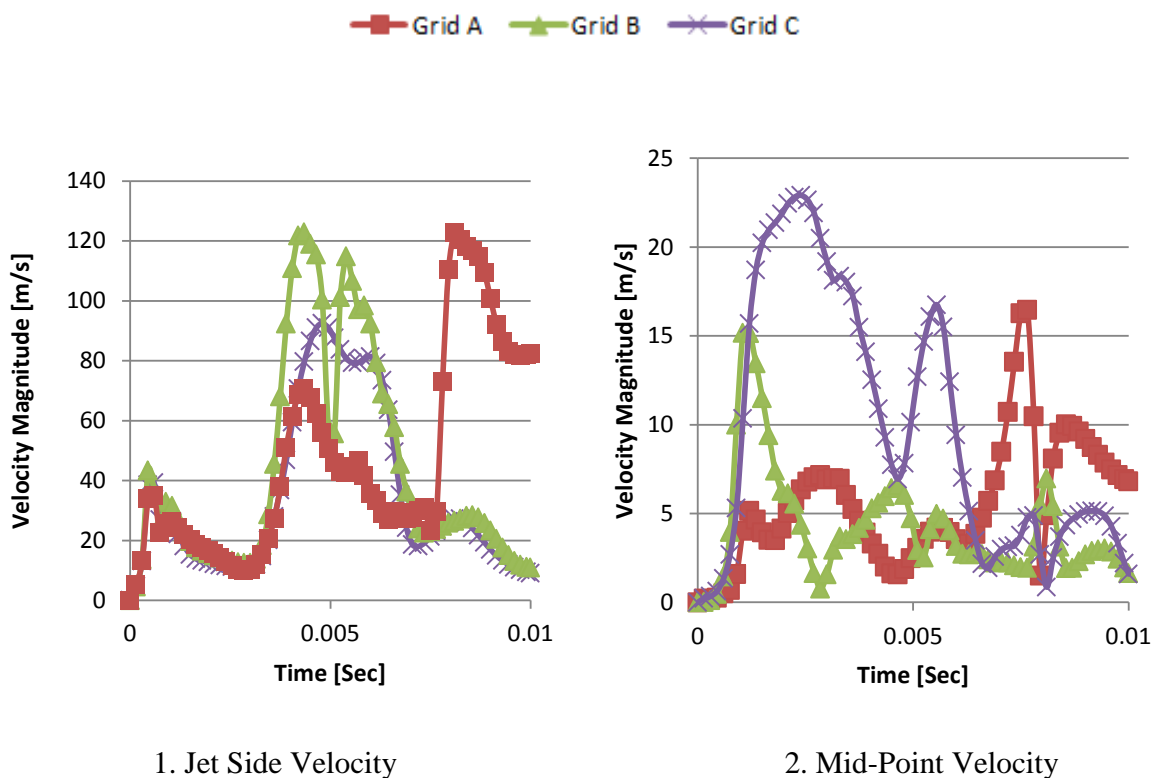


Figure I-5 Results of Grid Dependence Study

Four different monitors were used to investigate the grid dependence of the simulation. The first two monitors are values of velocities at two fixed points in the domain over a time period of 0.01 second, one of the two fixed points was the midpoint between the two jets while the other fixed point lies 25 mm downstream and 10 mm cross stream of the nozzle center. The second two monitors are the velocity profiles along both the common centerline of the two jets and at the middle plane between the two jets.

Figure I-4 presents the 4 monitors for grid dependence for the 3 used grids. It is observed that changes in the 4 monitors is very small (<5%) beyond Grid B, accordingly grid B was chosen to be the working grid for the current simulation.

Time Step Dependence

In this section we present brief results for the time step independence study that was done before choosing the simulation time step. The same monitors used for the grid dependence study are used in the time step dependence study. Three time steps were used which are going to be referred to as time step A = $2e-6$ second, time step B = $1e-6$ second, and time step C = $0.5e-6$ second.

Figure I-5 shows comparisons of the 4 monitors for different time steps, we observe that the difference between B and C is relatively small, accordingly, time step B was used in the current simulation.

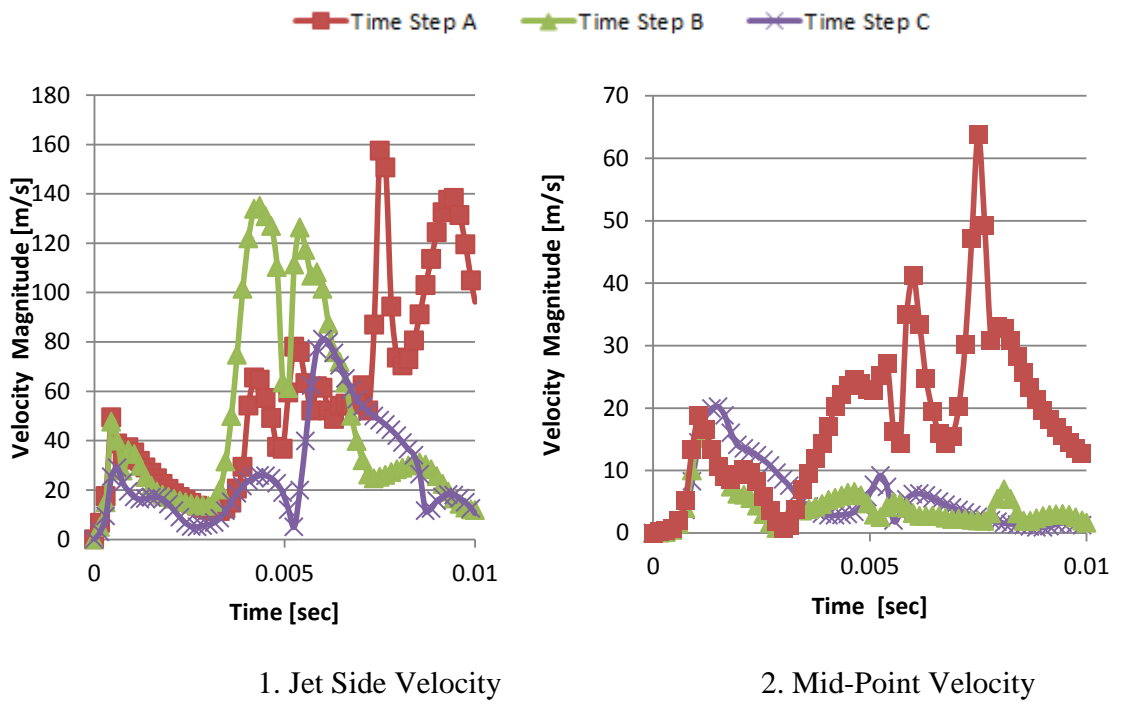


Figure I-5 Results of time independence study

Appendix II: Uncertainty and Error Analysis

In this section, the uncertainty associated with the measured experimental data is presented. According to Coleman & Steele (1999), for a variable (R) which is represented by independent measurement variables (v_i) as follows:

$$R = f(v_1, v_2, v_3, v_4, \dots, v_i). \quad (\text{II-1})$$

the uncertainty in variable (R) can be calculated using the Kline and McClintock method using the following relationship:

$$\partial R = \sqrt{\sum_{i=1}^N \left(\frac{\partial R}{\partial v_i} \partial v_i \right)^2}. \quad (\text{II-2})$$

where ∂v_i is the measurement uncertainty for an independent measurement variable v_i , and ∂R is the overall uncertainty of the dependent variable.

AII-1 Uncertainty Analysis for Geometry Parameters of Experiments

For the current study, geometrical parameters were measured directly with tools of known error range, thus we could report the uncertainty of geometrical parameters directly. The set up was leveled using standard level and aligned using rotary stages and transverse vice at each set of measurements to ensure preciseness and production of

repeatable results. Jet width (h) was measured using high precision filler gauges, while the impingement distance (z) was initially measured by the same filler gauges used for jet width measurement at an initial distance $z=h$ and then distance was adjusted by the electronic controlled vice model VXM-3. The microphone location was adjusted using a digital precision Vanier. Table II-1 presents results of uncertainty in measurements of geometry parameters in the current setup.

The impingement distance (z) is dependent on the following: the rotary stages resolution ($\partial\theta = 0.008^\circ$), the cross stream direction (Y) vice resolution ($\partial Y = 0.01\text{mm}$); and the stream wise direction (Z) measurement resolution (maximum uncertainty is for used filler gauge so $\partial Z = 0.01\text{mm}$). Accordingly, the following uncertainty relationship applies for the impingement distance:

$$\partial z = \sqrt{2\left(\frac{\partial z}{\partial \theta} \partial \theta\right)^2 + \left(\frac{\partial z}{\partial Y} \partial Y\right)^2 + \left(\frac{\partial z}{\partial Z} \partial Z\right)^2}. \quad (\text{II-3})$$

where $\frac{\partial z}{\partial \theta}$ is change in impingement distance corresponding to change in rotary stage inclination (two rotary stages exist) which is estimated to be $3.1675\text{E-}4$, while $\frac{\partial z}{\partial Y}$ is change in impingement distance corresponding to cross stream vice offset which is estimated to be $1.92\text{E-}5$, finally $\frac{\partial z}{\partial Z}$ is change in impingement distance corresponding to change in stream wise distance (estimated to be 1). Using Equation (II-3) $\partial z = 0.01\text{ mm}$

Geometry Parameter	Measurement Uncertainty
Jet Width (h)	$\pm 0.01\text{mm}$
Impingement distance (z)	$\pm 0.01\text{mm}$
Microphone location	$\pm 0.01\text{mm}$

Table II-1 Uncertainty Analysis for Experiments Acoustic Response Parameters

Frequency and Sound Pressure Level

For the acoustic response, the frequency spectra was established by breaking down the acoustic tone time signal 100 blocks equal in size, the data was acquired at a sampling rate of 51.2 kHz for 50 seconds, producing a spectral resolution of 2 Hz, where slight changes in fundamental tone frequency (f_0) was observed during the process of averaging. The uncertainty in the frequency is estimated to be at maximum of the spectral resolution of the acoustic tone $\partial f = \pm 2$ Hz. While the microphone has a flat frequency response in range of 4 Hz-70 kHz with uncertainty in SPL of $\partial SPL = \pm 2\text{dB}$.

Nozzle plenum static pressure P and exit nozzle velocity U_0

The acoustics measurements were acquired based on operation variables; one of those is the nozzle exit flow velocity U_0 which was calculated from the nozzle plenum static pressure (P). A Validyne[®] DP-15 pressure transducer was used having a full scale accuracy of $\pm 2.5\%$ fitted with an 8.0 psi diaphragm, thus uncertainty for nozzle plenum static pressure is estimated to be pressure $\partial P = \pm 0.02$ psi (± 0.00137 bar). Over the operation range, the plenum pressure experienced slight variations less than 2 % of the recorded readings.

The exit nozzle velocity (U_0) was thus calculated from the following relationship derived from compressible flow through an isentropic nozzle:

$$U_0 = c \sqrt{\frac{2}{\gamma - 1} \left[\left(\frac{P + P_\infty}{P_\infty} \right)^{\frac{\gamma - 1}{\gamma}} - 1 \right]}. \quad (\text{II-4})$$

where c is the speed of sound which can be expressed as $c = \sqrt{\gamma RT}$ where $R = 287.04$ J/(kg·K) is the ideal gas constant for air and T is air temperature in kelvin. Air can be assumed as an ideal gas having ratio of specific heat of $\gamma = 1.4$, thus, substituting by c into equation (II-4) the exit nozzle velocity U_0 can be written as:

$$U_0 = \sqrt{\frac{2\gamma RT}{\gamma - 1} \left[\left(\frac{P + P_\infty}{P_\infty} \right)^{\frac{\gamma - 1}{\gamma}} - 1 \right]}. \quad (\text{II-5})$$

Looking into equation (II-5), there can be three parameters that affect uncertainty of U_0 , namely: ambient air temperature (T), b) ambient air pressure (P_∞), and the nozzle plenum static pressure (P). By expanding (II-5) using Kline and McClintock method and the mentioned uncertainty parameters, and following similar procedure done by (Arthurs 2012) for the same nozzle it results the following relationship:

$$\partial U_0 = \sqrt{\left(\frac{\partial U_0}{\partial T} \partial T \right)^2 + \left(\frac{\partial U_0}{\partial P_\infty} \partial P_\infty \right)^2 + \left(\frac{\partial U_0}{\partial P} \partial P \right)^2}. \quad (\text{II-6})$$

which by differentiation ultimately leads to the following:

$$\partial U_0 = U_0 \sqrt{\left(\frac{1}{2T} \partial T \right)^2 + \left(\frac{\left(\frac{(\gamma - 1)P}{2\gamma P_\infty^2} \right)}{\left[\left(\frac{P + P_\infty}{P_\infty} \right) - \left(\frac{P + P_\infty}{P_\infty} \right)^{\frac{-1}{\gamma}} \right]} \partial P_\infty \right)^2 + \left(\frac{\left(\frac{(\gamma - 1)}{2\gamma P_\infty^2} \right)}{\left[\left(\frac{P + P_\infty}{P_\infty} \right) - \left(\frac{P + P_\infty}{P_\infty} \right)^{\frac{-1}{\gamma}} \right]} \partial P \right)^2}. \quad (\text{II-7})$$

The ambient air temperature was measured by a digital thermocouple that has a resolution of 0.1 K where a variation of maximum 2 K during the experiment operation, thus a total of uncertainty for temperature of $\partial T = \pm 2.1\text{k}$, whereas for nozzle static pressure P , the uncertainty is due to the pressure transducer $\partial P = \pm 0.00137$ bar, and for the ambient pressure an uncertainty is estimated to be $\partial P_\infty = \pm 0.001$ bar for the testing

time as measured by a digital barometer. During the experiments, the static pressure in the plenum varied between 0.2 and 0.55 bar. Substituting previous values in equation (II-7) the maximum uncertainty in U_0 is calculated to be $\partial U_0 \approx 0.8$ m/s for $U_0 = 250$ m/s , and relative uncertainty $\frac{\partial U_0}{U_0} = 0.355$ %

Strouhal number

The calculated Strouhal number ($St_z = \frac{f_0 z}{U_0}$) depends on tone fundamental frequency (f_0), the impingement distance (z) and exit nozzle velocity (U_0). Following the same uncertainty calculation method results the following uncertainty for Strouhal number (St_z):

$$\partial St_z = \sqrt{\left(\frac{\partial St_z}{\partial f_0} \partial f_0\right)^2 + \left(\frac{\partial St_z}{\partial z} \partial z\right)^2 + \left(\frac{\partial St_z}{\partial U_0} \partial U_0\right)^2}. \quad (\text{II-8})$$

which after expansion reduces to the following relationship:

$$\partial St_z = \sqrt{\left(\frac{z}{U_0} \partial f_0\right)^2 + \left(\frac{f_0}{U_0} \partial z\right)^2 + \left(\frac{-f_0 z}{U_0^2} \partial U_0\right)^2}. \quad (\text{II-9})$$

Using the above equation for all the investigated experimental data we found that the maximum uncertainty for Strouhal number (St_z) to be $\partial St_z = 0.00348$ which was about 3

% for that specific measurement point where $U_0=150$ m/s and $z=0.26$ m. Figure II-1 shows sample Strouhal number (St_z) plot with corresponding uncertainty error bars for $U_0=150$ m/s and a variable impingement ratio (z/h) calculated from equation (II-9).

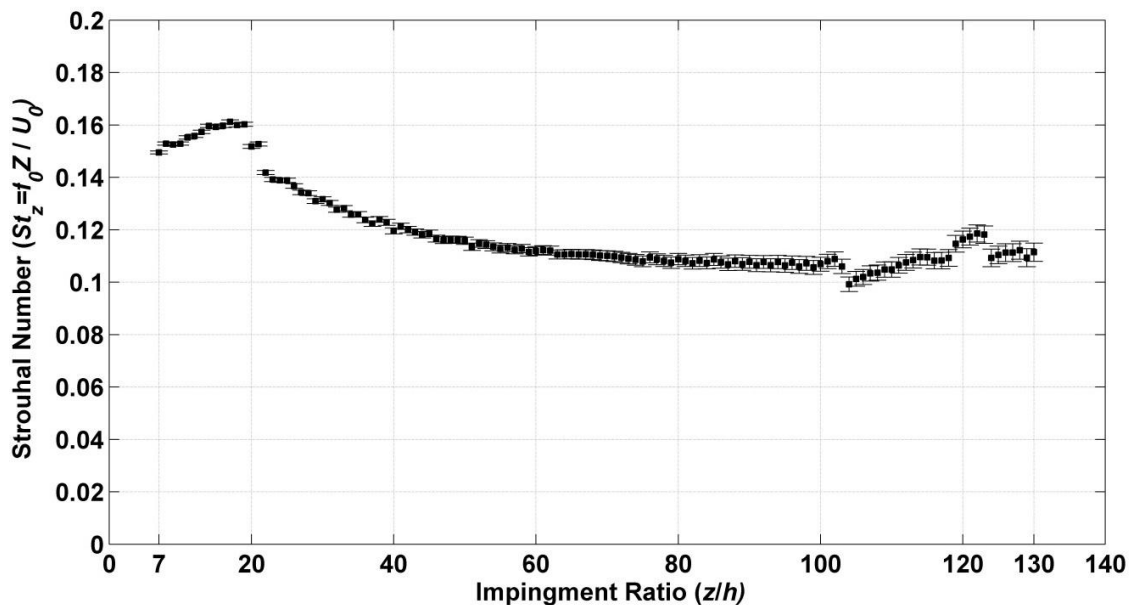


Figure II-1 Plot for Strouhal number (St_z) plot for $U_0=150$ m/s and variable impingement ratio (z/h) with uncertainty error bars

AIII-3- Uncertainty Analysis for Particle Image Velocimetry

In this section, the error and uncertainty associated with the flow field measurements using the particle image velocimetry are presented in detail. The flow field measurements were done for the case of $z/h = 50$ and $U_0 = 200$ m/s oscillating at $f_0 = 226$ Hz. Table II-2 presents an over view of the measurement parameters and the associated

uncertainties. The flow fields were processed using a Recursive Nyquist Grid engine that utilizes a multi-grid processing scheme with two refinement steps with a final interrogation window size of 8 pixels \times 8 pixels, while a first order deformation scheme was used with a Gaussian sub pixel interpolation. The resulted vector validation was more than 99 % for all acquired flow fields, while bad vectors were replaced using a standard interpolation scheme. The employed error analysis method in the current study is similar to that of Arthurs (2012) which was done for the same nozzle but for a different nozzle thickness and different impingement setup.

There are two main uncertainties that are important for the PIV error analysis. First, the fluid particle displacement uncertainty; Second, the uncertainty in velocity gradients that are used to find vorticity fields. Scarano & Riethmuller (2000) provided PIV displacement uncertainty data for known particle displacement gradients, while Raffel et al. (2007) outlined the corresponding absolute uncertainty in velocity gradients for a known particle displacement uncertainty using the following relationship:

$$\varepsilon_{\left(\frac{\partial u}{\partial y}\right)} = \frac{0.7\varepsilon_u}{\Delta Z}. \quad (\text{II-10})$$

$$\varepsilon_{\left(\frac{\partial v}{\partial Z}\right)} = \frac{0.7\varepsilon_v}{\Delta Y}. \quad (\text{II-11})$$

where ε_u is the particle displacement uncertainty in stream wise direction Z and ε_v is the particle displacement uncertainty in cross stream direction Y , $\varepsilon_{\left(\frac{\partial u}{\partial y}\right)}$ is the downstream

Measurement Parameters

Total Camera Sensor Size	2048 pixels × 2048 pixels
Total Field of View	130.87 mm × 130.87 mm
Size of field of View (Masked Area)	1698 pixels × 1576 pixels
Masked field of view	110 mm × 100 mm
Spatial Calibration	63.90 $\mu\text{m}/\text{pixel}$
Laser Pulse Separation Time	450 ns
Number of Image acquisition	800 total images, 100 image per phase

Image Processing Parameters

Initial Window Size	32 pixels × 32 pixels
Final Window Size	8 pixels × 8 pixels
Grid Engine	Recursive Nyquist Grid
Number of Grid Refinements	2 refinements
Subpixel Interpolation Scheme	Gaussian
Window Distortion Scheme	1st Order Deformation Scheme
Final Overlap	75%
Number of Vectors [x×y]	[391×360] 140,760 vector per field
Spatial Resolution ($\Delta x = \Delta y$)	277 μm
Vector Validation Rate	>99%

Error Analysis

Maximum Displacement Gradient	$(\partial u/\partial y)_{\max}$	0.100 pixel/pixel
	$(\partial v/\partial x)_{\max}$	0.011 pixel/pixel
Uncertainty in Particle Displacement	ϵ_u	0.06 pixel
	ϵ_v	0.004 pixel
Relative Uncertainty of Particle	$\epsilon u/\delta u$	0.5 %
	$\epsilon v/\delta v$	0.04 %
Uncertainty of Vorticity	$\epsilon_{(\partial u/\partial y)} = 0.7\epsilon_u/\Delta X$	0.0096 pixels/pixel
	$\epsilon_{(\partial v/\partial x)} = 0.7\epsilon_v/\Delta Y$	0.0006 pixels/pixel
Relative Uncertainty of Vorticity	$\epsilon_{(\partial u/\partial y)}/(\partial u/\partial y)_{\max}$	9.6 %
	$\epsilon_{(\partial v/\partial x)}/(\partial v/\partial x)_{\max}$	5.4 %

Table II-2 Results of PIV uncertainty analysis for $z/h = 50$ and $U_0 = 200$ m/s

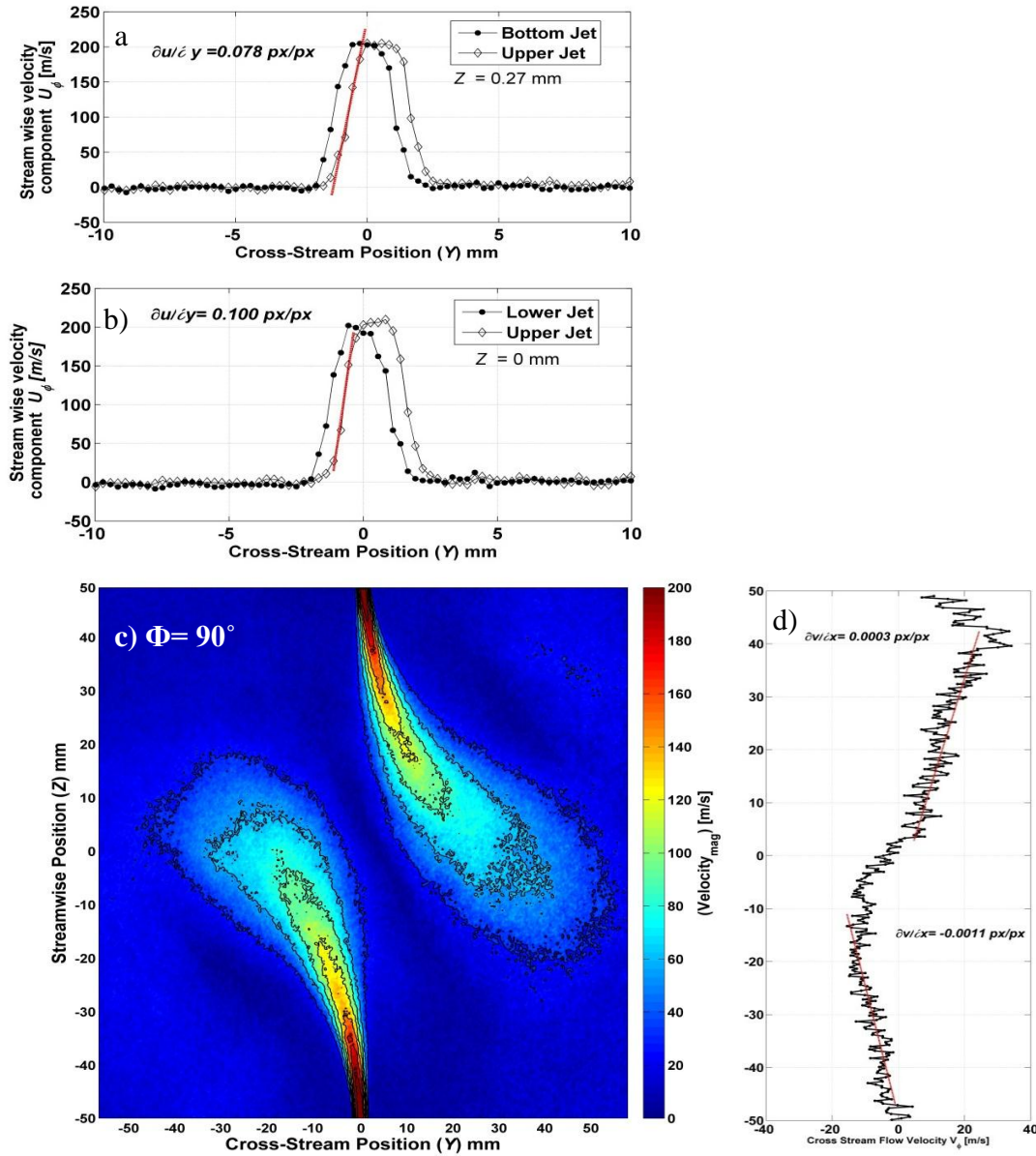


Figure II-2 Velocity Magnitude plot and velocity profiles for case of $z/h = 50$

and $U_0 = 200$ m/s oscillating at $f_0 = 226$ Hz at $\Phi = 90^\circ$

velocity gradient uncertainty and $\varepsilon_{\left(\frac{\partial v}{\partial Z}\right)}$ the cross stream velocity gradient uncertainty,

while the constant 0.7 was introduced to account for the error due to the evaluation of gradients using a central difference method to calculate the velocity gradient themselves.

While the processing engines that use the deformation based processing scheme are useful in cases of large displacement gradients that occur in high shear regions of the flow, in the current experimental case, those regions occur near the edge of the nozzle and at the middle entrainment region of the jet. One case of the acquired flow field was taken to be analyzed (where $\Phi = 90^\circ$) which has relatively high displacement gradient along the oscillation cycle.

Figure II-2 shows plot for velocity magnitude for the corresponding chosen phase angle ($\Phi = 90^\circ$), and the velocity profiles that were used to find the maximum displacement gradients for this case. The top velocity profiles in Figure (II-2) (a and b) present the U_Φ velocity component for the two jets at the edge of the nozzle at $Z=0$, and at $Z= 0.27$ mm downstream. For the current case, the maximum displacement gradient occurs at the edge of the upper jet having a maximum stream wise displacement gradient of $(\partial u/\partial y)_{\max} = 0.1$ pixel/pixel. For the cross stream displacement gradient, presented in Figure (II-2d), the maximum displacement gradient is $(\partial v/\partial x)_{\max}=0.011$ pixel/pixel. According to Scarano and Riethmuller (2000), the previous displacement gradient correspond to uncertainty in particle displacements of $\varepsilon_u = 0.06$ pixel and $\varepsilon_v = 0.004$ pixel. And by substituting in equations (II-10) and (II-11), it results in uncertainty in velocity gradients of $\varepsilon_{\left(\frac{\partial u}{\partial y}\right)} = 0.0096$ pixels/pixel and $\varepsilon_{\left(\frac{\partial v}{\partial x}\right)} = 0.0006$ pixels/pixel. This eventually leads to relative uncertainty in vorticity gradients of $\varepsilon_{(\partial u/\partial y)}/(\partial u/\partial y)_{\max}=9.6$ % and $\varepsilon_{(\partial v/\partial x)}/(\partial v/\partial x)_{\max}=5.4$ %.

Appendix III: Effect of measurement equipment on Acoustic Response

AIII-1 Microphone Location

In the current section, the effect of the microphone location on the acquired acoustic data is presented. One case of operating conditions is chosen for simplicity, where the nozzles exit flow velocity $U_0 = 200$ m/s and two planar nozzles are 60 mm apart ($z/h = 30$, $h = 2$ mm). The microphone was positioned at a plane 25.4 mm above the nozzles top surface plane, at a midpoint position between the two nozzles as shown in Figure IV-1. Ten different microphone locations were chosen along the same line at the

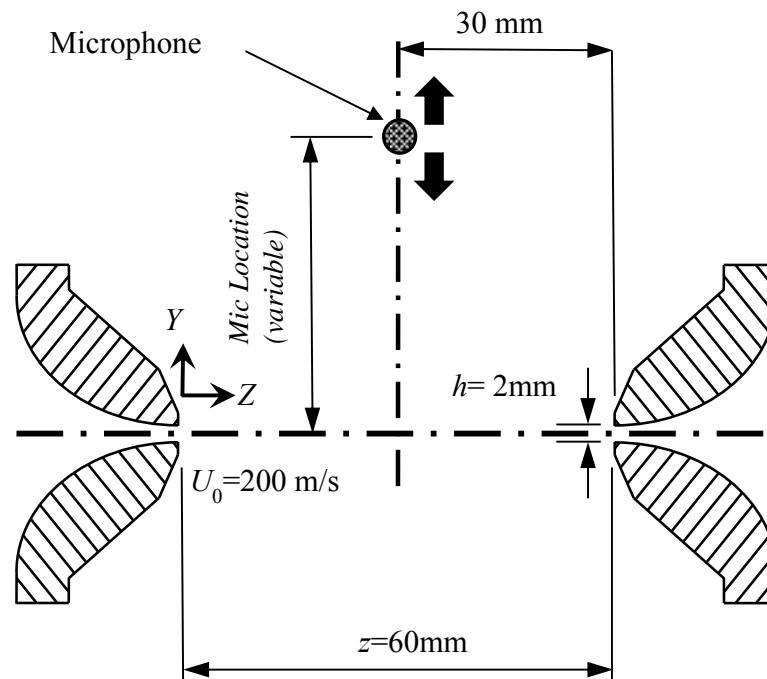


Figure III-1 Schematic Microphone location effect setup

middle between the two nozzles, starting at a point 0 inch away and up to a point 9 inch away with 1 inch step. For each location the acoustic tone was acquired for comparison with same data acquisition and spectral averaging parameters outlined in chapter 3.

Figure IV-2 is a waterfall plot for the frequency spectra showing effect of microphone location on the acoustic response, where each spectra on the waterfall plot represents a location of the microphone, starting with 0 inch where the microphone is located just above the common centerline of the two jets, then with offset of 1 inch away from the common centerline up to 9 inches. We observe that a sharp distinct peak is present at each frequency spectra along the waterfall plot; this sharp peak is the fundamental tone frequency (f_0) of the system. Variation of the microphone location had an effect on sharpness of the peak frequency, whereas increasing the distance away from the common centerline lead to a more distinct sharp peak of the fundamental tone frequency (f_0), with a relatively higher sound pressure level for the fundamental tone.

Figure IV-3 shows a color plot for the same experimental set, where such plots better outline the values of sound pressure level at different spectra. The red color in the Figure has the highest SPL and blue color has lowest SPL. It is observed that the SPL for fundamental tone frequency increases as the Mic location distance increases, while the SPL of the higher harmonic tones f_1, f_2 is initially constant, but starts to decrease at location longer than 4 inches. Accordingly, the location of 2 inches was chosen such that the fundamental tone peak is sharp enough while the higher harmonic tones are noticeable too.

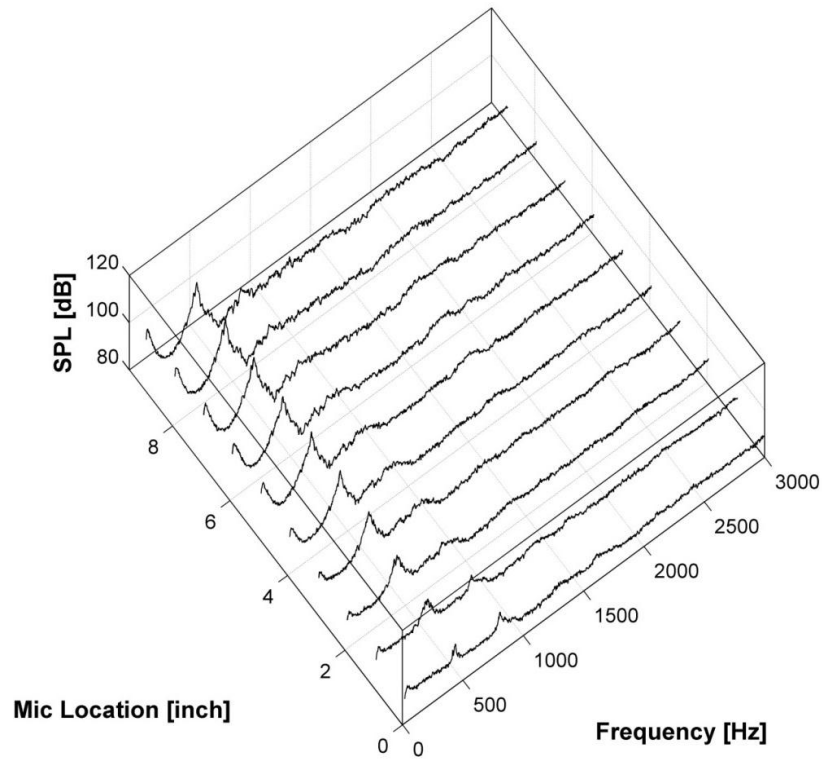


Figure III-2 Waterfall plot for variable Mic Locations at $U_0 = 200$ m/s and $z/h = 30$

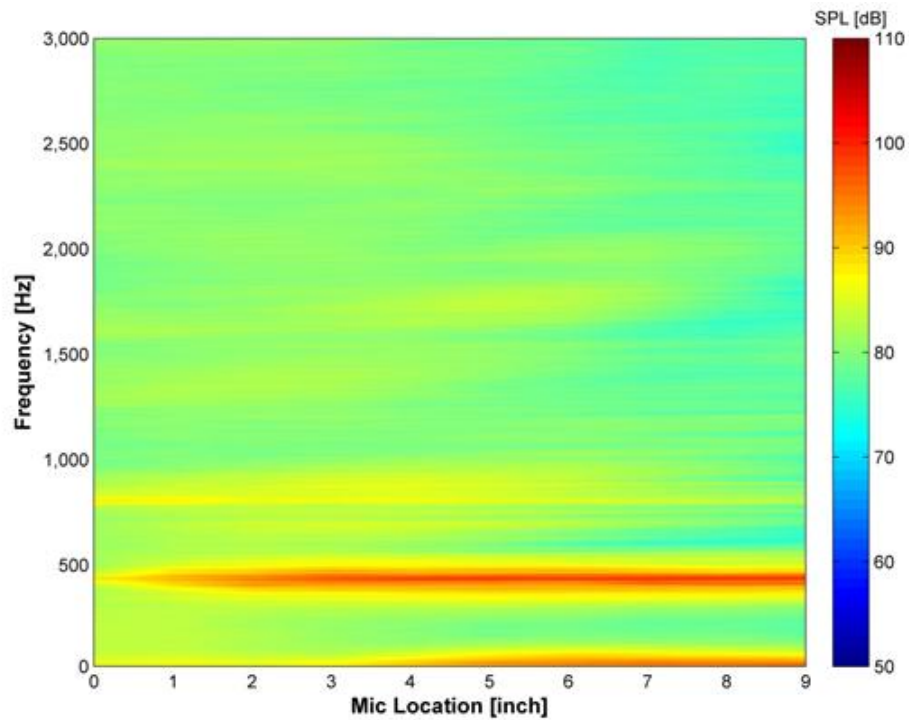


Figure III-3 Color plot for variable Mic Locations at $U_0 = 200$ m/s and $z/h = 30$

Figure IV-4 presents the variation of the fundamental tone frequency (f_0) with the microphone location, little or no effect was observed in the fundamental tone frequency as the Mic location was increased above 2 inches, a point where the fundamental tone frequency (f_0) was recorded to be 432 Hz the variations in this frequency was found at a maximum of 2 Hz as the microphone location was changed.

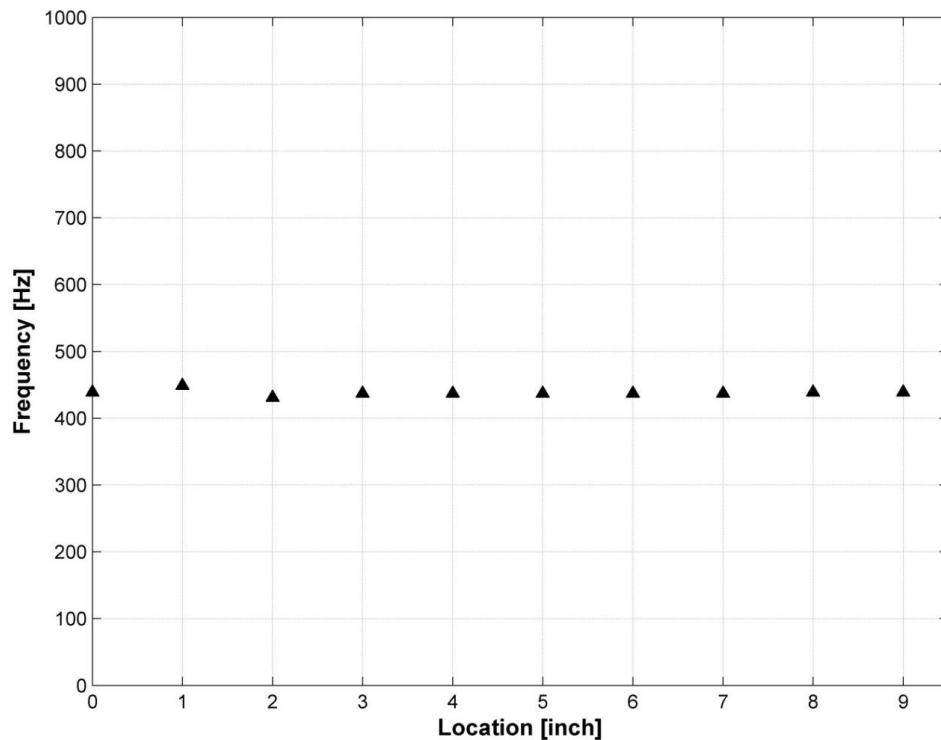


Figure III-4 Plot for fundamental tone frequency (f_0) with the microphone location [inch]

AIII-2 Effect of Spectral Averaging

In this section, the effect of averaging the acquired frequency spectra on the final spectra that was used to represent the system is investigated. Averaging usually provides

more reliability in detecting the tone frequency from the acoustic tone signal, where any random or temporal noise that is from the outside environment is reduced by the process of averaging, leaving out only the acoustic response of the system itself. However, the improper choice of number of spectral averages can lead to introduction of tones and noise that is not produced by the system. This case can happen when the number of the averaged spectra is non-sufficient, or in other cases choice of huge number of averages which is time consuming in terms of acquiring the data with no effect on the final result.

In order to investigate the effect of spectral averaging on the tone spectra, one testing condition case was chosen for simplicity, where nozzles' exit flow velocity was $U_0 = 200$ m/s and the impingement ratio was $z/h = 40$, and the jet thickness was $h = 2$ mm. Figure IV-5 shows the resulted tone spectra for different number of averaged spectra starting with IV-a showing averaged spectrum for 5 acquired spectra till IV-f which shows averaged spectrum of 1000 samples. The spectral averaging effect is obvious in Figure IV-5 where we compare a) with b) and c) we observe that averaging eliminated random noise and produced smooth spectra with distinct observed tones. The fundamental tone frequency and SPL are displayed at the top right of each sub plot, there is no change of the fundamental tone frequency f_0 beyond 100 averaged spectra, where there very minor change in SPL within the error of the measurement instrument itself (± 0.5 dB). Thus the choice of 100 averaged spectra is convenient to acquire the acoustic tone response spectra for the current study.

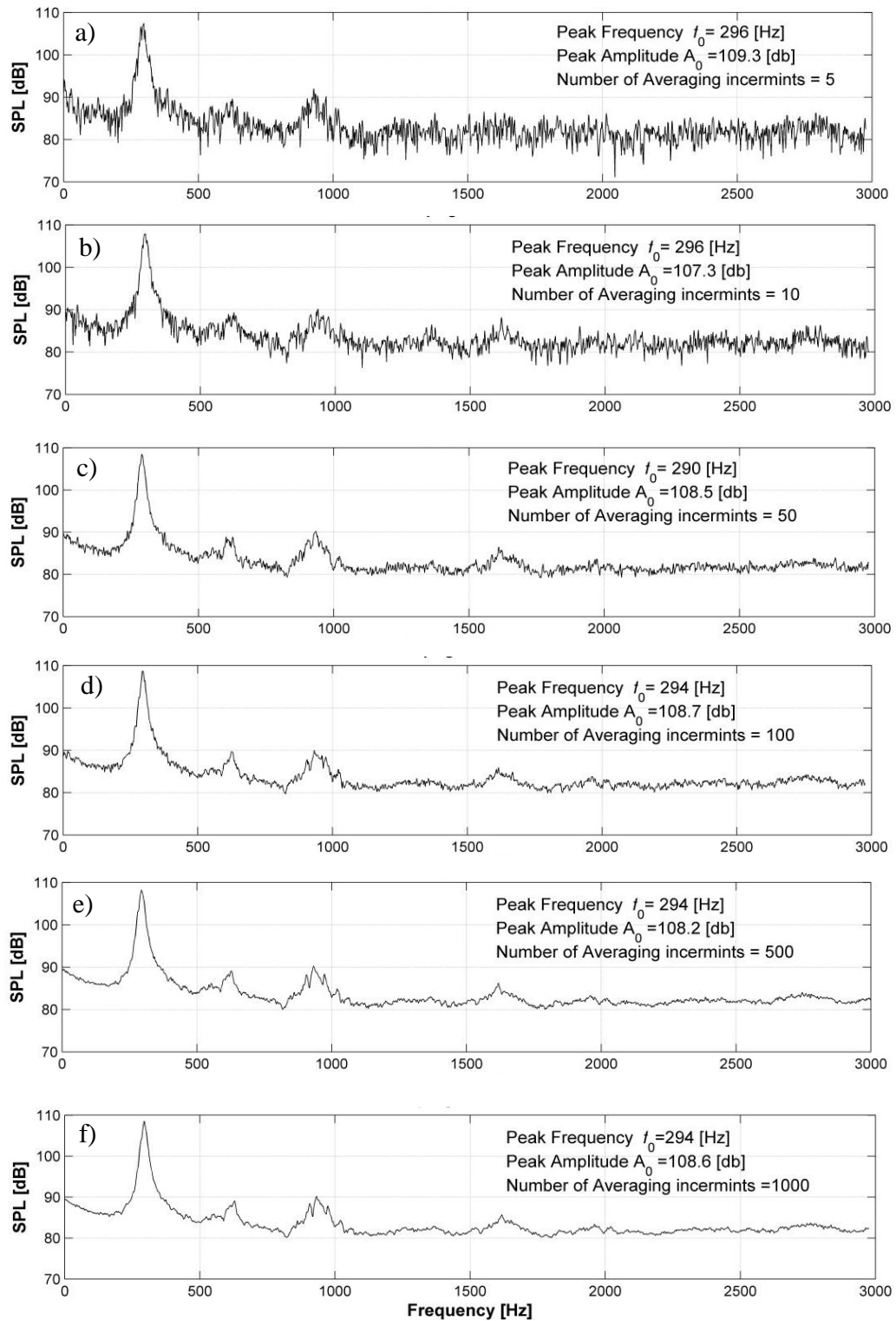


Figure III-5 Acoustic Tone Spectra for different number of averaged samples for

$$U_0 = 200 \text{ m/s}, z/h = 40, \text{ and } h = 2 \text{ mm}$$

Appendix IV: Experimental Equipment Data

Rotary Stage



Figure IV-1 481 Series High-Performance Rotation Stages
 (http://www.newport.com/481-Series-High-Performance-Rotation-Stages/144550/1033/info.aspx#tab_Specifications)

481 Series

- High-Performance Rotation Stages
- Sensitivity to 15 arc sec
- 360° coarse/5° fine motion
- Post or Table-top mounting
- Rotates 1 in. (25.4 mm) diameter polarizers and wave plates
- Adaptor available for mounting 1/2-in diameter optics

Sensitivity	AJS Screw, 15 arc sec; Micrometer, 30 arc sec
Graduations	1 °
Vernier Graduations (arc min)	5
Backlash	Negligible
Travel, Fine	5 °
Load Capacity [lb (N)]	40 (178)
Maximum Drive Torque [in-lb (cm-kg)]	8 (9.6)

Table IV-1 Rotary Stage Specification

Manual Vice Velmex™ 2.5 inch wide A25 series screw drive UniSlide Vice



Figure IV-2 Velmex™ 2.5 inch wide A25 series screw drive UniSlide Vice A2506P40-S2.5

(http://www.velmex.com/manual_cross_sections.asp?series=2500)

Catalog Number: A2506P40-S2.5

Type: Graduated Knob

Travel: 3.5"

Product Features: Accurate lead screw, engraved knob and lithographed scale

Product Benefits: Measure position to 0.001" or 0.01 mm

Number of turns/inch: 40

Number of turns/cm: N/A

Series: A25

Base Length: 6"

Width: 2.5"

Electronic Vice and power supply



Figure IV-3 VX1 Stepping Motor Controller
(http://www.velmex.com/pdf/controllers/vxm_user_manl.pdf)

Unit Conversion for Velmex Positioners

Lead Screw Models			Speed		
	UniSlide*	BiSlide**	Advance per turn Units	Advance per step Units	@ 1000 SPS (2.5 rev/sec) Units
C	P40	E25	0.025 inch	0.0000625 inch	0.0625 inch/sec
B	P20	E50	0.05 inch	0.0001250 inch	0.125 inch/sec
W1	P10	E01	0.1 inch	0.0002500 inch	0.25 inch/sec
W2	P5	E02	0.2 inch	0.0005000 inch	0.5 inch/sec
W4	P2.5	E04	0.4 inch	0.0010000 inch	1 inch/sec
K1	Q1	M01	1 mm	0.0025 mm	2.5 mm/sec
K2	Q2	M02	2 mm	0.0050 mm	5 mm/sec

* Typical UniSlide model (where x is from above table): MB4024xJ-S4

** Typical BiSlide model (where x is from above table): MN10-0100-x-21

To convert from "real" units to steps, divide the distance desired to move by the Advance per step. (Distance ÷ Adv per step = Steps)

Example #1: To move 3.000 inches with the BiSlide E04 lead screw ($3.000 \div 0.001 = 3,000$) requires a 3,000 step index.

Example #2: To move 90 degrees with the B5990 rotary table ($90 \div 0.01 = 9,000$) requires a 9,000 step index.

Example #3: To move 4.000 inches with the UniSlide W1 lead screw ($4.000 \div 0.00025 = 16,000$) requires a 16,000 step index.

Other formulas:

1 Motor rev = 400 steps

Linear Speed = Advance per step x steps per second

Rotary Speed = Advance per step x steps per second

Steps per second ÷ 400 = rev/sec

Table IV-2 Electronic Vice Specifications
(http://www.velmex.com/pdf/controllers/vxm_user_manl.pdf)

GRAS™ model 40BP ¼" high-level microphone

Figure IV-4 40BP ¼" high-level microphone
 (<http://www.gras.dk/g-r-a-s-40bp-pressure-microphone.html>)

Open-circuit sensitivity @ 250 Hz (±2 dB)	[mV/Pa]	1.6
Open-circuit sensitivity @ 250 Hz (±2 dB)	[dB re 1V/Pa]	-56
Frequency response (±1 dB)	[Hz]	10 to 25 k
Frequency response (±2 dB)	[Hz]	4 to 70 k
Resonance frequency	[kHz]	50
Dynamic range lower limit (microphone thermal noise)	[dB(A)]	34
Dynamic range upper limit	[dB]	170
Dynamic lower limit with G.R.A.S. preamplifier	[dB(A)]	39
Dynamic range upper limit with G.R.A.S. preamplifier @ ±14 V / +28 V power supply	[dB]	169
Dynamic range upper limit with G.R.A.S. preamplifier @ ±60 V / +120 V power supply	[dB]	181
Microphone cartridge capacity, typical	[pF]	7
Microphone cartridge venting		Rear
IEC 61094 designation		WS3P
Temperature range, operation	[°C / °F]	-40 to 150 / -40 to 302
Temperature range, storage	[°C / °F]	-40 to 85 / -40 to 185
Temperature coefficient @250 Hz	[dB/°C / dB/°F]	-0.01 / -0.006
Static pressure coefficient @250 Hz	[dB/kPa]	-0.008
Humidity range non condensing	[% RH]	0 to 100
Humidity coefficient @250 Hz	[dB/% RH]	-0.0013
Influence of axial vibration @1 m/s ²	[dB re 20 µPa]	55
CE/RoHS compliant, WEEE registered		Yes / Yes, Yes
Weight	[g / oz]	1.5 / 0.053

Table IV-3 GRAS™ model 40BP ¼" Microphone Specification

(<http://www.gras.dk/g-r-a-s-40bp-pressure-microphone.html>)

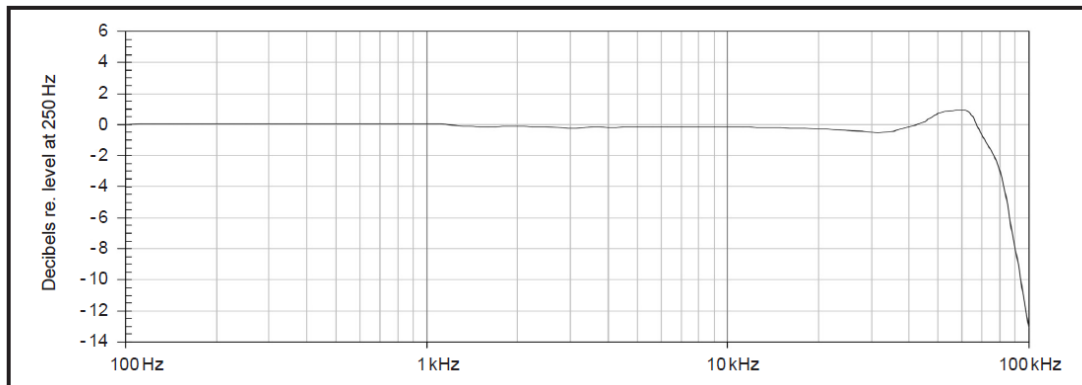


Figure IV-5 Typical frequency response for Type 40BP (without protection grid)
(<http://pdf.directindustry.com/pdf/gras-sound-vibration/-inch-pressure-microphone-type-40bp/70183-180877.html>)

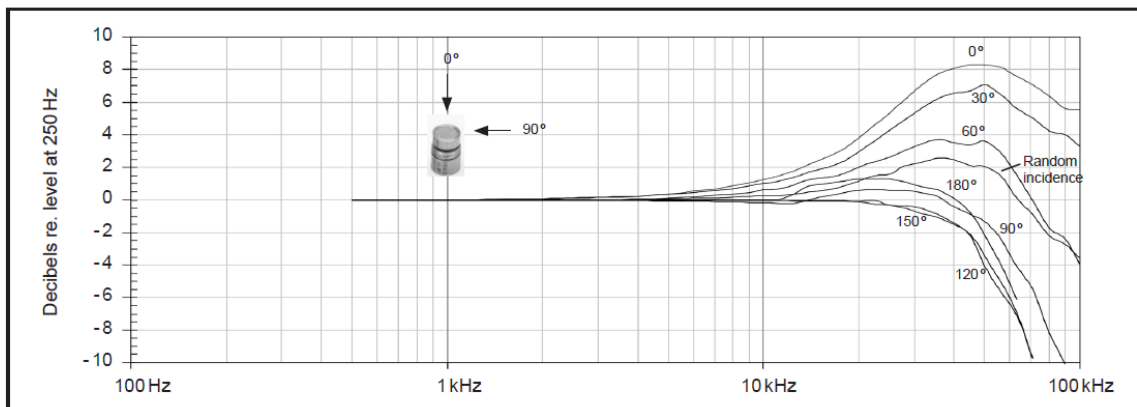


Figure IV-6 Free-field corrections for various angles of incidence (without protection grid)
(<http://pdf.directindustry.com/pdf/gras-sound-vibration/-inch-pressure-microphone-type-40bp/70183-180877.html>)

GRAS™ model 26AC preamplifier

Figure IV-7 ¼" Preamplifier Type 26AC
 (<http://magentobee.dk/gras/26ac-standard-preamp-cable.html>)

Specifications

Frequency response (18pF/small signal):	
2.5Hz - 200 kHz	±0.2 dB
Slew rate:	
	20 V/μs
Input impedance:	
	20 GΩ, 0.5 pF
Output impedance (Cs = 20 pF, f = 1000Hz):	
Typical	75 Ω
Noise (measured with 20 pF ½" dummy mic.):	
A-weighted:	≤2.5 μV rms (typically 1.8 μV rms)
Linear (20 Hz - 20 kHz):	≤6 μV rms (typically 3.5 μV rms)
Gain*:	
Typical:	-0.27 dB
Power supply:	
Single:	28 V (0.7 mA) to 120 V (2.5 mA)
Dual:	±14 V (0.7 mA) to ±60 V (2.5 mA)
Maximum signal-output voltage (peak):	
	from ±10 V to ±50 V
Temperature:	
Operation:	-30°C to +70°C
Storage:	-40°C to +85°C
Relative humidity:	
Operation:	0 to 95 %
Storage:	0 to 95 %
Dimensions and Weight:	
Diameter:	6.35 mm (¼")
Length:	43 mm (1.7")
Weight (without cable):	6 g (0.2 oz)
Weight (with cable + LEMO conn.):	50 g (1.8 oz)

* Measured with 20 pF ½" dummy microphone

Figure IV-8 Specifications for G.R.A.S. ¼" Preamplifier Type 26AC
 (<http://magentobee.dk/gras/26ac-standard-preamp-cable.html>)

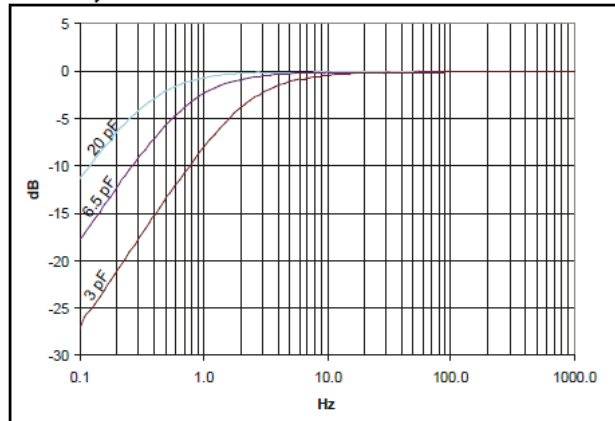


Figure IV-9 Typical low-frequency response of Type 26AC for 1/2" (20 pF), 1/4" (6.5 pF) and 1/8" (3 pF) microphones
 (<http://magentobee.dk/gras/26ac-standard-preamp-cable.html>)

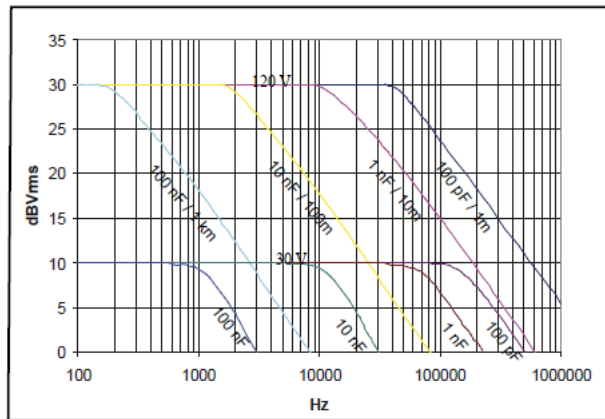


Figure IV-10 Typical max. rms output signal with 120 V and 30 V supply
 (<http://magentobee.dk/gras/26ac-standard-preamp-cable.html>)

GRAS™ model 12AA 2-channel power supply module



Figure IV-11 GRAS™ model 12AA 2-channel power supply module
 (<http://magentobee.dk/gras/12aa-2-ch-power-module-gain-filters-and-syscheck.html>)
Specifications

- 2 channels (A and B), each comprising:
- Input socket: 7-pin LEMO 1B female
- Output socket: BNC coaxial
- Gain: -20 dB to $+40$ dB in 20 dB steps, and Direct mode
- Output-voltages:
 Preamplifier supply: 28 V or 120 V
 Polarization voltage: 0 V or 200 V
- Gain error: <0.2 dB
- Frequency response (Lin setting): 3.5 Hz - 200 kHz: ± 1.0 dB
 2 Hz - 250 kHz: ± 3.0 dB
- Channel separation: 20 Hz - 20 kHz: > 65 dB
- Inherent noise: (20 Hz - 20 kHz with input grounded)
 A-weighted: < 1 μ V
 Lin: < 1.6 μ V (20 Hz - 20 kHz with G.R.A.S. preamplifier and 20 pF dummy microphone)
 A-weighted: $< 3,2$ μ V
 Lin: < 5.7 μ V (values valid for $+20$ dB and $+40$ dB gain re. input)
- A-weighting filters: Compliant with IEC 60651 Type 0
- High-pass filter:
- 3-pole Butterworth, -1 dB at 20 Hz

- Output impedance: 30 Ω
- Power supply: 10 x LR6 (AA) standard alkaline cells, or
- DC mains/line adapter supply: 12 V - 18 V
- Power consumption: With one G.R.A.S preamplifier using:- 120 V: 190 mA 28 V: 160 mA
- Fuse: 315 mA (low impedance <1.5 Ω), 250 V
- Dimensions: (1/12 of a standard 19-inch rack)
Height: 132.6 mm (5 ¼ in)
Width: 34.6 mm (1.3 in)
Depth: 196.0 mm (7.7 in)
Weight: 770 g (1.69 lbs)

Source:

(http://magentobee.dk/gras/media/docs/files/items/m/a/man_12aa_ver_01_09_05.pdf)

G.R.A.S. Sound Calibrator Type 42AB



Figure IV-12 Sound Calibrator Type 42AB

(http://www.sonustc.com/la_zh/upload/DownFiles/PB/ST/GRAS_Calibrators.pdf)

Specifications

<p>Output signal: Specified on the calibrator for reference conditions.</p> <p>Reference conditions: Ambient temperature: 20 °C Ambient pressure: 101.3 kPa Humidity: 65% RH Effective load volume: 250 mm³</p> <p>Accuracy: SPL: 114 dB ± 0.2 dB re. 20 µPa Frequency: 1000 Hz ± 0.2% Complies with IEC 942-1988 Class 1.</p> <p>General: Typical sensitivity to change in load volume: 0.0003 dB/mm³ at 1000 Hz Time for level to stabilize: max. 2 sec.</p> <p>Microphone sizes: According to IEC 1094-4 With adapters removed: 1-inch With adapter(s): ½-inch and ¼-inch</p> <p>Harmonic distortion: Maximum: 1%</p> <p>Controls: Push-button start. Automatic switch-off.</p> <p>CE classification: EMC: EN 50081-1, EN 50082-1 Safety: EN 61010-1, 1993 For portable equipment, pollution category 2.</p>	<p>Ambient requirements for specified operation: Temperature: -10 °C to +50 °C Ambient pressure: 65 kPa to 108 kPa Humidity: 10% to 90% RH</p> <p>Battery: Type: 6LR61, 9 V Life: ≈ 30 hours Battery type 6F22G has a shorter life, whereas a 9 V lithium battery gives an extended operating time.</p> <p>External supply voltage: 7.5 V to 15 V Automatic shut-off when voltage drops below 7.5 V</p> <p>Overall weight and dimensions: Weight: 185 gm with battery Length: 109.5 mm Diameter: 40 mm</p> <p>Accessories included: Delivered fitted with a removable adapter for calibrating ½-inch microphones. Remove this for calibrating 1-inch microphones. Adapter for ¼-inch microphones: RA0049 9 V alkaline battery: EL0003</p> <p>Accessories available: Adapter for ½-inch microphones: RA0069</p>
---	--

Figure IV-13 Specifications for Sound Calibrator Type 42AB
(http://www.sonustc.com/la_zh/upload/DownFiles/PB/ST/GRAS_Calibrators.pdf)

National Instruments NI-9234 data acquisition card (24-bit)



Figure IV-14 National Instruments NI-9234 data acquisition
(<http://sine.ni.com/nips/cds/view/p/lang/en/nid/208802>)

Specifications

Number of channels	4 analog input channels
ADC resolution	24 bits
Type of ADC	Delta-Sigma (with analog prefiltering)
Sampling mode	Simultaneous
Type of TEDS supported	IEEE 1451.4 TEDS Class I
Internal master timebase (f_M)	
Frequency	13.1072 MHz
Accuracy	± 50 ppm max
Data rate range (f_s) using internal master timebase	
Minimum	1.652 kS/s
Maximum	51.2 kS/s
Input coupling	AC/DC (software-selectable)
AC cutoff frequency	
-3 dB	0.5 Hz
-0.1 dB	4.6 Hz max

Table IV-4 NI-9234 data acquisition specifications
<http://sine.ni.com/ds/app/doc/p/id/ds-316/lang/en>

Validyne DP-15 pressure transducer



Figure IV-15 Validyne DP-15 pressure transducer
(<http://validyne.com/ProductDisplay.aspx?Pid=12>)

Specifications

Standard Ranges: ± 0.08 psid FS to 3200 psi FS (see range selection chart, left)

Accuracy: $\pm 0.25\%$ FS (including effects of non-linearity, hysteresis and non-repeatability)

Overpressure: 200% FS up to 4000 psi maximum, with less than 0.5% zero shift*

Line Pressure: 3200 psig operating

Line Pressure Effect: Less than 1% FS zero shift/1000 psig

Output: ± 35 mV/V full-scale nominal

Inductance: 20 mh nominal, each coil

Zero Balance: Within 5 mV/V

Excitation: Rated: 5 Vrms, 3 kHz to 5 kHz

Limits: 30 Vrms at 3 kHz 1 kHz to 20 kHz with 20 mH coils

Pressure Media: Corrosive liquids and gases both sides, compatible with 410ss and inconel**

Temperature: Operating: -65 °F to 250 °F** Specified: 0 °F to 160 °F

Thermal Zero Shift: 1% FS/100 °F typical

Thermal Sensitivity Shift: 2%/100 °F typical

“O” Rings: Buna N**

Pressure Cavity Volume: 1.2×10^{-2} cu. in.

Volumetric Displacement: 6×10^{-4} cu. in.

Pressure connection: $1/8$ ” – 27 NPTF**

Electrical Connection: PTO2A-10-6P, Amphenol (formerly Bendix) or equivalent. Mating connector PTO6A-10-6S (SR) not furnished.**

Weight: 12 ounces (.34 Kg)

Replacement Diaphragm: See Pressure Range Chart

Source: (<http://validyne.com/ProductDisplay.aspx?Pid=12>)

Two dimensional Particle Image velocimetry system built by TSI

Nd:YAG laser Laser Specifications

Specifications

Dual YAG Laser arrangement

Wavelength	532 nm
Transverse mode	multimode
Beam Diameter	3.0 mm
Beam Divergence	4.0 mr
Polarization	Linear, horizontal
Q-switch Performance at 1 kHz	
Average Power	14 W
Pulse Energy	14 mJ
Pulse Width	160 ns
Peak Pulse Power	87 kW
Average Power	
5 kHz	32 Watts
10 kHz	40 Watts
20 kHz	35 Watts
Mechanical	
Optical Assembly	131L x 30W x 21H cm
Power Station Dimension	91H x 62W x 98D cm
Direct Cooling Water	20 l/min at 20°C max temp (35 psi pressure) (Chiller is NOT included but optional)
Electrical Power	220 +/- 10% VAC, 3 -phase, 50/60 Hz, 30A (or 380 +/- 10% VAC, 3 phase, 50/60 Hz, 20A)

Specifications subject to change without notice.

Figure IV-16 532nm New Wave Solo 120XT pulsed Nd:YAG laser specifications (http://www.tsi.com/uploadedFiles/_Site_Root/Products/Literature/Spec_Sheets/Lee_Laser_2980482.pdf)

PowerView Plus 4MP Camera Specifications

Specifications

Model 630059 POWERVIEW Plus 4MP Camera

Imaging Device	Progressive Scan Interline CCD with microlens
Pixel Resolution	2048 × 2048 pixels
Pixel Size	7.4 μm (H) × 7.4 μm (V)
Image Size	15.15 mm (H) × 15.15 mm (V)
Intensity Dynamic Range	12-bit
Frame Rate	16 fps in Frame Straddling Mode
Quantum Efficiency	57% maximum
CCD Operating Temperature	40°C
Spectral Range	350 nm to 740 nm (more than 20% QE)
Blooming Suppression	>300X
Pixel Clock Rate	40 MHz per channel
Number of Channel Outputs	2 channels
Frame Straddling Time	200 ns
Protection Mask	Integrated protection mask for the CCD output circuit
Lens Mount	F-mount
Camera Output	Dual output parallel LVDS
Operation Modes	Free Run, Triggered and Frame Straddling
Exposure Time	42 μs to 105 ms for Frame A in Frame Straddling; 42 μs to 105 ms for single frame in Triggered
Binning	1 to 12, horizontal and vertical
Camera Control	RS-232 via frame grabber cable
Camera Display	LED display of operation, power and output
Camera Head Dimension	45 × 68 × 66 mm
Camera Head Weight	0.8 kg
Camera Interface	64-bit Camera Link
Frame Grabber Cable	5 m standard with RS-232 communication
Power Cable	5 m standard with universal power supply
Power	12 VDC @ 6.0 W
Standard Camera Lens	Nikon 50 mm F1.8 lens

Figure IV-17 PowerView Plus 4MP camera Specifications
 (http://www.tsi.com/uploadedFiles/_Site_Root/Products/Literature/Spec_Sheets/2980283A-PowerPLus4MP.pdf)

Laser pulse synchronizer Specifications

Specifications

Model 610035 Synchronizer

Pulse Generation

Delay	0 - 1000 sec.
Pulsewidth	10 ns to 1000 sec.
Resolution	1 ns
Time base	100 MHz, 25 PPM crystal oscillator
RMS jitter	<400 ps

Outputs

Outputs	TTL/CMOS, Adjustable 2 - 20 V, 35 V (optional)
Impedance	50 Ohms
Slew Rate	>0.5 V/ns
Overshoot	<100mV + 10% of pulse amplitude
Amplitude(adjustable mode)	1 - 6 V into 50 Ohm load 2 - 12 V into high impedance load

External Trigger

Rate	DC to 5 MHz
Threshold	500 mV to 15 V
Input range	0 - 30 V
Trigger slope	rising or falling edge
RMS jitter	<5 ns
Insertion Delay	<150 ns

Communication to computer

Communication to computer	RS-232
Operating voltage	120/240 VAC, 50-60 Hz
Dimensions (H × W × D)	8 × 4.75 × 10.5 in. (20.3 × 12 × 26.7 cm)
Weight	2.5 lb. (1.1 kg)

Figure IV-18 Laser Pulse synchronizer Specifications
 (http://www.tsi.com/uploadedFiles/_Site_Root/Products/Literature/Spec_Sheets/Model%20610036_US_5001385_WEB.pdf)